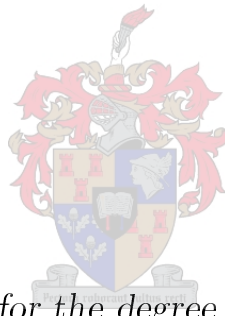


# Multi-Layered Substrate Integrated Waveguide (MSIW) Waffle-Iron Filters

by

Susan Maas



*Dissertation presented for the degree of Doctor of Philosophy  
in Electronic Engineering in the Faculty of Engineering at  
Stellenbosch University*

Supervisor: Prof. P. Meyer

December 2019

# Declaration

By submitting this dissertation electronically, I declare that the entirety of the work contained therein is my own, original work, that I am the sole author thereof (save to the extent explicitly otherwise stated), that reproduction and publication thereof by Stellenbosch University will not infringe any third party rights and that I have not previously in its entirety or in part submitted it for obtaining any qualification.

Date: .....

Copyright © 2019 Stellenbosch University  
All rights reserved.

# Abstract

## Multi-Layered Substrate Integrated Waveguide (MSIW) Waffle-Iron Filters

This dissertation will present the following two topics: (1) Implementation of a waffle-iron filter, utilising multi-layered substrate integrated waveguide (MSIW) technology and (2) Developing a new methodology for measuring scattering parameters of multimode waveguide filters.

The classical image impedance synthesis method for waffle-iron filter design is used to develop two filters. Filter A is a classical MSIW Waffle-iron filter and filter B is an extended version with an extra step in the middle of the filter.

This work proposes two methods in measuring a multimode waveguide filter; one utilising a set of measurements with different probe positions, and one using a radiating horn.

The prototypes presented, displays less than -12 dB passband reflection over 8.5 to 10.5 GHz, with stopband attenuation in excess of 70 dB over the harmonic bands 15 to 43 GHz for filter A and 15 to 48 GHz for filter B. The prototypes were designed to handle 10 Watt average power in the transmitted band. A good correlation is found between synthesised and measured responses in these two designs.

# Uittreksel

## Multi-Laag Substraat Geïntegreerde Golfgeleier (MSGG) Wafel-Yster Filters

*(Multi-Layered Substrate Integrated Waveguide (MSIW) Waffle-Iron Filters)*

In hierdie verhandeling word die volgende twee onderwerpe aangebied: (1) Implementering van 'n wafel-yster filter, met behulp van multilaag-substraat geïntegreerde golfleier (MSGG) tegnologie en (2) Ontwikkeling van 'n nuwe metodologie vir die meting van S-parameters in multimode-golfleier filters.

Die klassieke beeld impedansie sintese metode vir die ontwerp van wafel-yster filter word gebruik om twee filters te ontwerp. Filter A is 'n klassieke MSGG wafel-yster filter en filter B is 'n uitgebreide weergawe met 'n ekstra stap in die middel van die filter.

In hierdie werk word twee metodes voorgestel om 'n multimode-golfleier filter te meet, een met behulp van 'n stel metings met verskillende meet posisies en een met behulp van 'n stralende horing.

Die prototipes wat aangebied word, vertoon minder as -12 dB deurlaat-band weerkaatsing oor 8.5 to 10.5 GHz, met stopband verswakking van meer as 70 dB oor die harmoniese bande 15 to 43 GHz vir filter A en 15 to 48 GHz vir filter B. Die prototipes is ontwerp om 10 Watt gemiddelde drywing in die transmissie band te hanteer. 'n Goeie korrelasie word gevind tussen gesintetiseerde en gemete waardes in hierdie twee ontwerpe.

# Acknowledgements

To say "thank you" cannot sufficiently express the thankfulness I experience in my heart. There are so many people that contributed to this thesis. First and foremost, I would like to thank my heavenly Father for the privilege to have been able to continue further in my academic career. He has given me talents, strength, and perseverance. My heart is filled with thankfulness.

I would also like to express my sincere gratitude to the following people and organisations.

Prof. Petrie Meyer for his dedicated support and encouragement as my promoter. His knowledge and guidance in technical matters is matched by his interest in his students' welfare and personal development.

Wessel Croukamp, Prof. Riana Geschke (from University of Cape Town) and Johan Fourie (from Tamashi Technology Instruments), for their support during the testing phase and lending me the necessary test equipment. I want to especially thank Anneke Bester for all her help during the measurement phase, tips on Texmaker and just for her awesome support.

Reutech Radar Systems for allowing me to use their test equipment for the power test and Anneke Stofberg for her assistance during the test.

Paul Keanly from Xsight for conducting the CT and X-ray scans.

The project relied heavily on the knowledge, insights and professional work provided by Anton Tait and Edmund Geldenhuys from TraX, and the sales team from MercuryWave during the manufacturing phase.

I also want to thank Cape Peninsula University of Technology (CPUT) for the financial contribution to my research, especially thanks to Clive Whaits, Rory Pentz, Ben Groenewald and Robert van Zyl (F'SATI), for their support during this time.

On a more personal note, I would like to thank my family and friends for

*ACKNOWLEDGEMENTS***v**

their prayers, support and encouragements. Especially to my husband Gualbert Maas and my children, Altus and Hugo, for their love and understanding. Gualbert helped me with the PCB layout phase and his PCB knowledge always astonishes me.

# Dedications

*This dissertation is dedicated to my husband Gualbert Maas.*

# Contents

<b>Declaration</b>	<b>i</b>
<b>Abstract</b>	<b>ii</b>
<b>Uittreksel</b>	<b>iii</b>
<b>Acknowledgements</b>	<b>iv</b>
<b>Dedications</b>	<b>vi</b>
<b>Contents</b>	<b>vii</b>
<b>List of Figures</b>	<b>ix</b>
<b>List of Tables</b>	<b>xii</b>
<b>Nomenclature</b>	<b>xiii</b>
<b>1 Introduction</b>	<b>1</b>
1.1 Background . . . . .	2
1.1.1 Filters with wide stopbands . . . . .	2
1.1.2 Substrate integrated waveguide (SIW) . . . . .	4
1.1.3 Methods for measuring the scattering parameters of mul- timode waveguides filters . . . . .	6
1.2 Problem Statement . . . . .	7
1.2.1 MSIW Implementation . . . . .	7
1.2.2 Measuring technique . . . . .	7
1.3 Original Contributions . . . . .	9
1.4 Dissertation Outline . . . . .	10
<b>2 SIW Technology and Manufacturing</b>	<b>11</b>
2.1 Substrate Integrated Waveguide . . . . .	11
2.2 PCB Manufacturing for MSIW . . . . .	14
<b>3 SIW Waffle-Iron Filters</b>	<b>23</b>
3.1 Introduction . . . . .	23



3.2	Design approaches for Waffle-Iron filters . . . . .	26
3.2.1	Cohn's method . . . . .	26
3.2.2	Marcuvitz's method . . . . .	29
3.3	MSIW Implementation of Waffle-Iron Filters . . . . .	30
3.3.1	Basic structure . . . . .	30
3.3.2	PCB Stack-up Design . . . . .	33
3.3.3	Design example . . . . .	34
3.4	Design of transitions . . . . .	42
3.4.1	Coax to SIW transition . . . . .	42
3.4.2	SMPM to SIW transition . . . . .	47
3.4.3	Waveguide to SIW transition . . . . .	47
3.5	Manufacturing Issues . . . . .	50
<b>4</b>	<b>Measurements</b>	<b>54</b>
4.1	Measurement of devices supporting multiple propagating modes	54
4.1.1	First measuring method: 2.4 mm connector set-up . . . . .	57
4.1.2	Second measuring method: antenna set-up . . . . .	62
4.2	Implementation of measurement system . . . . .	63
4.2.1	2.4 mm Connector set-up . . . . .	63
4.2.2	Antenna set-up . . . . .	65
4.2.3	The Thru-standard . . . . .	66
4.3	Measurements of prototypes . . . . .	66
4.3.1	Measurement 1 - Passband response . . . . .	68
4.3.2	Measurement 2 - Multimode measurements in the stop-band . . . . .	72
4.3.3	Measurement 3 - Power handling . . . . .	80
4.3.4	Summary and concluding remarks . . . . .	82
<b>5</b>	<b>Conclusion</b>	<b>84</b>
	<b>Appendices</b>	<b>85</b>
<b>A</b>	<b>MercuryWave 9350</b>	<b>86</b>
	<b>Bibliography</b>	<b>91</b>

# List of Figures

1.1	Classical waffle-iron filter. . . . .	3
1.2	Substrate integrated waveguide (SIW) structure. . . . .	5
1.3	MSIW Waffle-iron filter design stages. . . . .	8
1.4	Measurement concept. . . . .	8
1.5	Multi-layer PCB with blind vias. . . . .	9
2.1	The SIW structure and dimensions. . . . .	12
2.2	Region of interest for the SIW in the plane of $d/\lambda_c, p\lambda_c$ . . . . .	13
2.3	Cross-sectional view of microstrip, exaggerated copper roughness image. . . . .	17
2.4	Depth-controlled drilling results. . . . .	18
2.5	Un-plated section in a blind via. . . . .	19
2.6	Edge plating. . . . .	20
2.7	PCB manufacturer panel. . . . .	22
3.1	Cut-away perspective view of the Classical waffle-iron filter. . . . .	23
3.2	Definition of frequencies $f_0, f_c, f_1, f_\infty$ and $f_2$ for waffle-iron filters. . . . .	24
3.3	$\vec{E}$ -field patterns with unrounded and rounded corners. . . . .	24
3.4	Waffle-iron filter with thin rods to suppress $TE_{0n}$ modes. . . . .	25
3.5	$\vec{E}$ fields for aligned (left) and misaligned (right) extrusions. . . . .	25
3.6	Cohn's corrugated waveguide filter model, single section. . . . .	27
3.7	Design graph giving the parameter $b_0$ . . . . .	28
3.8	Design graph giving the parameter $G$ . . . . .	28
3.9	Filter A. . . . .	30
3.10	Filter B. . . . .	32
3.11	Half-inductive and half-capacitive input sections. . . . .	32
3.12	PCB stack-up. . . . .	34
3.13	PCB panel. . . . .	34
3.14	Frequencies $f_0, f_c, f_1, f_\infty$ and $f_2$ for waffle-iron filter A. . . . .	35
3.15	Filter parameter $b_0$ selection. . . . .	37
3.16	Filter B with blind vias in the extension section. . . . .	39
3.17	Filter B. . . . .	40
3.18	Routed slot and blind via walls. . . . .	41
3.19	Horizontal walls using three staggered rows of blind vias. . . . .	42

3.20	3D view of the multilayer PCB with a SMA edge mount connector to an UWB SIW transition. . . . .	43
3.21	Stack-up for the multilayer PCB with a SMA edge mount connector to an UWB SIW transition. . . . .	44
3.22	Top view of the structure, showing layer 3 and layer 6. . . . .	44
3.23	Embedded microstrip structure. . . . .	45
3.24	Manufactured PCB, (a) top view and (b) side view. . . . .	46
3.25	Measured and simulated S-parameters of the manufactured back-to-back SMA-to-SIW transition. . . . .	46
3.26	Comparison between simulated results for a back-to-back via-based transition (MS) and the proposed edge-plated transition (EMS). . .	47
3.27	SMPM PCB. . . . .	48
3.28	3 mm Air waveguide to 0.555 mm SIW transition. . . . .	49
3.29	PCB with air waveguide to SIW transition. . . . .	49
3.30	Air waveguide to SIW transition. . . . .	50
3.31	Batch 1 - Micro-section. . . . .	51
3.32	Batch 1 - CT-Scan. . . . .	51
3.33	Depth controlled drilling. . . . .	52
3.34	Batch 2 - Micro-section. . . . .	53
3.35	Batch 2 - CT-Scan. . . . .	53
4.1	Modes in a Waveguide (a) and its generalized S-Matrix representation (b). The vectors $a$ and $b$ contain the amplitudes of the incident and reflected modes at each port respectively. . . . .	55
4.2	The three-physical-port probe section. . . . .	56
4.3	3 mm High WR90 waveguide with a vertical and horizontal shifter. . .	58
4.4	Adjusting the 2.4 mm connector. . . . .	59
4.5	The 2.4 mm connector test set-up. . . . .	59
4.6	Simulated results for the $TE_{m0}$ modes. . . . .	60
4.7	Antenna test set-up. . . . .	62
4.8	Antenna measurement grid . . . . .	63
4.9	2.4 mm Connector to SIW transition. . . . .	63
4.10	2.4 mm Connector inserted in the waveguide. . . . .	64
4.11	2.4 mm Connector with a small shim-stock piece soldered to the center pin. . . . .	64
4.12	2.4 mm Connector to SIW back-to-back transition. . . . .	64
4.13	Horn antenna to SIW transition. . . . .	65
4.14	Completed horn antenna to 2.4 mm connector transition. . . . .	65
4.15	Dimensions of the horn antenna. . . . .	66
4.16	PCB test set-up. . . . .	67
4.17	Calibration mechanical structure. . . . .	67
4.18	Comparison between simulated and measured results: filter A (batch 2). . . . .	68

4.19	Comparison between simulated and measured results: filter B (batch 2).	69
4.20	Filter A: SMA-EMS-SIW-EMS-SMA classical MSIW Waffle-iron filter.	69
4.21	Filter B: SMA-EMS-SIW-EMS-SMA extended MSIW Waffle-iron filter.	69
4.22	SMA connectors soldered on batch 2.	70
4.23	Filter A: Compare batch 1 and 2.	70
4.24	Filter B: Compare batch 1 and 2.	71
4.25	SMA transition enclosures.	71
4.26	Results with or without SMA enclosures.	71
4.27	Comparison between SMPM and SMA transitions.	72
4.28	Filter A: WG-SIW-WG Classical Waffle iron filter.	72
4.29	Filter B: WG-SIW-WG Longer Waffle iron filter.	72
4.30	VNA test set-up.	73
4.31	Comparison between the calibration PCB and filter A.	73
4.32	Comparison between the calibration PCB and filter B.	74
4.33	Filter A, batch 1 - stopband results.	74
4.34	Filter B, batch 1 - stopband results.	75
4.35	Filter A, batch 2 - stopband results.	75
4.36	Filter B, batch 2 - stopband results.	76
4.37	Filter A - Compare batch 1 and 2.	76
4.38	Filter B - Compare batch 1 and 2.	77
4.39	External inspection of the filter batches.	77
4.40	PCB batch 2 - Edge plating.	78
4.41	Sealing and clamping of the test set-up.	78
4.42	Filter A batch 2 - Compare results between filter structure clamped and not clamped.	78
4.43	Antenna measurements for filter A from batch 1.	79
4.44	Antenna measurements for filter A from batch 2.	79
4.45	Antenna measurements for filter B from batch 1.	80
4.46	Antenna measurements for filter B from batch 2.	80
4.47	Power test set-up.	81
4.48	Calibration results for the power test set-up.	82
4.49	Power measurement results of filter B (batch 1).	82
4.50	Short Filter: Measurements before and after the power test.	83
4.51	Long Filter: Measurements before and after the power test.	83
A.1	Dielectric constant changing with frequency.	86
A.2	Dielectric constant changing with temperature.	87
A.3	<i>Mercurywave<sup>TM</sup></i> 9350 specifications.	88
A.4	<i>Mercurywave<sup>TM</sup></i> 9350 thermal properties.	89
A.5	<i>Mercurywave<sup>TM</sup></i> 9350 loss tangent changing with frequency.	90

# List of Tables

2.1	Layers for an inside-out build. . . . .	16
2.2	Layers for a sequential build. . . . .	17
3.1	Design specifications for filter A and B. . . . .	35
3.2	Estimated dimensions of filter A. . . . .	38
3.3	Final dimensions of filter A. . . . .	38
3.4	Modified Classification Scheme for Devices/Signals based on Band- width. . . . .	43
3.5	Dimensions of the transition in mm . . . . .	45
4.1	Matrix for set-up 1. . . . .	61
4.2	Matrix for set-up 2. . . . .	62

# Nomenclature

## Acronyms

AOI	Automated optical inspection
ASIG	Autocatalytic Silver Immersion Gold
BW	Bandwidth
CAL	Calibration
CAM	Computer Aided Manufacturing
CST	CST Microwave Studio (3D EM simulation software)
CT	Computed Tomography
CW	Continuous Waveform
DGS	Defected Ground Structure
EMS	Embedded Microstrip
HASL	Hot Air Solder Levelling
MSIW	Multi-layered Substrate Integrated Waveguide
MS	Microstrip
MW	Microwave
PCB	Printed Circuit Board
PA	Power Amplifier
Radar	Radio Detection And Ranging
RF	Radio Frequency
SIW	Substrate Integrated Waveguide
SIFW	Substrate Integrated Folded Waveguide
SIGW	Substrate Integrated Gap Waveguide
SMA	Sub-Miniature Version A (connector)
SMPM	Sub-Miniature Push-on Micro (connector)
SS	Suspended Stripline
TE	Transverse Electric
TEM	Transverse Electromagnetic
TM	Transverse Magnetic
UV	Ultraviolet

VNA	Vector Network Analyser
VSWR	Voltage Standing Wave Ratio
WG	Waveguide
WR90	Waveguide Rectangular (with a 0.9 inch inner width)
X-band	8-12 GHz Radar band

**Constants**

$c =$	$2.99 \times 10^8 \text{ m/s}$
$\pi =$	3.141592654

**Notations**

$\alpha$	Attenuation constant
$cm$	Centimeter
$dB$	Decibel
$dBc$	Decibel relative to carrier
$dBm$	Decibel relative to one milliwatt
$\varepsilon_r$	Dielectric constant
$GHz$	Gigahertz
$mm$	Millimeter
$\lambda$	Wavelength
$\lambda_g$	Guide wavelength

# Chapter 1

## Introduction

Microwave filters play an essential role in receivers and transmitters by defining the frequency of interest. Examples of microwave filter applications include satellite communications, radar and wireless communication systems. As technology and complexity increase, so do the challenges of microwave filter design. Stringent requirements, as is the case with the rapid development environment of mobile communication industry, wideband wireless communication systems are also being widely developed and applied, because of their high transmission rate, low power consumption, high security and anti-interference ability. Therefore, wideband bandpass filters with wide stopbands have received widespread attention recently, and various methods and techniques are continually revised. However, up until now the design of wide bandpass filters with wide stopbands, compact size, high selectivity and low cost are still a challenging task [1].

For high power handling, all-metal waveguide filters are most useful in the microwave frequency band, where they have a low insertion loss and high-quality factor (Q). One such filter is the waffle-iron filter. It is a metallic waveguide filter and is particularly suitable where both a wide passband and a wide stopband, free of spurious responses for all modes, are required [2]. Applications include suppressing the harmonic output of transmitters and the design of wideband diplexers.

In some applications, the use of metallic waveguide filters are not realisable due to their physical size and weight. Planar structures such as microstrip, stripline and coplanar waveguide (CPW) filters, compare to metallic waveguide filters, are compact in size, low in weight and have low manufacturing cost. However, disadvantages include low power handling and relative low Q compared to metallic waveguide structures.

Fortunately, substrate integrated waveguide (SIW) technology can fill the technology gap between planar technology and metallic waveguide, since it



combines the best of both technologies and offers a relatively high  $Q$  with the size- and cost-related advantages of printed planar circuits [3].

This dissertation will present the following two topics: (1) Implementation of a waffle-iron filter, utilising multi-layered substrate integrated waveguide (MSIW) technology and (2) Developing a new methodology for measuring scattering parameters of multimode waveguide filters.

## 1.1 Background

### 1.1.1 Filters with wide stopbands

Most distributed microwave bandpass filters have multiple passbands, which are replicas of the lumped element prototype. In most designs, only the lowest frequency passband is relevant, and the rest are considered unwanted spurious artefacts which cannot be avoided, although the design can have some control over the frequency position of the spurious bands. Usually, the filter is designed so that the edge of the first spurious band is well above any frequency of interest.

In planar structures, lowpass filters can also be used to create a wide stopband. In lowpass filters, all frequencies below a set frequency are selected, and all frequencies above this same set frequency are unwanted. TEM structures of microstrip and stripline lines are ideal for lowpass filters. The design of a microwave microstrip lowpass filter closely follows the idealised lumped-element circuit. In a stepped-impedance microstrip lowpass filter, a short section of a high-impedance transmission line can approximate a series inductance. Likewise, a short section of a low-impedance transmission line can approximate a shunt capacitor. The filters selectivity increase with the number of sections. The series inductances should also be realised by discrete sections with the highest possible impedance, while still considering etching tolerance. A section with electrical length shorter than  $\pi/4$  ( $\lambda_g/8$ ) provides a broader stopband [4]. The width steps cause significant discontinuities but can be reduced by employing a thinner dielectric substrate. A wider stopband can be realised by using a stepped-impedance lowpass filter realised on a combination of microstrip and suspended striplines. The high-impedance suspended striplines have inductive elements and low-impedance shunt microstrip capacitive elements. This combination of two different lines allows a very large impedance ratio and, therefore, outstanding stopband performance, in addition to small size [4]. However, at higher frequencies, the electrical length becomes much smaller, and at a certain point, the manufacturing of such a filter becomes very difficult to realise.

In waveguides, a lowpass filter is not possible because waveguides inherently form a bandpass filter. In waveguide filter design one needs to consider the mode of transmission. In waveguides, any number of modes are possible, and higher modes frequently cause problems. Designs are usually based on a single-mode and often incorporate features to suppress unwanted modes. Corrugated-waveguide filters consist of several ridges that periodically reduce the internal height of the waveguide [2]. These types of filters are used in applications which simultaneously require a wide passband, that is well-matched, and is characterised by a wide stopband. The distance between ridges is much smaller than the  $\lambda/4$  distance between elements of other filter designs. The filter operates in the dominant  $TE_{10}$  mode, and although it suppresses higher-order modes, there is little stopband attenuation for  $TE_{20}$  and  $TE_{30}$  modes [2]. A waffle-iron filter is a variation of the corrugated-waveguide design, but with longitudinal slots through the grooves, resulting in an internal structure that has the appearance of a waffle-iron. Waffle-iron filters are used in applications that require a wide passband, low insertion loss and a wide stopband. These filters are particularly useful where suppression of spurious modes are needed. The waffle-iron filter attenuates all higher  $TE_{m0}$  modes nearly equally up to a frequency pre-determined by the distance between the metal teeth. This is true if the spacing exceeds more than half the free-space wavelength of the signal.

An example of a classical waffle-iron filter structure is shown in Figure 1.1. The pegs (also called teeth, ridges or bosses) inside the waveguide are on both the top and bottom surfaces. These pegs are aligned with each other but do not touch. The number of pegs, their size, and the distance between them, are all parameters that can be used to control the filtering specifications. Waffle-iron filters are typically fabricated from a rectangular, metallic waveguide and are thus capable of maintaining operation at very high incident power levels. The disadvantages include high manufacturing cost, primarily due to the complexity in the fabrication process, including accuracy as well as the physical size.

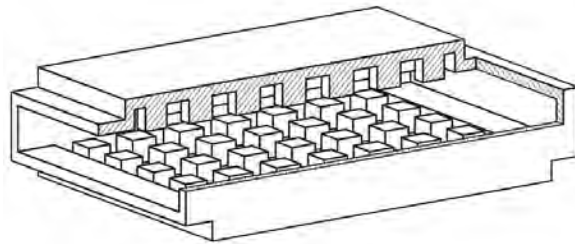


Figure 1.1: Classical waffle-iron filter.

A direct-coupled SIW cavity resonator filter has a wider stopband than conventional metallic waveguide filters because the SIW structure only supports  $TE_{m0}$  and does not support the propagation of TM modes. In the SIW structure, the side walls have physical discontinuities which prevent the longitudinal direction currents to circulate. All of the modes having a  $z$ -directed magnetic field, namely,  $TE_{0n}$  and  $TE_{mn}$ , might present significant leakage losses if excited [5]. The stopband performance can be improved by using symmetric excitation or coupling since even-order modes cannot exist for symmetric coupling [6]. Also, some novel techniques compatible with SIW schemes have been developed to further improve the performance of a direct-coupled SIW cavity resonator filter. In [7] and [8], patterned transverse radiating slots at positions of SIW cavities are used to reject the second-order longitudinal resonant modes. The stepped-impedance resonator scheme, which comes from microstrip resonators, has been successfully used in the direct-coupled SIW resonator filter with a wide stopband [9], [10]. The stepped-impedance resonators implemented by H-plane discontinuities inherently have different spurious frequencies which can degrade the passband. On the other hand, the spurious resonance can shift to a higher frequency by selecting the appropriate length and impedance ratio of the resonator. The second resonance of the fundamental  $TE_{10}$  mode can shift to  $1.5 f_0$  by using E-plane discontinuities to realise the stepped-impedance resonator, similar to the ridged SIW filter [11]. In [12], the cross-coupling technique is used to generate some transmission zeros (TZs) to improve stopband performance, but it is difficult to adjust the coupling coefficients between resonators, and the stopband is also limited to  $2f_0$ . A MSIW approach for suppressing the higher-order modes of bandpass filters is presented in [13]. The vertical coupling schemes are implemented here but only suppress the first higher-order mode  $TE_{102}$ . Substrate integrated gap waveguide (SIGW) technology makes use of slot cavities that enhance transmission zeros and suppress resonance [14]. Substrate integrated folded waveguide (SIFW) technology uses a folded cavity to create a dual-band filter and attenuates some cavity modes in [15]. Unfortunately, until now most of the current designs have narrow bandwidth, less than 20%, and the insertion loss is only in the region of 25 dB in the stopband. It can also be noted that no multimode scattering parameter measurements were conducted in these designs.

### 1.1.2 Substrate integrated waveguide (SIW)

The basic concept of SIW is shown in Figure 1.2, where a waveguide cavity merge with a planar structure on a single dielectric high-frequency material. This is attained by the use of multi-row vias in a substrate dielectric acting as the walls of the waveguide cavity. The top and bottom metallised layers of the high-frequency PCB material, form the upper and lower cavity walls,

while planar transmission lines are used for the RF input and output ports [3].

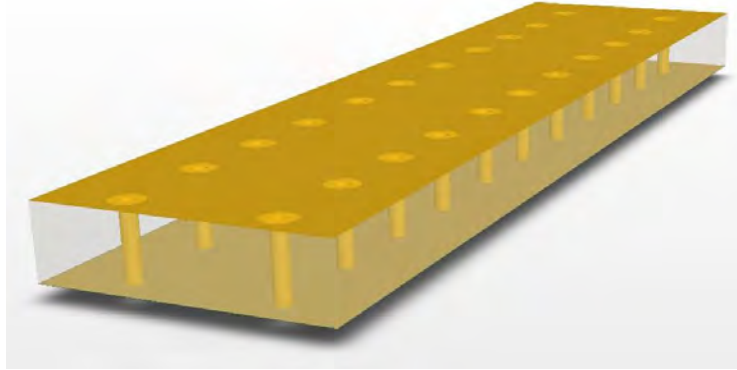


Figure 1.2: Substrate integrated waveguide (SIW) structure.

Various applications can benefit from making use of SIW structures. Depending on the configuration, SIW can be used in antenna arrays and slot antennas [16], [17], [18], [19]. In RF circuit applications, properly adjusted SIW transmission waveguide dimensions, lends itself to the development of various linear phase shifters [20] [21]. Designing of directional couplers, mixers, oscillators and power divider/combiners, are all possible by making use of different configurations of multiple SIW cavities [22], [23], [24], [25], [26], [27], [28], [29].

Recently, SIW technology has become very popular for the design and development of high-performance and cost-sensitive filters over a vast frequency spectrum, ranging from sub-gigahertz to sub-terahertz [30].

Numerous efforts have been made to reduce the physical size of SIW filters. This include folded substrate integrated waveguide (FSIW) [31], half-mode substrate integrated waveguide (HSIW) [32], and evanescent-mode SIW filters [33].

SIW cavities have also been employed to produce higher quality filters, compared to planar configurations, such as dual-mode SIW filters [34], compact super-wide bandpass filters [35], and MSIW filters [36]. Looking specifically at RF front-end designs, RF and microwave filters are characterised by specifications such as low loss, small size, lightweight, low sensitivity to environmental effects (temperature and humidity, for example), high power handling, predefined in-band and out-of-band performance metrics and lower cost.

### 1.1.3 Methods for measuring the scattering parameters of multimode waveguides filters

Characterising multimode waveguide filters, such as waffle-iron filters, can prove to be very difficult and time-consuming. It is difficult because of the contribution of the different modes that have to be separated by using measurements at one physical port, and time-consuming because each mode entails using a different electrical port, creating a multiport device that can only be characterised by a generalised scattering matrix.

Several possible solutions have been proposed in literature to deal with this type of problem. The earliest techniques [37] relied on the use of mode couplers or very long lengths of line to fully utilise the difference in the propagation speed of the various modes. Later a technique using a plunger [38] was proposed to vary the resonance condition of a cylindrical guide cavity for various modes.

The use of probes to sample field strengths along the waveguide walls and the use of Fourier techniques to extract the modal content was also suggested [39]. This approach was further investigated by others [40], [41], [42] to make it more accurate and easier to use. In particular, Levinson et al. [41] documented all their efforts made to determine the relative power distribution of the propagating modes in the waveguide and proposed the use of an enlarged waveguide incorporating a probe section in the cavity to sample the fields along the waveguide walls. A phase-sensitive detector is used to differentiate between the various modes.

During a later period, it was proposed to make use of a liquid crystal sheet [43] to identify modal patterns in a multimode waveguide.

The most accurate broadband measurement technique was presented by Sequinot et al. [44]. They use a multimode thru-reflection line (TRL) algorithm to derive the generalized scattering parameters of a multimode two-port network. Coupled microstrip lines are used as the multiple conductor structure device under test (DUT). The DUT has two physical ports (1 and 2) and each port has  $N$  propagating modes. This requires the characterisation of a  $2N$  port device with the aid of a network analyser. The validity of the algorithm was proven, but a practical calibration kit for microwave probe-based measurements, should still be designed.

Overall much research has been done in this area, but the measurement results are either not accurate over the entire frequency band or the technique requires an immense number of measurements.

## 1.2 Problem Statement

Combining a waffle-iron filter with MSIW technology can offer an important trade-off between size, cost and performance for filters with wide pass- and stopbands. In such a filter, the higher order modes will be attenuated even further due to the use of a dielectric medium. PCB manufacturing processes have improved significantly over the last couple of years, especially pertaining to the tolerance of vias and the alignment between them, making it possible to use either blind or buried vias for the pegs. If using buried vias, then the inner layers of the PCB can be used for the MSIW waffle-iron filter structure, while the outer layers can be populated with other circuit components. Such an approach can reduce PCB size considerably and can make this filter ideal for use in a small, medium power transceiver system that is also very cost-effective.

### 1.2.1 MSIW Implementation

The basic principles to implement a waffle-iron structure in MSIW is shown in Figure 1.3 (a), where a dielectric waveguide (shown in grey) is loaded with rows and columns of blind vias, which will form the pegs of the structure. A 3D-rendering is shown in Figure 1.3 (b), with one prototype shown in Figure 1.3 (c). In order to measure wideband response, this filter will be inserted between two tapered matching networks, as shown in Figure 1.3 (d).

### 1.2.2 Measuring technique

A new method for measuring the multimode scattering parameters of the filter is proposed. A WR90 waveguide with a height of 3 mm, with two manual shifters (tolerance of 10  $\mu\text{m}$ ) attached to it, one to move the back-short, and the second one on the side of the waveguide, to move the 2.4 mm connector across the width of the waveguide. This construction in Figure 1.4 (a) is connected to both sides of the filter through an air-to-dielectric waveguide transition in Figure 1.4 (b). Multiple incident and reflected modes can be measured at both ends.

A look-up table will be used to move each shifter at a time to a different position, covering all possible positions to measure combinations of higher order modes. Also, this structure is symmetrical, which halves the measuring time and because it is one structure, no extra time is used in unfastening and fastening of connectors and structures during every measurement, which is the case in all previously proposed methods.

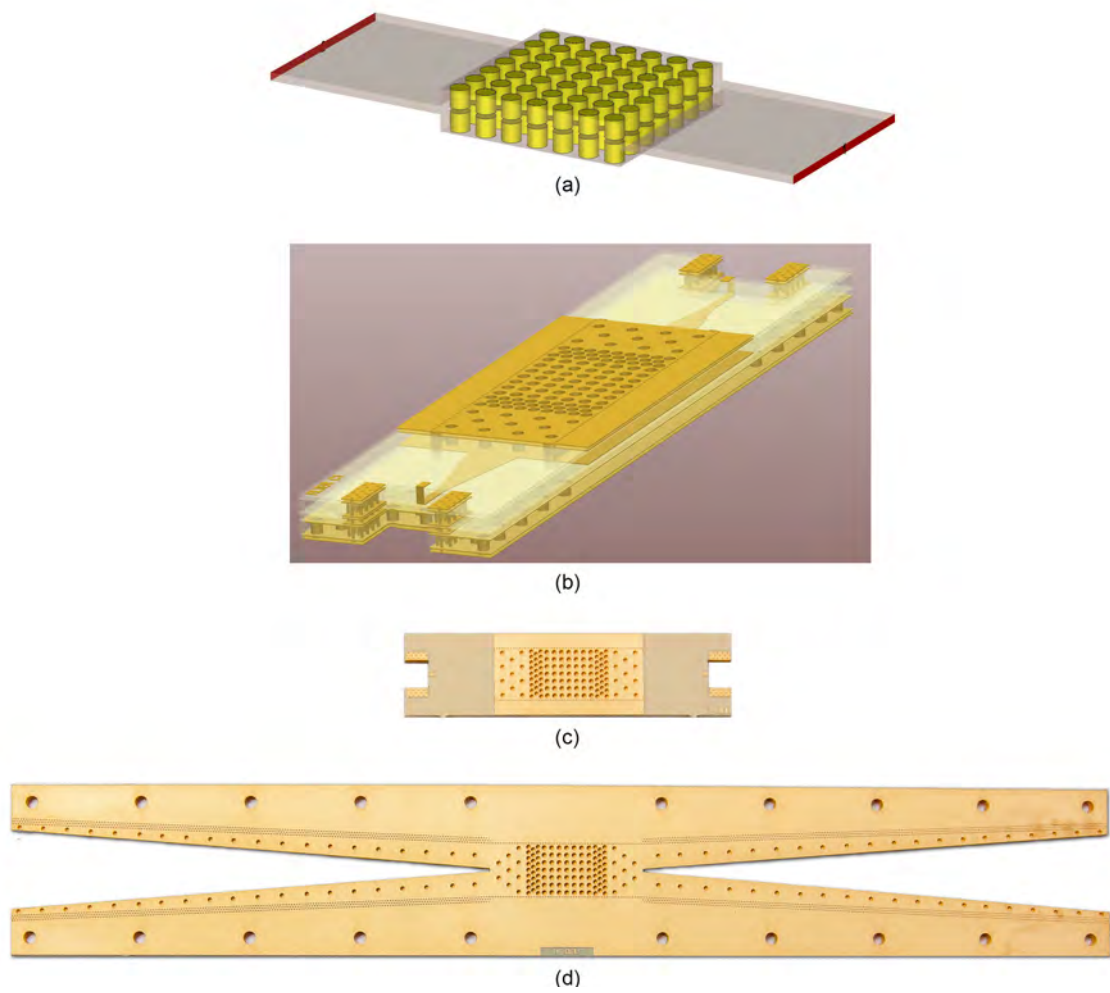


Figure 1.3: MSIW Waffle-iron filter design stages.

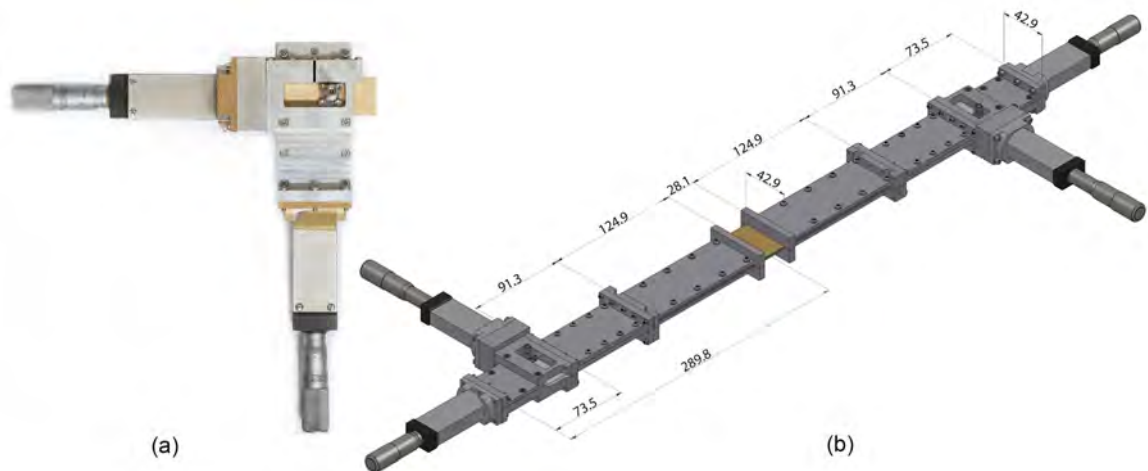


Figure 1.4: Measurement concept.

### 1.3 Original Contributions

The proposed project aims for the following original contributions:

1. The design of a MSIW waffle-iron filter. This will be accomplished by:
  - a) Applying MSIW technology to classical waffle-iron filter design. In particular, a number of manufacturing issues inherent to MSIW will be modelled accurately, and their effects mitigated by the design approach. A basic MSIW structure is shown in Figure 1.5.

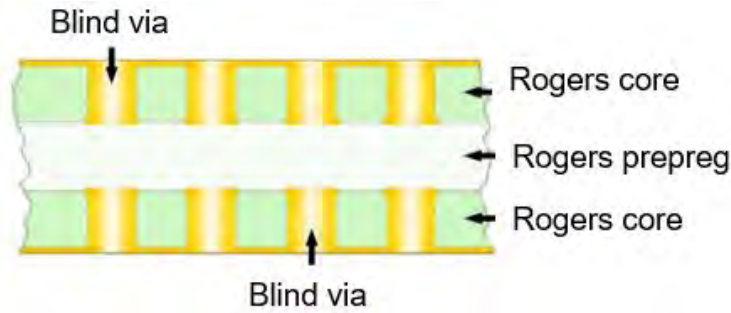


Figure 1.5: Multi-layer PCB with blind vias.

- b) The MSIW waffle-iron filter will be constructed by utilizing more than one core PCB layer, together with prepreg that will be used to bind the core layers. Each extrusion will be realised with a single blind via. An in-depth analysis of the manufacturing process will be conducted during this phase, to establish how accurate the alignment of the extrusions (vias) are and whether, if any,  $TE_{0n}$  or Quasi- $TM_{m0}$  modes arise due to misalignment thereof. In the case of misalignment, a new revision of the existing design will be manufactured, this time adding very thin tracks across the width of the filter in the space between the extrusions (vias) of the filter. This will be done in an attempt to suppress the  $TE_{0n}$  modes.
2. A new calibration and measurement technique will be designed for measuring scattering parameters of multimode waveguide filters. The new technique will measure the entire frequency range, with minimum required measurement iterations. This technique will also be used to measure the manufactured MSIW waffle-iron filter.



## 1.4 Dissertation Outline

Chapter 2 will discuss SIW/MSIW technology used in wide stopband filters and manufacturing process of MSIW. In Chapter 3, the design, modelling, optimisation and the manufacturing of the Waffle-iron SIW filter will be discussed. Two filter versions will be designed namely, filters A and B. Filter A is the classical Waffle-iron filter implemented in MSIW. Filter B is an extended version of filter A, with an extra step in the middle of the filter to extend the bandstop range. The implementation of measuring the passband, multiple propagating modes and power handling response of filter A and B will be examined in Chapter 4. The dissertation will conclude in Chapter 5.

## Chapter 2

# SIW Technology and Manufacturing

### 2.1 Substrate Integrated Waveguide

Substrate Integrated Waveguide technology has become very popular for the design and development of high performance and cost-sensitive filters over a vast frequency spectrum, ranging from sub-gigahertz to sub-terahertz. X.P. Chen and K. Wu published three journal papers in the IEEE Microwave Magazine [3], [45] and [46], where they made a summary of the basic design rules, techniques, innovations and practical considerations.

In Figure 2.1, the SIW is an equivalent rectangular waveguide formed by two solid conductor planes, separated by a dielectric substrate, with conductor side-walls reproduced by rows of metallised through-plated vias [47]. Since the discontinued side-walls do not allow longitudinal current flow, the SIW structure only supports the propagation of quasi-transverse electric (TE) modes that have properties similar to those in a conventional metallic waveguide, of which the dominant mode is  $TE_{10}$ . The transverse magnetic (TM) modes require longitudinal side-wall surface currents to propagate, and if generated or exists along with the structure, TM modes will immediately become leaky through unbounded via windows along the transversal direction. The absence of TM modes creates a very favourable condition for the bandpass filter design because certain mode problems, which may be responsible for out-of-band parasitic response, can be avoided. This is a distinct feature of the SIW technique for filter design. In most cases, the only mode of interest is the  $TE_{m0}$ . This is due to the substrate thickness that is relatively thin compared to that of the SIW width.  $TE_{mn}$  transverse electric modes, where  $n \neq 0$ , require longitudinal side-wall surface currents for efficient propagation.

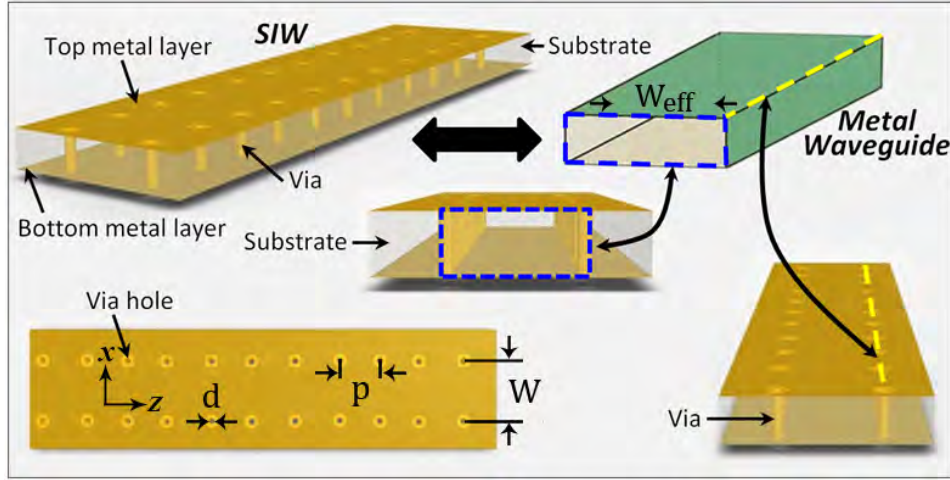


Figure 2.1: The SIW structure and dimensions.

Various wave guidance and leakage characteristics of the SIW were discussed in detail in [48] and [5]. During the design of SIW components, one must ensure that the SIW operates within the frequency band of interest where there are no bandgap effects and leakage loss is negligible over the entire waveguide bandwidth of interest. The SIW is a periodic structure, that is always governed by the bandgap phenomena. The frequency region of interest for the SIW is drawn and described in Figure 2.2. The SIW structure is designed by choosing suitably-spaced vias, all with the same diameter, to support guided wave propagation with minimum radiation loss. The spacing between the vias controls the number of fields leaking out of the waveguide. If the vias are spaced too far apart, the leakage of the SIW will be compromised. This leakage potential sets the limit as to what modes of propagation will be possible within this periodic waveguide. The bandwidth of the bandgap increases when the diameter of the posts decreases. The SIW is designed from standard formulas [47] shown below, where period length ( $p$ ) must be larger than the post diameter ( $d$ ) so that the circuit is physically realisable. The period length ( $p$ ) must be smaller than a quarter of cutoff wavelength to avoid any bandgap in the operating bandwidth. From [47],

$$p > d \quad (2.1.1)$$

$$p/\lambda_c < 0.25 \quad (2.1.2)$$

$$a_l/k_0 < 1 \times 10^{-4} Np/\text{rad} \quad (2.1.3)$$

$$p/\lambda_c > 0.05 \quad (2.1.4)$$

where  $a_l/k_0$  is the total leakage losses as functions of the via diameter and period length normalised to the cutoff wavelength, and  $k_0$  is the wave number in free space. This condition must closely adhere to in order to prevent the leaky-wave and wave-forbidden region in the plane. A more limiting

and general condition for negligible leakage losses is  $p \leq 2d$ . The width of the waveguide is determined by the desired cutoff frequency of the dominant mode.

The vias are usually mechanically drilled and chemically electroplated or plasma deposited, and the production time is directly related to the choice of a processing technique. According to Deslandes et al. [5], if the length of the period is very small, the mechanical rigidity is adversely affected, and it is recommended that  $p/\lambda_c > 0.05$ , with the number of vias not exceeding 20 per wavelength to simplify the fabrication process. As seen in Figure 2.2, the red dot indicates the proposed via diameter per wavelength and spacing between the vias per wavelength, for the designs in this dissertation.

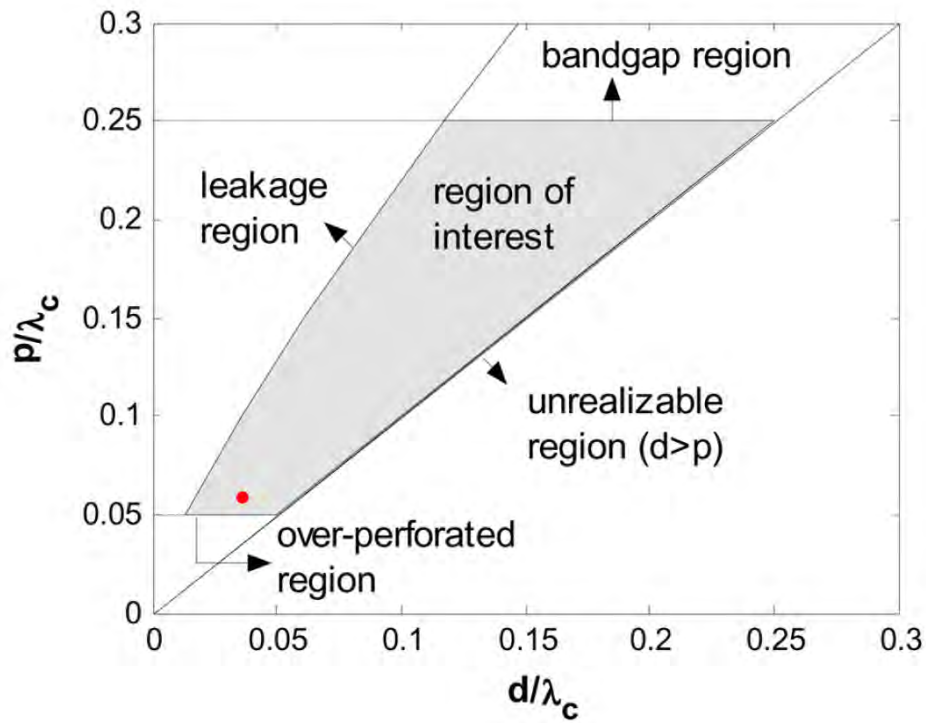


Figure 2.2: Region of interest for the SIW in the plane of  $d/\lambda_c$ ,  $p/\lambda_c$  [5].

If we consider the  $TE_{10}$  mode frequency region that is of interest, the SIW is equivalent to a conventional rectangular waveguide. A rectangular waveguide has negligible losses in terms of leakage and has no bandgap in the specific frequency band for which the filter has been designed. What this entails is that such an equivalence dictates that the physical SIW and its dielectric-filled equivalent rectangular metallic waveguide share the same  $TE_{10}$  mode cutoff frequency and has similar dispersion properties. The equivalent width of the SIW is proposed as follows [47]:

$$w_{eff} = w - 1.08 \times \frac{d^2}{p} + 0.1 \times \frac{d^2}{w}, \quad (2.1.5)$$

where  $p/d$  is smaller than 3 and  $d/w$  is smaller than  $1/5$ . The dispersion characteristics are similar to that of an equivalent rectangular waveguide if one examine the high-order  $TE_{m0}$  modes in the SIW. It can be noted that minor difference do exist in the equivalent width between the higher-order and the fundamental mode [48].

Through this method, the quasi-TE modes of the SIW ( $TE_{10}$  mode, in particular) can effectively be mapped through an equivalent waveguide width that characterise the cutoff frequency. This is effectively accomplished by mapping modes into the dielectric-filled TE waveguide that has solid metallic walls. Well known and familiar design models, analysis equations, and synthesis tools usually associated with rectangular waveguide circuits can be utilized in a straightforward manner in the development of SIW circuits, components and systems.

Currently, for typical PCB fabrication specifications, a through-hole via diameter must be at least a  $10^{th}$  of the PCB's thickness. The spacing hole-to-hole between vias should be at least 0.15 mm, but it depends upon the specific bare-board fabricator.

## 2.2 PCB Manufacturing for MSIW

In this work, the aim is to show that waffle-iron filters can be realised in MSIW, using normal PCB processes. It is, therefore useful to briefly touch on the basics of the PCB process, especially the steps that can lead to errors in a MSIW structure. The PCB fabrication process is a highly complex balance of electrical, chemical and mechanical process steps that must all come together in the right way, at the right time, in order to produce a successful PCB. There is no such thing as a "standard" PCB, and each board has its own unique set of challenges.

Parameters that contribute to error, in no specific order, include but are not limited to:

1. Environmental temperature,
2. Saturation levels of the chemicals used during the fabrication process,
3. Accuracy of the imaging process,
4. Consistency of the water pressure during processing,

5. Operator's skill level,
6. Copper utilisation on the PCB panel,
7. Other boards that are in the same processing bath at that specific instance,
8. External contaminants that get into the processing bath,
9. Machine tolerances and variations,
10. Wear and tear of instruments, probes and drill bits.

It is often surprising to designers to learn that, the CAM-engineer 'compensates' the design in order to increase yield. This compensation off-set the error inherent to the specific fabricator. He has characterised his equipment and can therefore introduce offsets to facilitate an accurate reproduction of the electronic data.

From the layout, artwork is fabricated on film by means of a highly accurate printer that prints the positive or the negative image onto film material. A process called "direct imaging" may also be employed. This process reduces refractive error in the imaging process where traditional film is used and rather "prints" the image directly onto the PCB copper.

The bare board laminate is cut to the fabricator's panel size. This laminate consists of either fibreglass, ceramic or PTFE material, depending on the specific parameters required. The laminate is covered usually on both sides with copper sheeting. Following the cutting, alignment holes are drilled so that the individual cores can be accurately aligned in the successive steps. The accuracy of these holes, often called tooling holes, are paramount to the success of the final boards' construction.

Once the laminates used for this specific board has been cut and drilled, the laminates are covered with photo-resist. Photo-resist is a light-sensitive coating that is used in the process of transferring the image to the copper surface. The film is placed under vacuum and exposed to UV light. Wherever the artwork has been inked, no UV will reach the photo-resist, and the opposite is true for the non-inked or clear parts of the artwork. The UV interacts with the photo-resist and changes the properties of the coating. Next, a developer is used to wash away any exposed regions leaving the exposed bare copper on the laminate. All these steps are done in a clean-room environment as any contaminants can lead to a degraded end product.

The next process is the etching process where acid is used to remove the bare exposed copper. The photo-resist protects the traces from being attacked by the acid, although this process needs utmost attention to not cause over or under etching. Over etching is caused by exposing the laminate to the acid for too long, so that the acid eats in under the photo-resist. Under etching is the phenomenon where the exposure to the acid is too short, and not all the copper has been etched away.

Once etched, the inner layer laminate is inspected with an AOI machine that compares the artwork to the visioning system of the machine and identifies regions of error within a specific tolerance window. An operator can remove small errors with a scalpel. If the error level is too high, the laminate is scrapped, and the process starts over. This is repeated for each inner-layer set of laminates.

A 4-layer PCB, for example, typically consists out of 1 inner-layer pair of laminates with prepreg and copper foil on the outer layers. This is called an inside-out build and is shown in Table 2.1. Another way of producing a 4-layer board is by using two sets of inner-layer pair laminates without the additional prepreg and outer copper layers, as seen in Table 2.2. This is called a sequential build but requires more processing steps and is more costly.

Layer Name	Type	Material	Thickness (mm)	Dielectric Material	Dielectric Constant
Top Overlay	Overlay				
Top Solder	Soldermask	Surface Material	0.01	Solder Resist	3.5
Layer 1	Signal	Copper	0.035		
Prepreg	Dielectric	Prepreg	0.238	FR4 Prepreg 1080+7628	4.2
Layer 2	Internal Plane	Copper	0.035		
Core	Dielectric	Core	0.93	FR4 Tg 150 0.93mm 35/35	4.2
Layer 3	Internal Plane	Copper	0.035		
Prepreg	Dielectric	Prepreg	0.238	FR4 Prepreg 1080+7628	4.2
Layer 4	Signal	Copper	0.038		
Bottom Solder	Soldermask	Surface Material	0.01	Solder Resist	3.5
Bottom Overlay	Overlay				

Table 2.1: Layers for an inside-out build.

Another critical parameter to consider is copper roughness in high frequency applications. The copper is bonded to the laminate to form a core substrate. This is then used with prepreg in a final PCB build. It is advantageous if the copper surface closest to the laminate is rough as this improves adhesion to the laminate and prevent de-lamination, but from an RF point of view, this roughness increases the length substantially for the surface current and therefore increases the loss.

Layer Name	Type	Material	Thickness (mm)	Dielectric Material	Dielectric Constant
Top Overlay	Overlay				
Top Solder	Soldermask	Surface Material	0.01	Solder Resist	3.5
Layer 1	Signal	Copper	0.035		
Core	Dielectric	Core	0.238	FR4 Tg 150 0.51mm 35/35	4.2
Layer 2	Internal Plane	Copper	0.035		
Prepreg	Dielectric	Prepreg	0.93	FR4 Prepreg 7628*2+1080	4.2
Layer 3	Internal Plane	Copper	0.035		
Core	Dielectric	Core	0.238	FR4 Tg 150 0.51mm 35/35	4.2
Layer 4	Signal	Copper	0.038		
Bottom Solder	Soldermask	Surface Material	0.01	Solder Resist	3.5
Bottom Overlay	Overlay				

Table 2.2: Layers for a sequential build.

There are two ways of adding copper to the laminate or substrate material:

1. Rolled or annealed copper
2. Electro-deposited copper

To add to the complexity, the copper can be treated in various ways before adhesion too, yielding two different end results in the circuits' performance.

Also, as can be seen in the exaggerated Figure 2.3, the rough sides are facing each other on a laminated sheet, and with SIW filters, this may influence the insertion loss. Simonovich [49] modelled conductor surfaces using the cannonball stack principle. He used different sphere model variations to design formulas that can be incorporated into the SIW design model that will take the copper roughness into account.



Figure 2.3: Cross-sectional view of microstrip, exaggerated copper roughness image.

Once all the inner-layer laminates have been etched, the board needs to be laminated. During this phase, the inner-layer laminates are "glued" together with prepreg. Prepreg is usually made from the same homogeneous material than the inner-layer laminate but contains more resin than fibres. The laminates and prepreg are placed in a press that, under pressure and elevated temperature, heat and squeeze the sheets together to form a single PCB. During this stage, the laminates are heated to the glass transient temperature ( $T_g$ ) where the laminate turns from a rigid to a rubber-like structure. During this stage, many things can go wrong in the processing from copper migration,



misalignment or even de-lamination. For a waffle-iron filter, the vertical gap between pegs is of critical importance, therefore the lamination stage is also critical.

After verifying the laminating stage with an x-ray process, the board is sent to the drilling stage where the plated holes will be processed. On this filter PCB, an additional step had to be performed called, depth-drilling. Depth drilling is the process by which the drill is mechanically taken to a specific depth from the top surface of the board. What makes this process difficult is the fact that the pressed board is not entirely flat over the whole surface.

The various factors that contribute to the exact final depth of the drilled hole can be summarised, in no particular order:

1. Drilling machine tolerance.
2. Planarity across the whole area of the panel.
3. Operator's ability to accurately set the depth and then monitor the subsequent drilled depths across the panel width.

The drilling machine, having a  $50\text{ }\mu\text{m}$  tolerance, in this case, must be set to ensure that the depth-controlled drill does not penetrate the next layer in the substrate. Ideally, the drill must stop as soon as it touches the copper. Figure 2.4 illustrates on the left, the blind via touching the inner layer pads and on the right-hand side, the blind via not touching the inner pads. It will later be shown that this has an enormous effect on the waffle-iron filter performance.

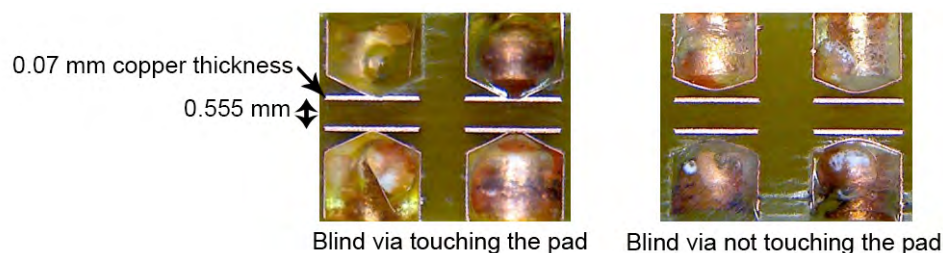


Figure 2.4: Depth-controlled drilling results.

After drilling both through-hole and depth-controlled holes, graphite is pushed into the holes and through the holes under extreme pressure. This creates the electrical pathway for the electroplating process to deposit copper on the board, effectively plating the hole with conductive copper.

Because not all the holes are going right through the board, washing the solution through those holes can be tricky, and a process called reverse pulse plating must be used in order to wash the plating solution in and out of the hole until the hole is plated with copper.

The panel has to be plated to insure the conductivity of the holes. Plating is controlled to achieve about 5-8  $\mu\text{m}$  of copper in the holes on the panel. In Figure 2.5, a section of the via is not plated.

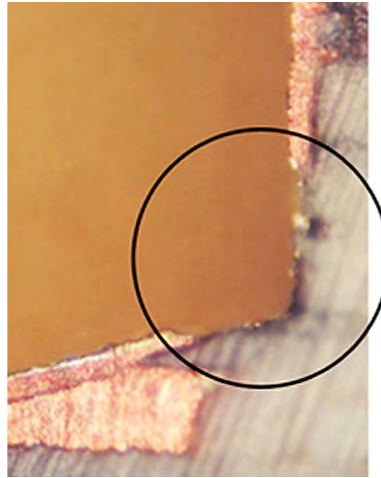


Figure 2.5: Un-plated section in a blind via.

Following the initial panel plating process, the outer layers are again covered with photo-resist and the outer image is transferring using the process step described earlier during the inner-layer imaging process. After etching the board goes back to the plating line where the pattern plating is performed.

Because the outer layer plating happens during the plating of the holes, a starting copper thickness needs to be chosen that is less than the desired final copper thickness of the outer layers and hole-wall thickness. Laminates come in standard 1/4 oz (12  $\mu\text{m}$ ), 0.5 oz (18  $\mu\text{m}$ ), 1 oz (35  $\mu\text{m}$ ) and 2 oz (70  $\mu\text{m}$ ) thicknesses. In the case of this filter board, a starting copper of 1 oz was chosen (35  $\mu\text{m}$ ). After pattern plating, the resultant copper thickness on the outer layer would be approximately 55  $\mu\text{m}$  with a hole wall plating thickness of 20-25  $\mu\text{m}$ .

An additional technology employed in this PCB design is the process called edge plating. This process is performed by routing a thin slot with a 0.8 mm drill bit and then applying shadow and plating to the slot. A specialised cutter

is then used to route through the plated slot so that only a thin copper conductor remains. This is a specialised process that must be carefully controlled because the graphite/copper plating can easily tear off the laminate during the subsequent routing process. Figure 2.6 shows edge planting that was properly done.

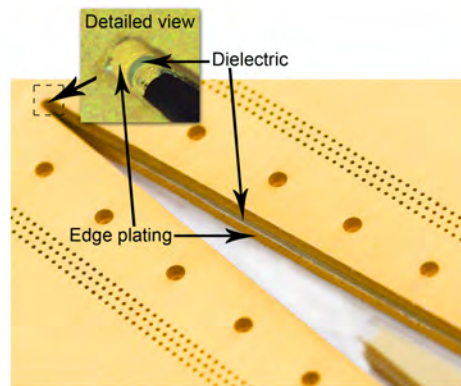


Figure 2.6: Edge plating.

Usually, in a bare board fabrication process, the next step would be to cover the board with a polymer called solder resist. This serves two purposes:

1. Stop solder from flowing on the copper surface during the assembly process.
2. Protect the volatile copper surface from exposure to air and oxidation.

A second process, using the same polymer called legend printing, is used to add text on top of the solder resist. This is typically used to identify and name components on the board. Because this development board did not require these steps, it was skipped in its entirety.

To protect the copper from air and subsequent oxidation, a final processing step occurs. Various options exist, and the decision on the final finish is driven by various factors documented below:

1. HASL - Hot Air Solder Levelling, where the board is dipped in a molten tin bath and blown off with hot air "blades". This process is not commonly used any more due to the fine pitch of modern packages. This is not the preferred option for RF or fine pitch technology boards (package pitch below 0.65 mm).
2. Immersion-Tin - This finish offers good shelf life and surface planarity, but because of the tin content, can lead to tin-whisker growth. For

RF applications, due to tin's low conductivity, this is not the preferred solution.

3. Immersion-Silver - Although silver offers good conductivity and surface planarity, the complexity in applying this process, makes it costly. Also, the boards do not have a very long shelf-life and should be stored in a very controlled manner and assembled within a few weeks of production.
4. Immersion-Gold - Most good PCB fabricators will offer this solution to their clients. Excellent planarity and good conductivity, due to the gold, makes this solution the preferred option for most type of boards, including that of RF designs. The one drawback is that under the extremely thin layer of gold (1-2  $\mu\text{m}$ ) there is Nickel that acts as a metallurgical barrier between the gold and copper. The conductivity of Nickel is not so good and taken skin-depth into consideration, most of the RF signal will propagate in the Nickel itself increasing loss.
5. ASIG or Autocatalytic Silver Immersion Gold offers superior performance both in terms of surface planarity as well as RF performance. In this process, silver replaces the Nickel so the RF signal will propagate primarily through silver which has a much higher conductivity than Nickel.

Next, the board profile needs to be cut out. Because the PCB is cascaded or panelised in the fabrication panel, the boards need to be separated. Board profiling can be performed through 3 technologies:

1. Scoring - V-groove scoring is the process where a specialist v-like cut is made from the top and the bottom, leaving about 1/3 of the material thickness. The board can then be excised using a tool similar to that of a pizza cutter called the v-groove separation tool to separate the individual board from the panel.
2. Routing - This is done with a precision CNC machine fitted with a specialist cutter designed for cutting through tough PCB material. The operator needs to carefully control the speed of the cutting process. Cutting too slowly will reduce factory through-put and also place additional wear and tear on the cutting surface. Cutting too fast can cause flexing and even snapping the cutting bit, forcing the whole process to come to a halt. Because the hardness of each type of material varies, the factory heavily relies on experience and skilled operators to be involved during this part of the process.
3. Punching - The process involves the making of a punching tool with sharpened edges that press through the board at high speed using a specialised press. Punching, due to the physical-mechanical impact, can

leave holes fractured and the board compromised. This process is, therefore, not recommended.

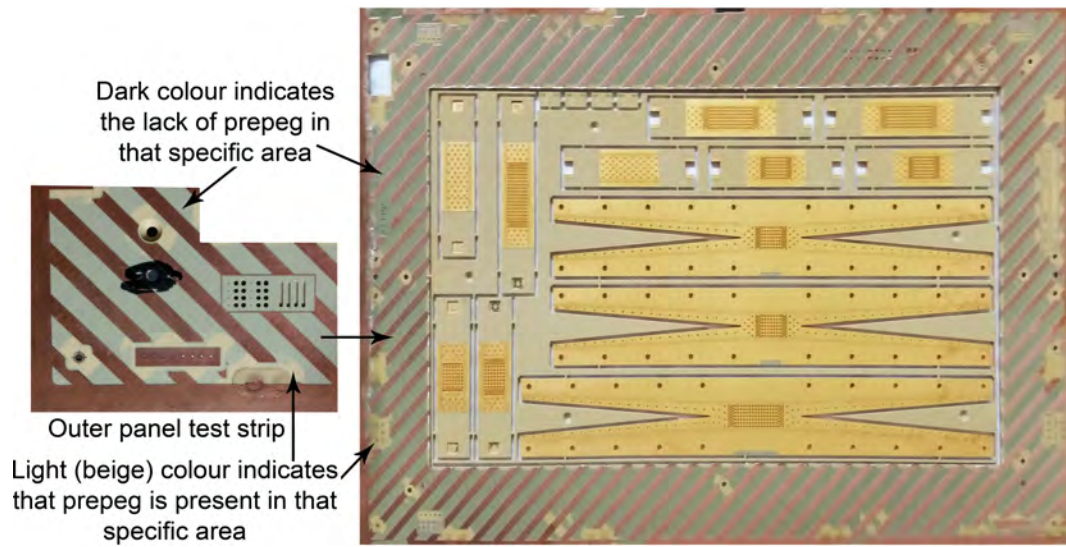


Figure 2.7: PCB manufacturer panel.

The panelisation needs to be carefully designed in order to take the profiling step into account. This includes leaving enough material between the boards in order for the CNC bit to excise the board profile while still maintaining sufficient mechanical integrity in the fabricated PCB panel. Figure 2.7 shows the complete Waffle-iron filter panel. The outer section of the panel is used for in-house testing to make sure that the prepreg was enough and any additional tests.

## Chapter 3

# SIW Waffle-Iron Filters

### 3.1 Introduction

Seymour B. Cohn et al. were the first to invent the Waffle-iron lowpass filter at the Stanford Research Institute in 1957 [50], [51], [52]. It is a popular solution for harmonic suppression due to the wide stopband, typically covering up to four times the cut-off frequency [53], which may be extended even further by cascading two or three waffle sections [54]. Figure 3.1, shows the classic waffle-iron with square pegs. The classical structure consists of a uniform multi-ridged rectangular waveguide, with equal width transverse grooves, forming rows and columns of rectangular pegs on the waveguide floor and ceiling. Since the spacing between opposing peg ends are typically less than full-height waveguide, the filter is matched using stepped or tapered E-plane sections.

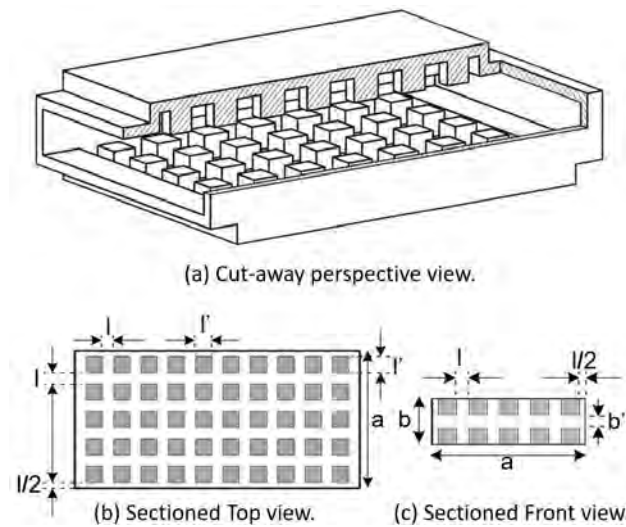


Figure 3.1: Cut-away perspective view of the Classical waffle-iron filter.

Two classic synthesis methods exist for waffle-iron filters. The first method is based on Cohn's corrugated waveguide filter data [55] and the second is Marcuvitz's models for waveguide stubs [56]. Both methods use the image impedance methods to match a specific periodic section below a cut-off frequency  $f_1$ , and pick an infinite attenuation frequency  $f_\infty$  below an upper stop-band frequency  $f_2$ , as shown in Figure 3.2. The passband occurs below  $f_c$ , and the stopband between  $f_1$  and  $f_2$ . No transmission or reflection is required between  $f_c$  and  $f_1$ , which makes this a so-called "buffer-band" between the transmitted and rejected bands.

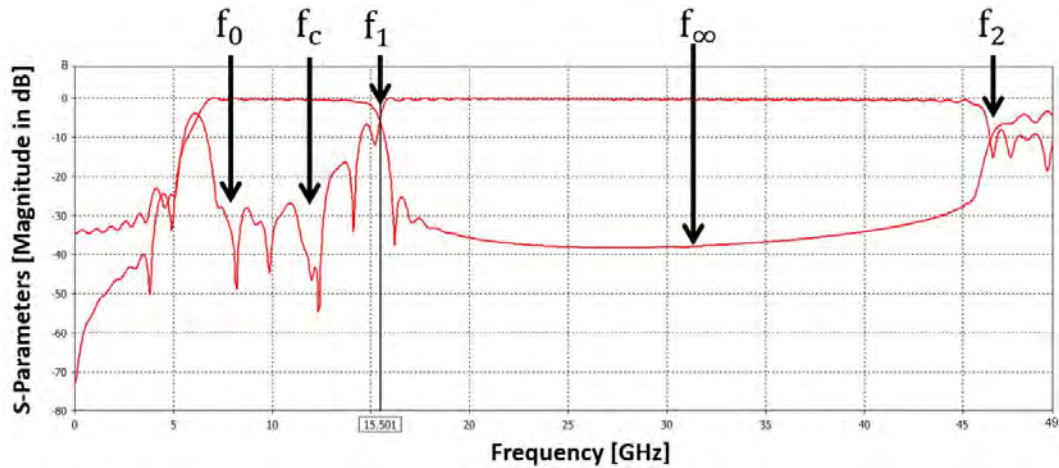


Figure 3.2: Definition of frequencies  $f_0$ ,  $f_c$ ,  $f_1$ ,  $f_\infty$  and  $f_2$  for waffle-iron filters.

The classical waffle-iron filter consists out of square pegs, but power handling capability can also be increased by replacing the sharp edges with rounded corners [57], as seen in Figure 3.3, by reducing the maximum  $\vec{E}$ -field around the sharp corners, which increase the power handling capability by 30% [54].

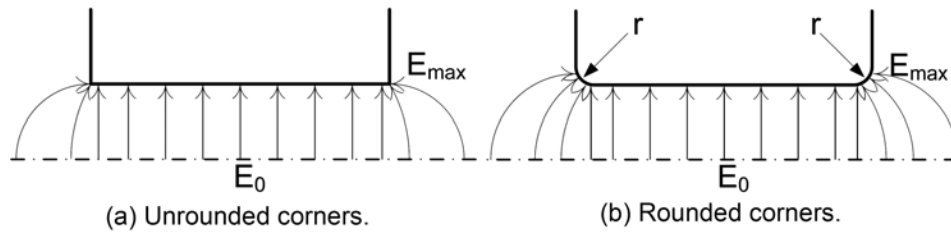


Figure 3.3:  $\vec{E}$ -field patterns with unrounded and rounded corners [58].

One big constraint in waffle-iron filters is the alignment of the pegs.  $TE_{0n}$  modes are higher-order modes which should not, in theory, be excited in the waffle-iron filter due to the symmetry of the structure. However, in practice,

they are caused by poorly mating waveguide flanges or misaligned extrusions. These spurious modes can be suppressed by adding thin rods across the width of the filter in the air gap between the extrusions, as shown in Figure 3.4. This is a more cost-effective solution compared to paying the premium for high precision engineering, which results in a more robust design that can readily be repeated in a consistent fashion [2].

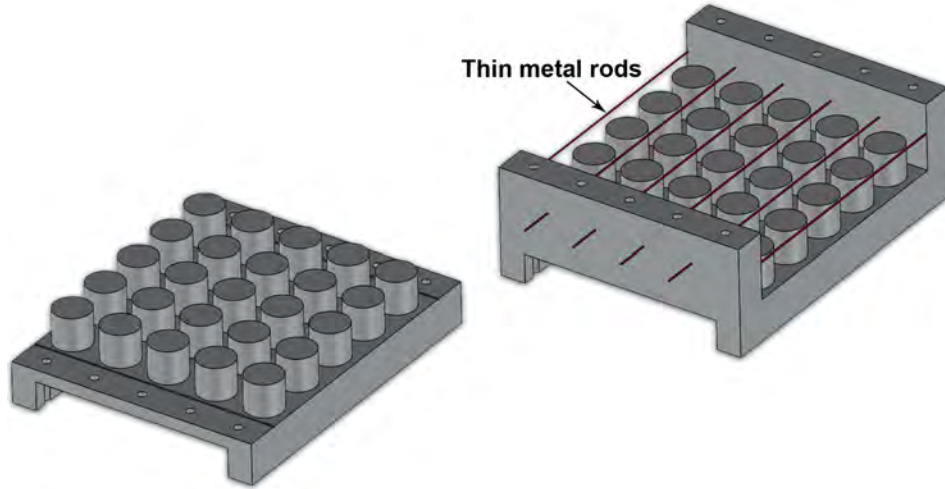


Figure 3.4: Waffle-iron filter with thin rods to suppress  $TE_{0n}$  modes.

Quasi- $TM_{m0}$  modes, for even values of  $m$ , may also be excited due to misaligned pegs that appear asymmetrical with respect to the  $H$ -plane (as shown in Figure 3.5), exciting an  $x$ -directed  $\vec{E}$ -field component. Since they rely on manufacturing tolerances, they are not revealed in the typical full-wave analysis, unless the misalignment is simulated specifically. [58].

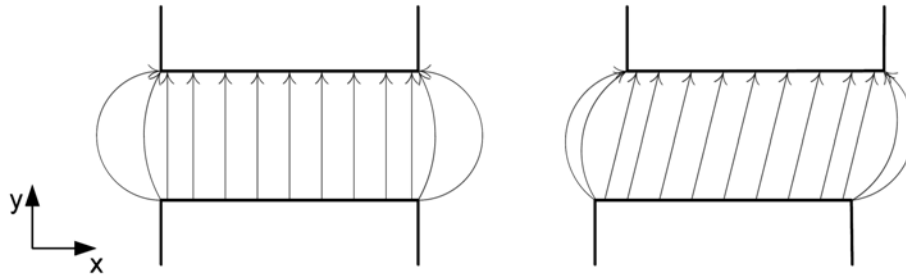


Figure 3.5:  $\vec{E}$  fields for aligned (left) and misaligned (right) extrusions [58].

Unfortunately, both classical synthesis methods, outlined in [2], only allow for the synthesis of a specified stopband, with no direct control over passband



response. It is considered good practice to choose the upper stopband frequency  $f_1 > 1.43 f_c$ , the actual highest required transmission frequency.

In recent years CAD solutions have been developed [59], [60], [61]. The waffle-iron filter is modelled by a series of general scattering problems or solved utilising hybrid mode-matching (MM) / finite element method (FEM), which allows transversal grooves to be optimised for both adequate stopband response, as well as equiripple transmission across a defined frequency band. Traditional synthesis methods are, however, used for initial values [61].

One of the focuses for the proposed dissertation is to examine Cohn's and Marcuvitz's methods [2], select the appropriate method and apply MSIW technique to create a PCB waffle-iron filter. The proposed design will be ideal for applications such as satellite systems where the design must be compact, light-weight, and where the average transmitted power will not be more than 10 Watts.

## 3.2 Design approaches for Waffle-Iron filters

### 3.2.1 Cohn's method

The first design step in Cohn's method [2], is to design a corrugated waveguide filter to achieve the required stopband, replacing references to guide wavelength  $\lambda_{g0}$  by free-space wavelength  $\lambda_0$ . Once the transversal groove widths (forming the corrugations) are determined, identical longitudinal grooves are placed. Also, the spacing between two opposing solid ridges in a corrugated waveguide filter is reduced to  $b'$ , to compensate for the decrease in shunt capacitance of the discontinuity. The image impedance calculations rely on the circuit model shown in Figure 3.6. The transmission lines of alternating impedance  $Z_1$  and  $Z_2$  represent the sections of reduced height and full height (of  $b'$  and  $b$ ) waveguide of lengths  $l$  and  $l'$ , respectively. The shunt capacitance  $C_2$  compensates for transition effects, and  $C_1$  for capacitance between two adjacent corrugations.

According to Young et al. [57], bridging the gap between two opposite pegs (one vertical above the other) form the shunt capacitances of the low pass filter, storing electric energy. There is also a series-inductance effect due to magnetic energy stored between the neighbouring horizontal pegs.

Secondly, there are electric fields that are mostly horizontal, bridging the gap between two neighbouring pegs. These electric fields result in a bridging capacitance across the series inductance. This forms a parallel resonant circuit that theoretically causes infinite attenuation at some frequency. This infinite-

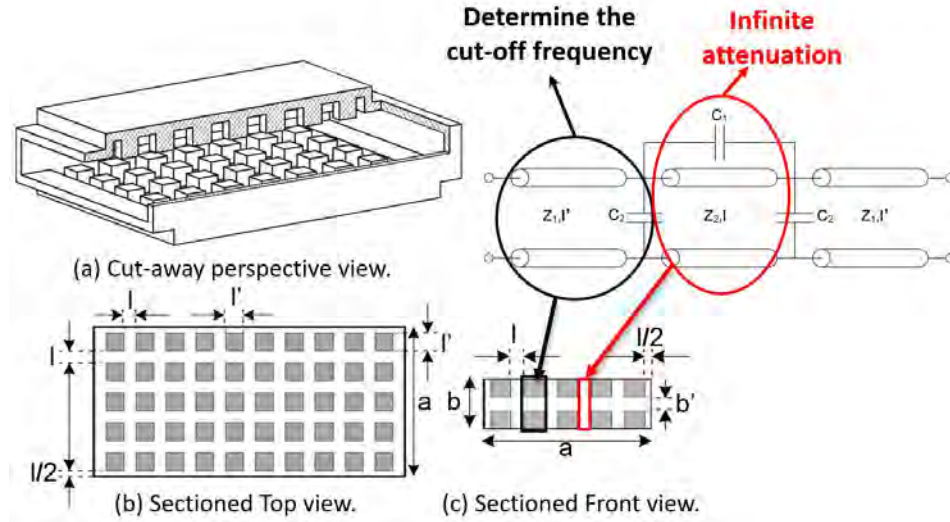


Figure 3.6: Cohn's corrugated waveguide filter model, single section.

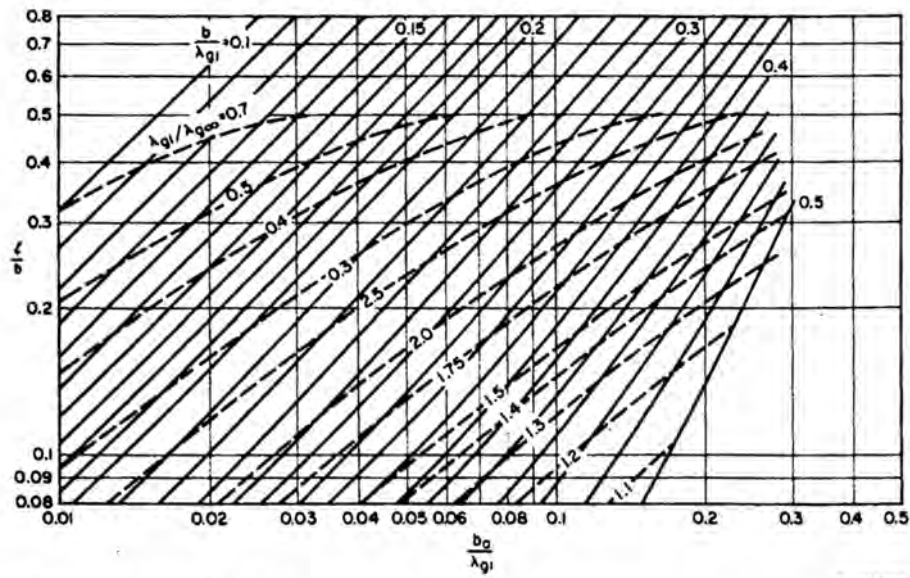
attenuation frequency is above the cut-off frequency of the filter because the filter structure is designed so that the fields between neighbouring pegs are weaker than the fields between opposite pegs.

The following steps define the Waffle-iron filter's design procedure using Cohn's design graph published in [2] starting from page 386.

1. Start by choosing the upper limit cut-off frequency  $f_c$  and upper stop-band frequency  $f_2$ .
2. Choose  $f_1$  and  $f_\infty$ , based on the rule of thumb  $f_1 > 1.43f_c$  and  $f_\infty \approx 0.8f_2$ .
3. Next, select values for  $b$  and  $l/b$ .
4. Use the selected values in step 3, as well as  $\lambda_1/\lambda_\infty$ , to find  $b_0/\lambda_1$  and  $b/\lambda_1$  from Figure 3.7. Calculate  $b_0$ ,  $b$  and  $l$  next. Here  $b_0$  is the terminating guide height which will match the filter as  $\lambda_g$  approaches infinity.
  - a) Repeat steps 2-4 above until the desired values for  $b$  and  $l$  are found.
5. With the aid of Figure 3.8, calculate parameter  $G$  in terms of  $l/b$  and  $b/\lambda_{g1}$ . A value of  $\delta \leq 0.20$  can be assumed to determining  $l'$  in the following equation.

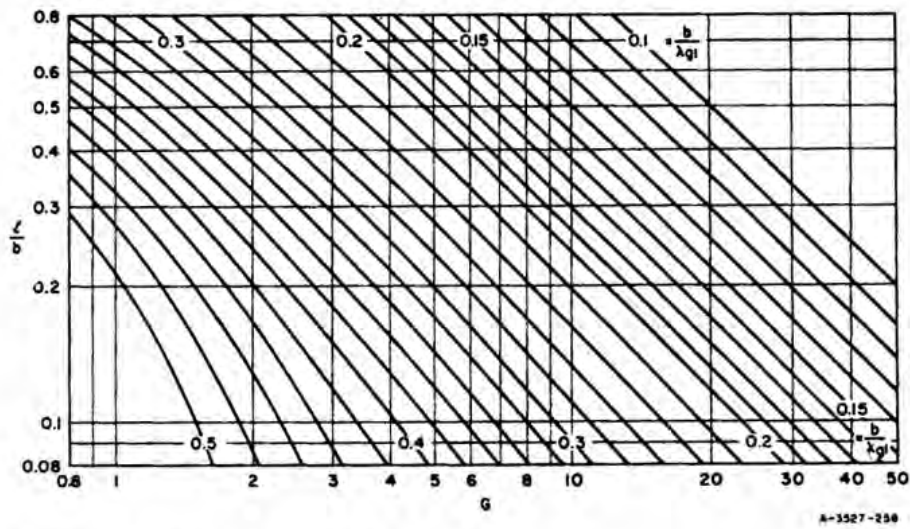
$$\tan \frac{\pi(l')}{\lambda_{g'}} = \pi\delta \frac{b}{\lambda_{g1}} \left[ G - \frac{2}{\pi} \ln \frac{1}{\delta} + 0.215 \right] \quad (3.2.1)$$

- a) Repeat steps 2-5 until a satisfactory value of  $l'$  is found.



Source: Proc. IRE (See Ref. 7 by S.B. Cohn)

Figure 3.7: Design graph giving the parameter  $b_0$  [2].



SOURCE: Proc. IRE (See Ref. 7 by S. B. Cohn)

Figure 3.8: Design graph giving the parameter  $G$  [2].

6. Use the following equation to calculate the  $b_T$ , the height of the main

guide providing an optimal match to the waffle-iron filter.

$$b_T = \frac{b_0}{\sqrt{1 - \left(\frac{\lambda_{g1}}{\lambda_{gm}}\right)^2}} \quad (3.2.2)$$

7. The following equation is used to calculate the boss spacing  $b'$ .  $b''$  is the spacing between two opposing solid ridges in a corrugated waveguide filter.

$$\frac{b''}{b'} = \frac{l'}{l + l'} + \frac{2}{\pi} \left( \frac{l}{l + l'} \right) \left[ \tan^{-1} \left( \frac{b'' b'}{b' l} \right) + \frac{\ln \sqrt{1 + (lb'/b'b'')^2}}{\frac{l}{b'} \frac{b'}{b''}} \right] \quad (3.2.3)$$

- a) Repeat steps 2-7 until a satisfactory value of  $b''$  is found.

### 3.2.2 Marcuvitz's method

In Marcuvitz's method, filter dimensions are also in terms of free-space (rather than  $TE_{10}$  waveguide mode) wavelength. The transversal grooves are not, however, modelled as sections of high impedance transmission lines, but rather lengths of short-circuited series waveguide stubs. An electric wall is placed in the H-plane between the bosses, to simplify the analysis [56].

The design process has many similarities compared to Cohn's method, with initial selections of the relevant frequencies and dimensions  $b'$ ,  $l'$  and  $l$ . Dimension  $b$  is chosen to ensure the stubs have an equivalent length (with consideration to the shifted reference plane) of  $\lambda_\infty/4$ .  $f_1$  and  $f_2$  can be calculated using Equations (2) to (4) of [62]. This process is repeated (with adjustments to  $b'$ ,  $l$  and  $l'$ ) until a satisfactory stopband response is found. Dimension  $b''$  is calculated using the same equation as step 7 in Cohn's method [2]. Finally,  $b_T$  (the terminating guide height) calculated using the following equation from [2]:

$$b_T = b'' \frac{Z_I}{Z_O} \quad (3.2.4)$$

Cohn's method is only accurate for  $l/b' > 1$  and Marcuvitz's for  $l/b' \leq 1$ . Also, the manufacturing process is highly dependant on the specific manufacturer and his capabilities. With these restrictions and current PCB manufacturing constrains, enough space ( $l$ ) must be allocated between the blind vias (pegs). Due to the aforementioned reasons, the design of the MSIW waffle-iron filter in this work, will only considered Cohn's method.

### 3.3 MSIW Implementation of Waffle-Iron Filters

Two filter versions will be designed; namely, filters A and B. Filter A is the classical MSIW Waffle-iron filter. Filter B is an extended version of filter A with an additional step in the cavity, reducing the height,  $b_1$ , in the centre of the filter. The purpose of the step in filter B is to increase the stopband even further.

#### 3.3.1 Basic structure

The basic structure for filter A is described in Figure 3.9. In the classic metal waffle-iron filter, shown on the left in Figure 3.9(a), rectangular extrusions are used to form the pegs. In contrast, a MSIW waffle-iron filter as seen on the right of Figure 3.9 (b) and (c), use metallised structures known as vias, to form the pegs.

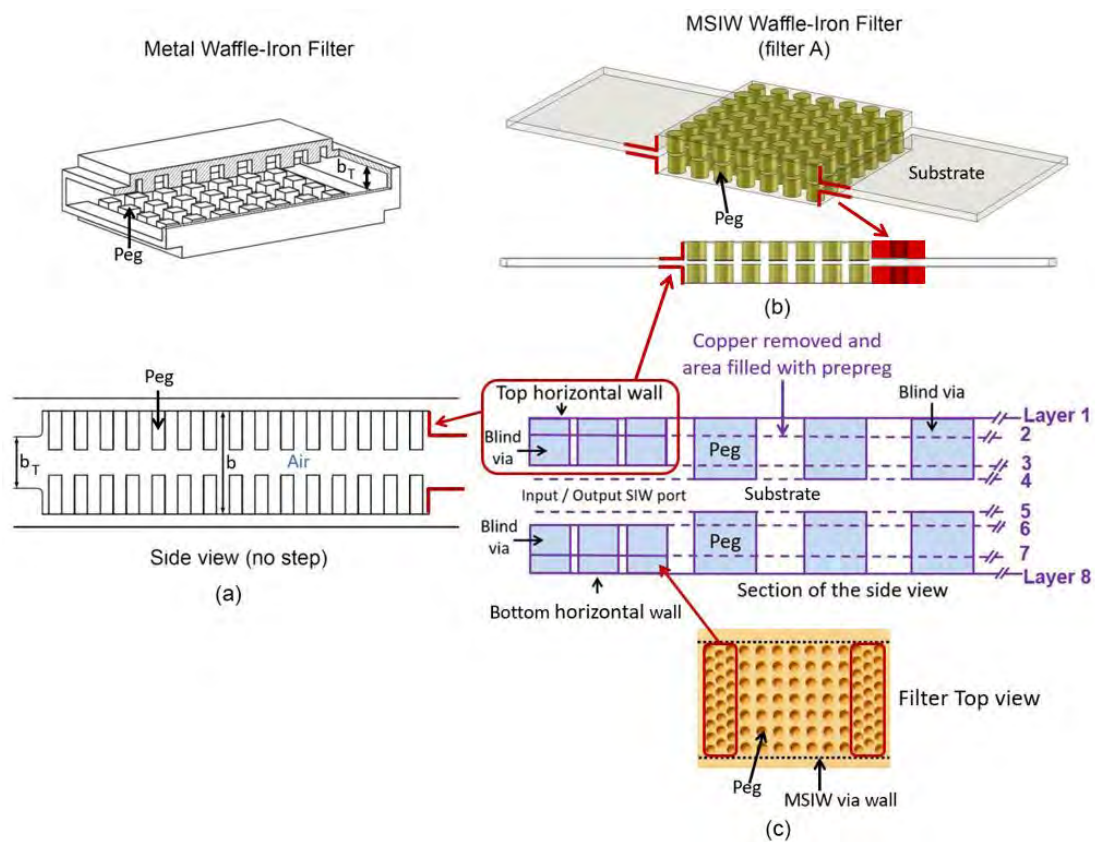


Figure 3.9: Filter A.

In the metal waffle-iron filter the metal that is not machined away, before and after the pegs, forms an impedance step. In a MSIW filter, one way of constructing this wall is to make use of staggered vias, spaced in three rows to ensure that minimal leakage occurs as the electrical wave propagates through the filter structure. Side-walls along the filter structure are placed according to SIW formulas.

Some limitations when it comes to MSIW waffle-iron filters are, (1) the fact that blind vias need to maintain a 1:1 aspect ratio, meaning that the via needs to be as wide as it is deep. This creates a physical limitation on the design of the filter. (2) There are more variations in the depth, position and diameter of vias compared to machined pegs; this will be viewed later in the chapter. The vertical gap between the pegs and their lengths is also very dependent on the process of lamination.

Additionally, it can be noted that for the classic metal waffle-iron filter, the dielectric medium is air compared to that of a MSIW waffle iron-filter that has some dielectric material through which the wave propagates.

In the extended version, filter B, as can be seen in Figure 3.10 the height of the cavity was reduced by adding two additional copper layers. These copper sections are stitched to the ground plane, on the top and the bottom, to prevent the  $TE_{m0}$  modes from propagation in this region. The result is a narrower channel through which the  $TE_{m0}$  modes must propagate, thus increasing the stopband even further.

It will be shown later in Chapter 4 that Quasi- $TM_{m0}$  modes, for even values of  $m$ , are not excited in a SIW waffle-iron filter, even if the pegs are misaligned with respect to the  $H$ -plane.  $TE_{0n}$  modes are also not excited due to the height of the MSIW Filter.

Lastly, let's consider the input and output sections of the filters. A lumped element equivalent of a stepped impedance filter model uses inductors as an equivalent of high impedance lines, and capacitors to represent sections of low impedance line [63]. In waffle-iron filters, the transversal grooves (which correspond to sections of high impedance line, under Cohn's stepped impedance line model description) are referred to as inductive sections, whereas sections of transversal rows of pegs are referred to as capacitive sections. Classical waffle-iron filter peg patterns are designed to terminate at either side with either half-width ( $l/2$ ) transversal grooves, or half-width ( $l'/2$ ) rows of bosses, as shown in Figure 3.11. This is referred to as half-inductive and half-capacitive terminations, respectively. Half-inductive input and output sections will be used instead of half-capacitive sections. The comparative responses of a uniform filter with half-inductive and half-capacitive terminations, done by Stander et



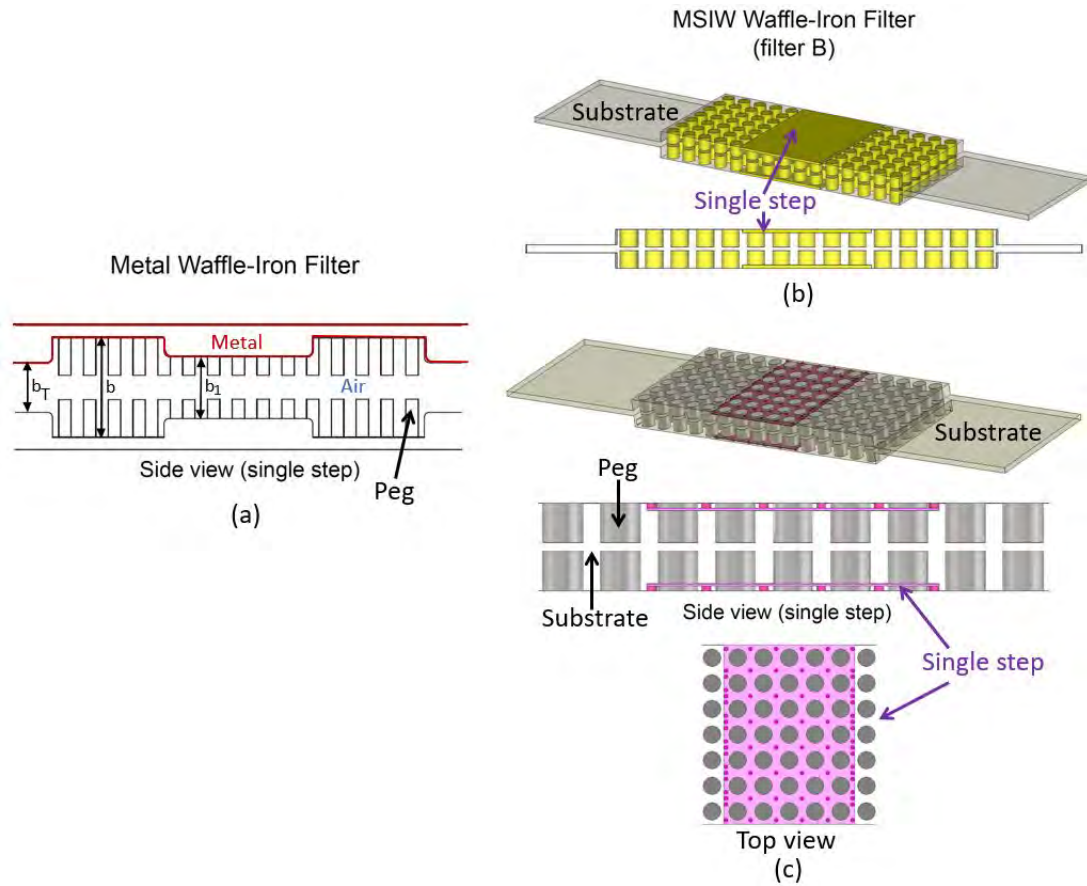


Figure 3.10: Filter B.

al. [58], showed that half-inductive filter exhibits a bandwidth improvement in both transmission band and stopband, as well as lower in-band reflection response. The reduced buffer band in the half-capacitive filter, has the advantage to improve power handling, which is not the purpose for this design. Also, it is not practical to manufacture a via half in this type of application.

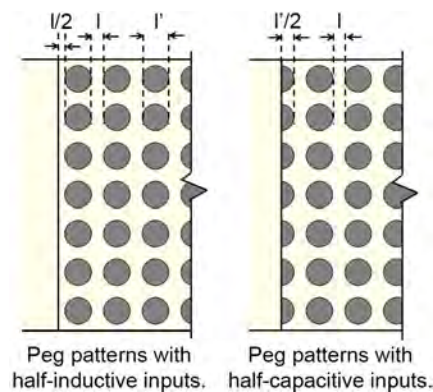


Figure 3.11: Half-inductive and half-capacitive input sections.

### 3.3.2 PCB Stack-up Design

Each PCB manufacturing company has its own PCB manufacturing process and rules, and it changes on a regular basis. Currently one of the manufacturing tolerances that influence this design process, is that the depth to width ratio of a blind via, the filter's pegs, cannot exceed a 1:1 ratio. Also, when choosing a small through-hole via, the via's width must be bigger than a tenth of the PCB thickness.

*Mercurywave<sup>TM</sup>* 9350 core material, with a dielectric constant ( $\epsilon_r$ ) of 3.55, offers a wide core thickness range while also satisfying all other specifications. Appendix A shows the dielectric constant with frequency and temperature; and the necessary specifications.

Figure 3.12 shows the selected eight-layer stack-up. Eight layers were chosen to accommodate filter B, and one panel was used for all the filters to reduce manufacturing cost, as seen in Figure 3.13. The stack-up is made out of dielectric sheets, each consisting out of a top and bottom 70  $\mu\text{m}$  copper foil, and prepreg between each dielectric sheet. It is important to note that the pressed thickness of the final board will vary, depending on the percentage copper utilisation on the inner-layers. The reason for this is because prepreg is heavily doped in resin and acts as the glue binding the different cores together. During the pressing cycle, the resin changes state from a solid to a soft glue (called the glass transient state or  $T_g$ ), and the resin flows in the gaps between the copper conductors, hence collapsing the separation that previously existed. In other words, if we were to strip all the copper from the two inner layers, the stack-up would have to be altered to include an additional two layers of 1080 prepreg in order to fill the void left by the 70  $\mu\text{m}$  copper foil and maintain the original layer separation. If no additional prepreg layers are added, the pressed thickness will reduce from 0.082 mm down to 0.030 mm.

During the first prototype (batch 1), Immersion Gold was used, but during the second prototype (batch 2) it was elected to not have any finish due to the fact that in this specific experimental set-up, the RF will only propagate between the copper of the inner layers. Also, the skin depth will range between 0.729  $\mu\text{m}$  to 0.292  $\mu\text{m}$ , over the frequency band 8 to 50 GHz. The copper coating is 20  $\mu\text{m}$ , this means, plating the bare board would not contribute to the filter's performance and only leads to the increased cost of the board and processing complexity. Care was taken to package the board in a vacuum until the assembly house could solder the test connectors on the board. This reduced the risk of oxidation, and great care was taken to ensure that the board was adequately cleaned before soldering.



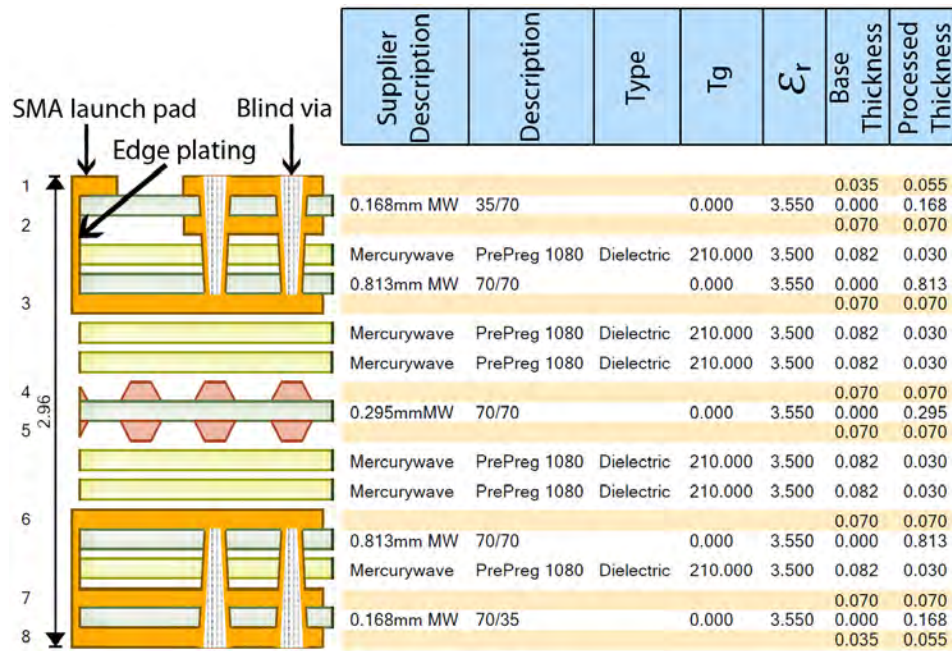


Figure 3.12: PCB stack-up.

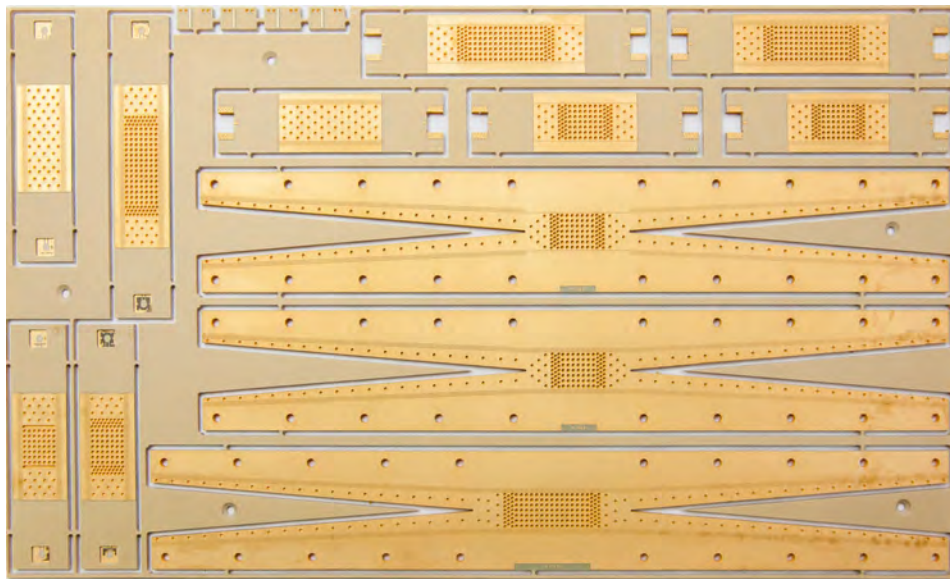


Figure 3.13: PCB panel.

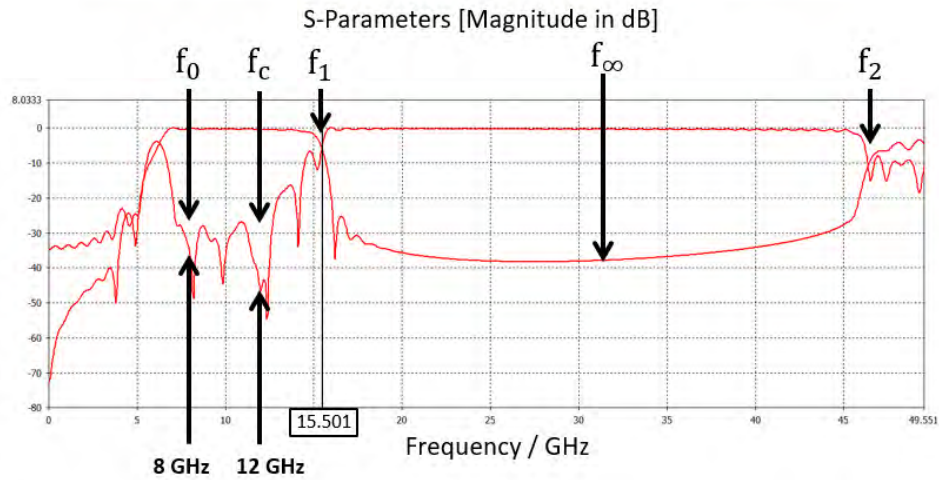
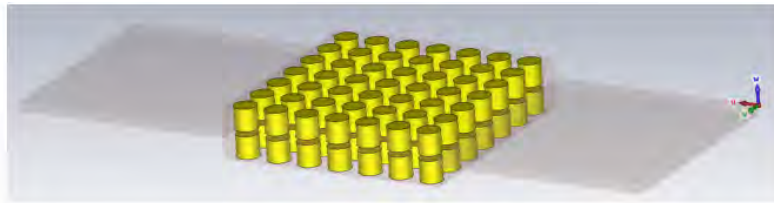
### 3.3.3 Design example

The MSIW waffle-iron filter will be placed after the transmitter amplifier in a low power X-band satellite communications system. The following subsections will describe the complete filter design procedure for filter A and B. Table 3.1 specifies the design specifications for filter A and B.

	Filter A	Filter B
Transmission Band	8 - 12 GHz	8 - 12 GHz
First Stopband	17.5 GHz	17.5 GHz
Second Stopband	43 GHz	48 GHz
$f_{\infty}$	33.6 GHz	33.6 GHz
Average Power	10 Watt	10 Watt
$S_{21}$ Attenuation flatness (passband)	< 1 dB	< 1 dB
Attenuation in stopband	> 70 dB	> 70 dB

Table 3.1: Design specifications for filter A and B.

Filter A will be designed as seen in Figure 3.14, by altering Cohn's method with MSIW design rules and following the manufacturing tolerances.

Figure 3.14: Frequencies  $f_0$ ,  $f_c$ ,  $f_1$ ,  $f_{\infty}$  and  $f_2$  for waffle-iron filter A.

The main difference between Cohn's method and the proposed method is that only the design graph for parameter  $b_0$  is used. Also, the peg's height must be equal or smaller than the peg's diameter, and with this in mind, two equations are created to calculate the total height of the filter  $b$ . Finally, a 3D solver is used to optimise the final design.

The following design steps will be used:

1. Choose the upper cut-off frequency  $f_c$  and upper stopband frequency  $f_2$ .
2. Select frequencies  $f_1$  and  $f_\infty$ , based on the rule of thumb  $f_1 > 1.43f_c$  and  $f_\infty \approx 0.8f_2$ .
3. Calculate the width ( $w$ ) of the SIW. Use the formulas in Chapter 2.
4. Determine the number of pegs ( $n$ ) per row. It has been shown in [2], that 5 pegs give a 3:1 stopband width.
5. To satisfy the 1:1 diameter vs. depth requirement for the manufacturing process, the distance between the adjacent pegs is defined as,  $l \leq \frac{l'}{2}$ . Therefore, the equation  $w/n = (l + l')$ , change to:

$$w/n \leq \left(\frac{l'}{2} + l'\right) \quad (3.3.1)$$

with  $l'$  and  $l$  becoming,

$$l' \geq \frac{2w}{3n} \quad (3.3.2)$$

$$l = \frac{w}{n} - l'. \quad (3.3.3)$$

6.  $l/b' > 1$ , thus  $b' < l$ .
7. Two equations will be used to estimate a value for  $b$ , namely

$$b = (2l' + b') \quad (3.3.4)$$

$$(3.3.5)$$

where the value for  $b'$  is chosen to be much smaller than  $l$  and

$$b < (2l' + l) \quad (3.3.6)$$

8. Choose values for  $b$  and  $b'$ .
9. Calculate  $\lambda_1$  and  $\lambda_\infty$ . Because this design is for MSIW and the dielectric is enclosed, use the following equation to calculate  $\lambda_1$  and  $\lambda_\infty$

$$\lambda_n = \frac{c}{f_n \sqrt{\epsilon_r}} \quad (3.3.7)$$

using  $n = 1$  and  $n = \infty$ .

10. Use the two chosen values for  $b$ , together with  $l$ ,  $\lambda_1$  and  $\lambda_\infty$  and determine  $\lambda_1/\lambda_\infty$ ,  $l/b$  and  $b/\lambda_1$ . Use Figure 3.15 to calculate two estimated values for  $b_0$ . The value for  $b_0$  closest to the  $\lambda_1/\lambda_\infty$  line will be selected as the initial simulation value.
11. By using a 3D MW solver (CST Microwave studio), insert these estimated values,  $b_0$ ,  $b'$ ,  $b$ ,  $l$  and  $l'$ , as parameters into an ideal filter model and then optimise.
12. Using the optimised values calculated, construct a practical model by using different dielectric sheets and prepreg thickness.
13. After the practical model in has been optimised, calculate the SIW parameters  $p$ ,  $d$  and  $d/p$ .

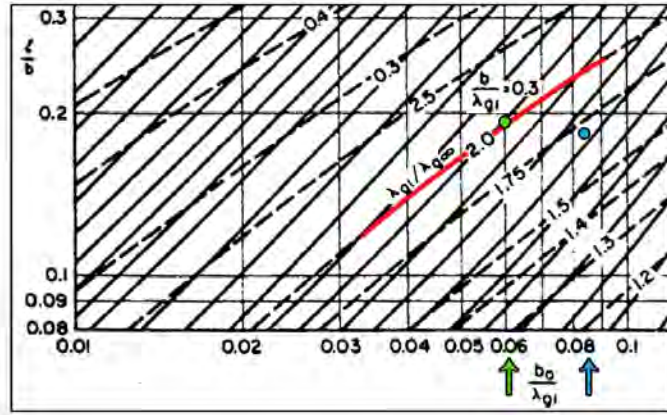


Figure 3.15: Filter parameter  $b_0$  selection [2].

Following the design steps above, an estimated set of dimensions have been calculated, and the results are shown in Table 3.2. For this dissertation, an X-band SIW was designed using a  $TE_{10}$  cut-off frequency of 6.557 GHz. Each peg's diameter must be 1:1 ratio with the blind via's depth, thus  $b \approx 2l' + b'$ .

Table 3.2: Estimated dimensions of filter A.

$f_c$	12 GHz
$f_2$	43 GHz
$f_1$	17.5 GHz
$f_\infty$	33.6 GHz
$w$	13.125 mm
$n$	7
$l'$	$\geq 1.25$ mm (1.3 mm chosen)
$l$	0.575 mm
$b'$	$< 0.575$ mm (0.5 mm chosen)
$b$	$< 3.1$ mm (2.8 mm chosen for Option 1, smallest value)
$b$	$< 3.175$ mm (Option 2, largest value)
$\lambda_\infty$	4.74 mm
$\lambda_1$	9.1 mm
$\lambda_1/\lambda_\infty$	1.919
$b_0/\lambda_1$	0.06 (Option 1, closest to $\lambda_1/\lambda_\infty$ )
$b_0/\lambda_1$	0.085 (Option 2)
$b_0$	0.546 mm
$p$	0.90 mm
$d$	0.50 mm
$d/p$	0.556 mm

After the parameters were optimised in CST Microwave studio, the values were used to select a PCB stack-up using the available dielectric thicknesses from the manufacturer. The manufacturer only stocks standard thicknesses, and this means that the final design parameter values may change. After verifying the new values through optimisation, the altered values are shown below:

Table 3.3: Final dimensions of filter A.

$f_1$	15.501 GHz
$l'$	1.3 mm
$l$	0.6 mm
$b'$	0.295 mm
$b$	2.857 mm (no finish)    0.967 mm (ASIG finished)
$b_0$	0.555 mm

In filter B, the stopband is extended further by applying a different value of  $b$ , namely,  $b_1$  for a number grooves inside the filter without changing the spacing  $b'$  between the pegs. The Equations for this method can be viewed in [58]. Dimension  $b_1$  is implemented by adding two extra layers to the PCB stack-up; one below the top layer and one layer above the last or bottom layer.



The extended area on each layer is filled with an uninterrupted copper plane, connected with small blind vias to the top and bottom layers respectively, as is illustrated in Figure 3.16. The extra layer consists of a 9.5 mm long copper plane on layer 2 and is 0.168 mm below the layer 1 (top side) and also 0.168 mm above layer 8 (bottom side) on layer 7. The total height for  $b_1$  is 2.381 mm.

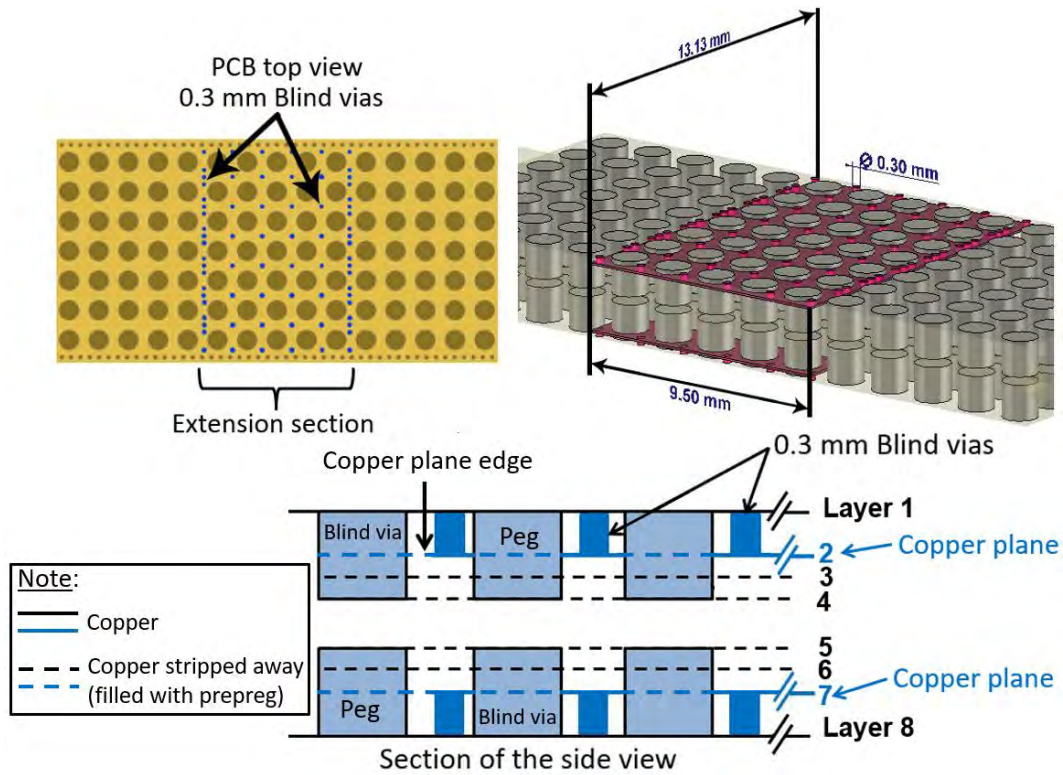


Figure 3.16: Filter B with blind vias in the extension section.

Figure 3.17, shows the ideal  $f_1$  frequency for Filter B.  $f_1$ ,  $f_0$ ,  $f_c$ ,  $f_\infty$  and  $f_2$ , are identical to Filter A and therefore the same design parameters will be used.

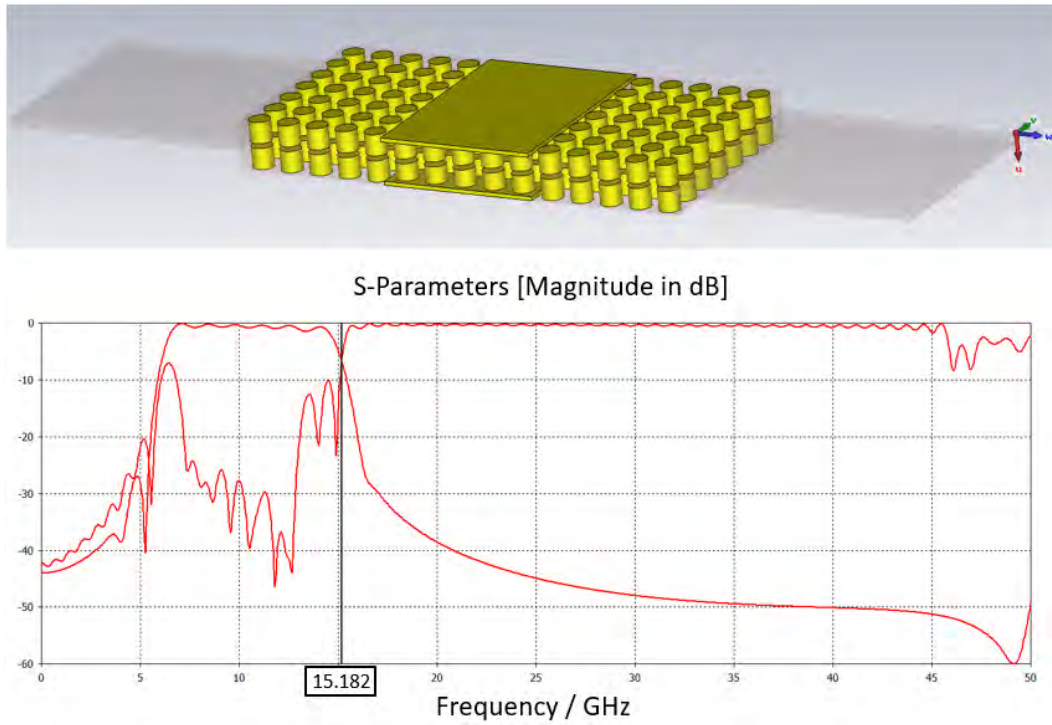


Figure 3.17: Filter B.

### Horizontal walls

As mentioned before, the spacing between opposing peg ends is typically less than the full-height waveguide, and the filter is matched using stepped or tapered E-plane sections. The reason for this is that incident modes having horizontal components of electrical field can excite slot modes that will propagate through the longitudinal slots in the filter at frequencies where the height  $b$  is greater than one half a free-space wavelength. These modes can create problems at the highest stopband wavelength, but unslotted step transformers are used to match the waffle-iron filter to a waveguide of the standard height. The reduced height of the stepped transformers effectively suppresses the incident modes with horizontal components of an electric field which could otherwise excite slot modes in the filter [2].

The proposed filter design does not make use of stepped transformers but uses a single horizontal wall step to shield the pegs from the input and output ports. This wall can be constructed in one of two ways: (1) a depth controlled routed slot or (2) a triple staggered blind via row. Both methods use the blind via concept and were electroplated to create an electrical wall as seen in Figure 3.18.

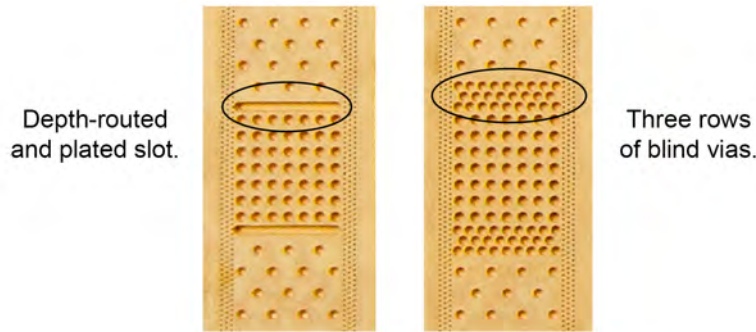


Figure 3.18: Routed slot and blind via walls.

In Figure 3.19, it is shown that the triple staggered blind vias are connected between layers 1 and 3, forming the top wall step and from layer 8 to 6, to form the bottom wall step. The filter consists out of 8 Layers, the purple lines (in the drawing) shows all the different layers, the dashed lines show where copper has stripped away on the plane (layer), and the solid lines show where copper is not stripped away. Solid lines also show the copper of the blind vias. The white lines in the two micro-section photos show the copper planes. A  $70\text{ }\mu\text{m}$  copper foil was selected for each copper layer to minimise the risk of drilling into the copper layer, seeing that the drill tolerance is  $+100\text{ }\mu\text{m}$ ,  $-50\text{ }\mu\text{m}$ . Only two of the triple staggered blind via rows are visible because the micro-section was made through the middle row of filter pegs in the  $z$  direction. Prepreg becomes a "jelly" state when it is warm-up, just before the laminates are pressed together, and the copper plane and pads can move around during this process. The micro-section on the left (yellow dash lines) shows layers 2,3,6 and 7 stop just before the half-inductive termination. In the micro-section on the right (yellow arrows), it is evident that layers 2 and 3 moved. Unfortunately, nothing can be done to prevent this from happening. The PCB top view shows the filter section with seven rows of blind vias, forming the filter's pegs, and three staggered rows of blind vias on each side of the filter section forming the single horizontal wall step.

Both the triple cascading via wall and the depth controlled routed slot, show satisfactory results but a longer slot may be problematic to the manufacturer.



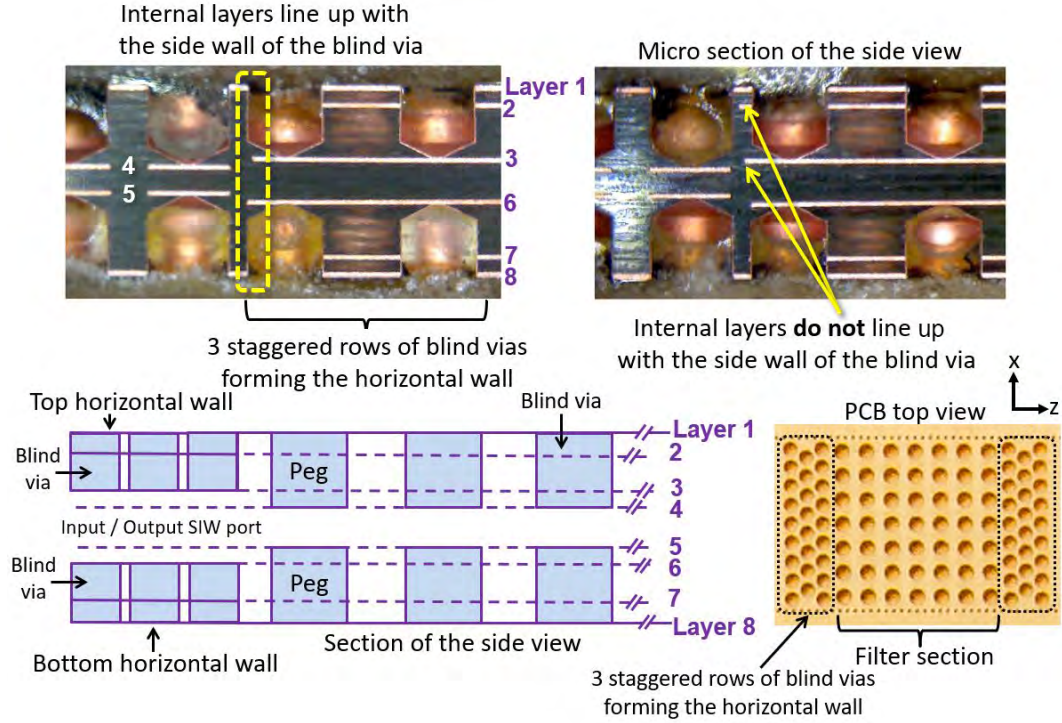


Figure 3.19: Horizontal walls using three staggered rows of blind vias.

## 3.4 Design of transitions

### 3.4.1 Coax to SIW transition

The passband and stopband of the waffle-iron filter will be measured using two different measurement designs. SMA to SIW transition, utilising an ultra-wideband coaxial-to-buried SIW transition, is proposed to measure the passband response ranging from 8 GHz to 12 GHz ( $B_F = 0.4$ ). According to [64], signals having fractional bandwidths ( $B_F$ ) greater than 0.25 are UWB as seen in Table 3.4.

Several ultra-wideband (UWB) SIW transitions to other planar transmission lines have been proposed, e.g. transitions to coplanar waveguide (CPW) [65], stripline [66], grounded coplanar waveguide (GCPW) [67], [68] and slotline [69]. For normal microstrip or stripline transitions to inner layers, a simple via is typically used, but for buried SIW, such an approach causes a reduction in bandwidth due to the large layer separation between the coaxial feed and the buried SIW structure.

A coaxial transition using an embedded microstrip line and an edge plated track is used to connect a coaxial SMA connector to a SIW structure on an inner layer is proposed here. The transition is suitable for ultra-wideband use,

Band Type		Fractional Bandwidth $B_F = 2 \frac{f_h - f_l}{f_h + f_l}$
Radar / Communications	Electromagnetic Interference	
Narrowband (NB)	Hypoband (NB)	$0.00 < B_F \leq 0.01$
Wideband (WB)	Mesoband (MB)	$0.01 < B_F \leq 0.25$
Ultra-Wideband (UWB)	Sub-Hyperband (SHB)	$0.25 < B_F \leq 1.50$
	Hyperband (HB)	$1.50 < B_F < 2.00$

Table 3.4: Modified Classification Scheme for Devices/Signals based on Bandwidth [64].

and easy to manufacture. Measurement results show a back-to-back return loss of better than 15 dB across a bandwidth of 8-12 GHz, with insertion loss between 1.0 and 1.5 dB.

This design requires a transition from a coaxial connector on the top layer, to the SIW structure on the inner layer. Figures 3.20, 3.21 and 3.22 illustrate the construction of the proposed transition, with the inner conductor of the SMA connector connecting to a short microstrip line, which is connected through edge plating to an embedded microstrip line on an inner layer. The use of edge plating instead of a via is at the core of the proposed transition, and is the element responsible for the improved performance.

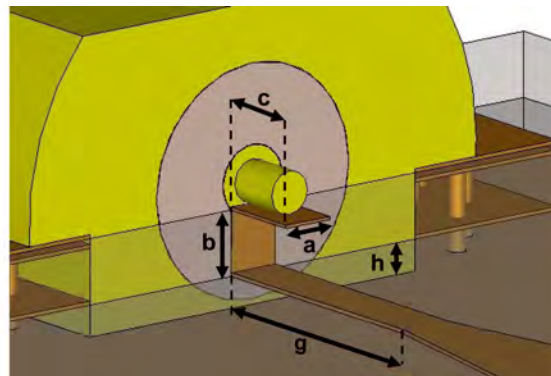


Figure 3.20: 3D view of the multilayer PCB with a SMA edge mount connector to an UWB SIW transition.

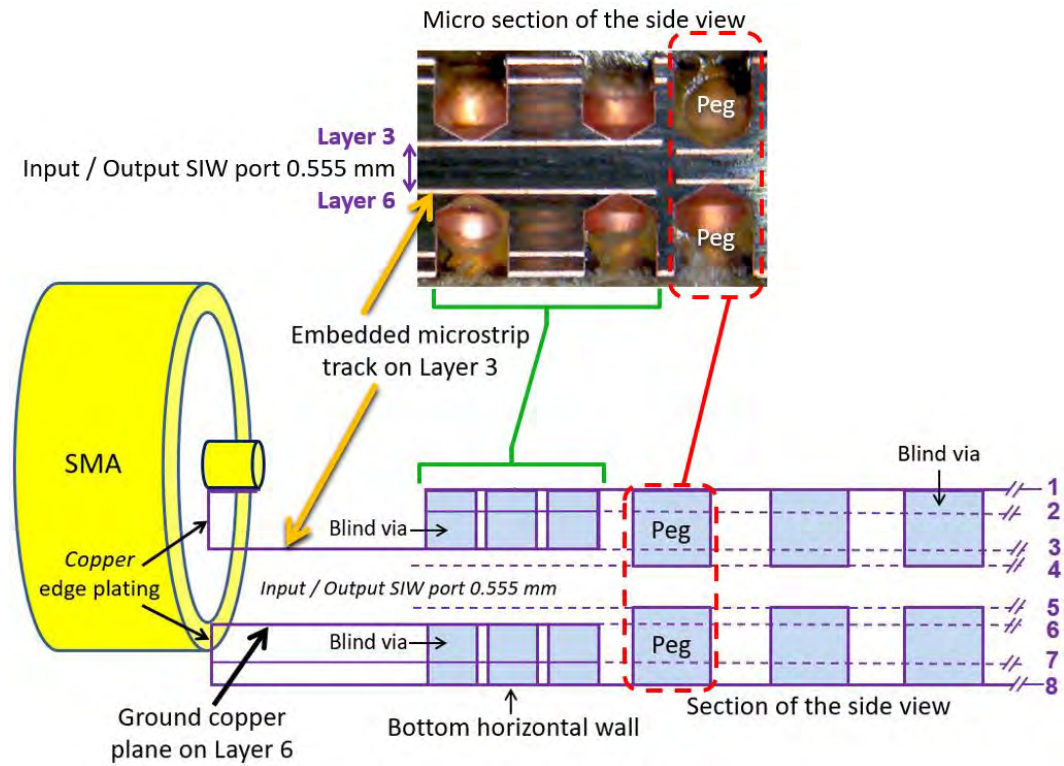


Figure 3.21: Stack-up for the multilayer PCB with a SMA edge mount connector to an UWB SIW transition.

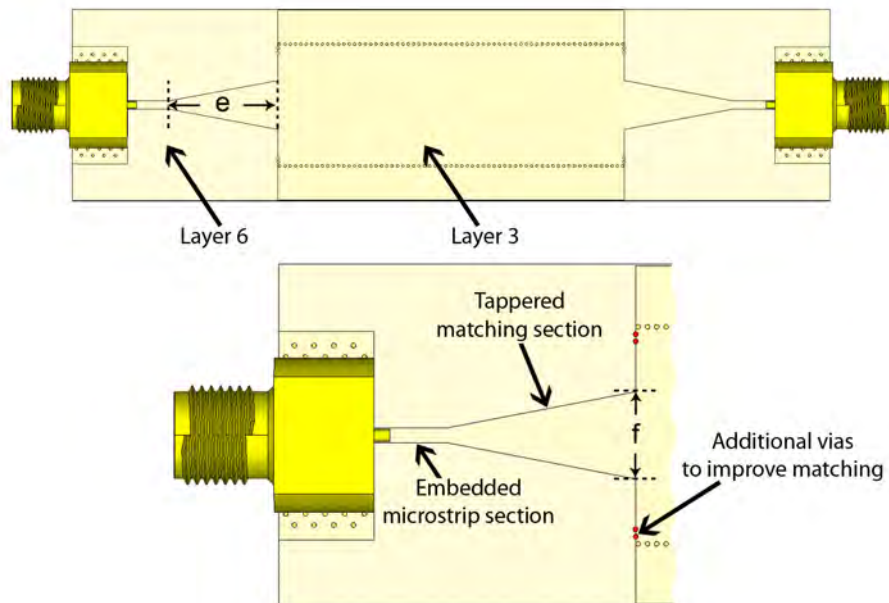


Figure 3.22: Top view of the structure, showing layer 3 and layer 6.

The embedded microstrip line is connected similarly to that of a standard microstrip-to-SIW transition. This is shown in Figure 3.22, where a top view of the structure shows the metal layers 3 and 6 together. The filter PCB consists out of *Mercurywave<sup>TM</sup>* 9350 core material, with a dielectric constant ( $\epsilon_r$ ) of 3.55. The structure is optimised in CST Microwave Studio for optimal return loss in the 8-12 GHz band.

Note also in Figure 3.22 that additional vias were used to improve the bandwidth results [70].

IPC-2141A [71] embedded microstrip formulas are used to calculate the track widths for the line segments, as seen in Figure 3.23:

$$Z_0 = \frac{60}{\sqrt{e_r \left( 1 - e^{\left( \frac{-1.55H_1}{H} \right)} \right)}} \ln \left[ \frac{5.98H}{(0.8W + T)} \right] \quad (3.4.1)$$

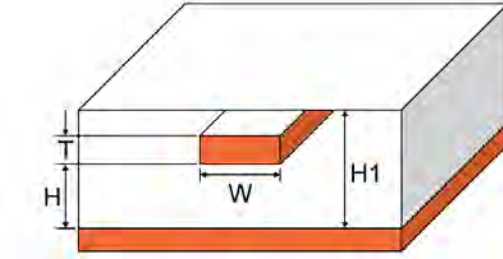


Figure 3.23: Embedded microstrip structure.

The proposed transition utilise the same width for the feeder line on both the top and inner layer. The length of the line on the top layer is very short and only required to facilitate the soldering of the inner pin of the SMA connector.

The SIW is designed from standard formulas [47] and a full set of dimensions is shown in Table 3.5.

Table 3.5: Dimensions of the transition in mm

a	b	c	d	e	f	g	h
0.93	1.206	1.5	0.5	11.9	5.38	4.67	0.555

Figure 3.24 shows a manufactured back-to-back transition with a section of SIW. The edge plating connecting the different layers, as well as the blind vias, and the top microstrip line, are clearly shown. The structure was measured using a Keysight PNA-X with coaxial calibration.

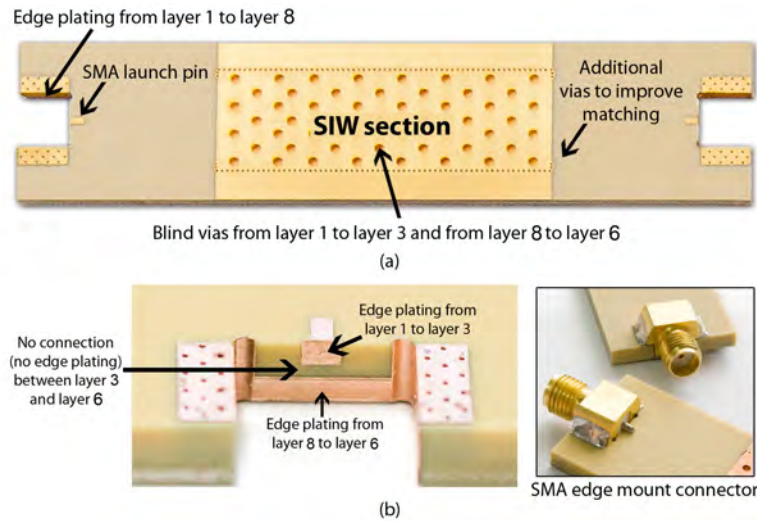


Figure 3.24: Manufactured PCB, (a) top view and (b) side view.

Figure 3.25 shows both the simulated and measured results for the back-to-back SMA-to-SIW transition. The simulated and measured results correlate closely with each other and show a measured insertion loss of between 1.0 dB at 8 GHz and 1.5 dB at 12 GHz, including the SIW line loss. A return loss of better than 15 dB is achieved across the band.

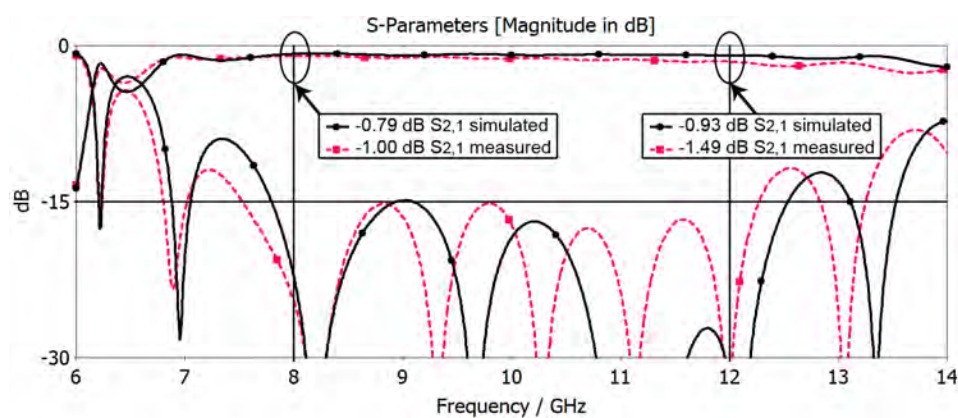


Figure 3.25: Measured and simulated S-parameters of the manufactured back-to-back SMA-to-SIW transition.



To compare the proposed transition with a standard via-based one, using the same layer and material structure, simulations of both were performed in CST Microwave Studio, with the results shown in Figure 3.26. While the return loss performance is comparable, the proposed transition (EMS) shows a simulated insertion loss exhibiting better than 0.9 dB across the 8-12 GHz band, while the normal via-based one (MS) shows a simulated insertion loss of 3.0-4.3 dB.

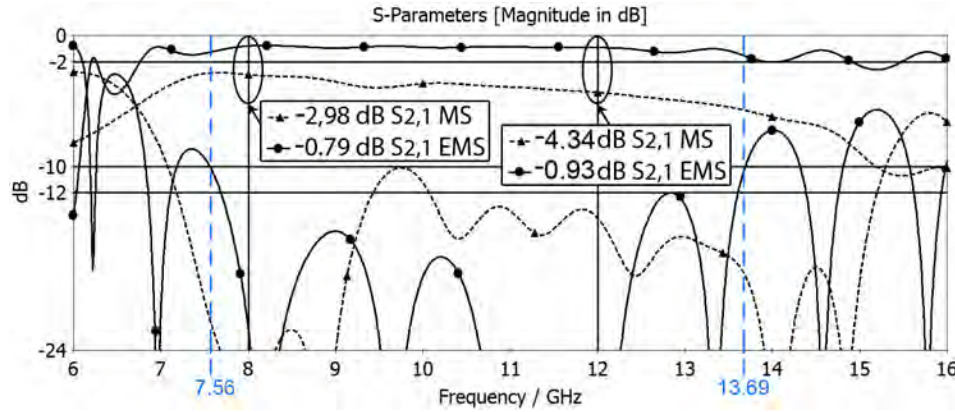


Figure 3.26: Comparison between simulated results for a back-to-back via-based transition (MS) and the proposed edge-plated transition (EMS).

### 3.4.2 SMPM to SIW transition

An SMPM connector can also be used in place of the SMA connector. In Figure 3.27, the construction can be observed, where depth controlled routing is used to remove the dielectric material from layers 1 to 3. SMPM pad is etched on layer 3, and the SMPM inner pin is connected to the embedded microstrip line. In Chapter 4 the results between SMA and SMPM will be compared.

### 3.4.3 Waveguide to SIW transition

A normal 2-port VNA measurement cannot be used to measure a multimode waveguide filter. The reason for this is that each waveguide port displays the sum of a set of different modes and not the individual modes separately. To measure the scattering parameters of multimode waveguide filters such as the Waffle-iron filter, it is proposed to launch different combinations of modes into the Input waveguide port, which is then measured at the output port. The complete implementation of such a system will be examined in Section 4.2

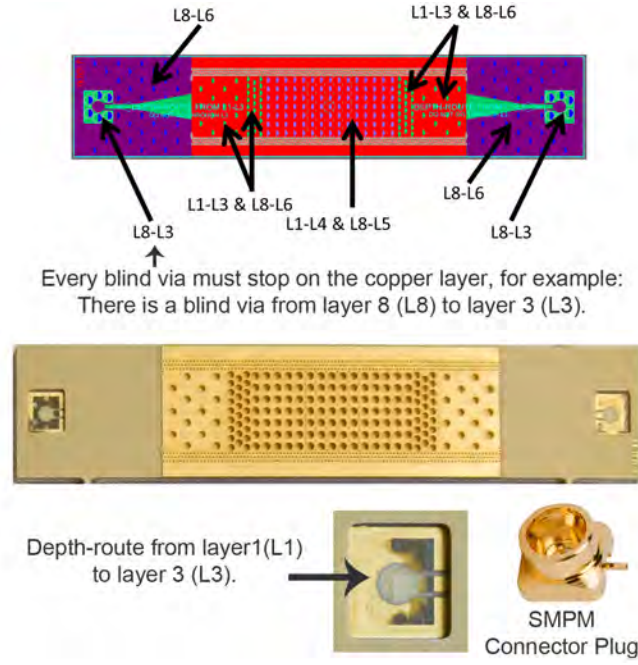


Figure 3.27: SMPM PCB.

of Chapter 4. In this subsection, only the waveguide to SIW transition will be considered. Figure 3.28 consists out of two main sections, (1) the 3 mm to 0.555 mm air waveguide transition (green area) and (2) the 0.555 mm air waveguide to SIW transition (purple area).

Section 1 - WR90 waveguide with a height of 3 mm was selected to suppress incident modes having horizontal components of electrical fields that can excite slot modes. The 3 mm opening in the air waveguide is decreased to a 0.555 mm air waveguide and the total length is 91.3 mm. The 0.555 mm is the same height as the Input and Output port for the SIW structure.

Section 2 - The 0.555 mm high WR90 (width of 22.86 mm) air waveguide is transformed to MSIW with a width of 13.125 mm. According to Mansor [72], a linear transition offers the best return loss, and the final length of the transition is 119.9 mm. A triple cascading through-hole via wall was used for the waveguide sides. As seen in Figure 3.29, a dovetail opening inside the waveguide is edge plated (purple area) to give a better defined transition as seen in Figure 2.6 in Chapter 2. Blind via stitching from layer 1 to 3, as well as layer 8 to 6, was done to eliminate any resonance from forming between the unused parallel PCB layers.

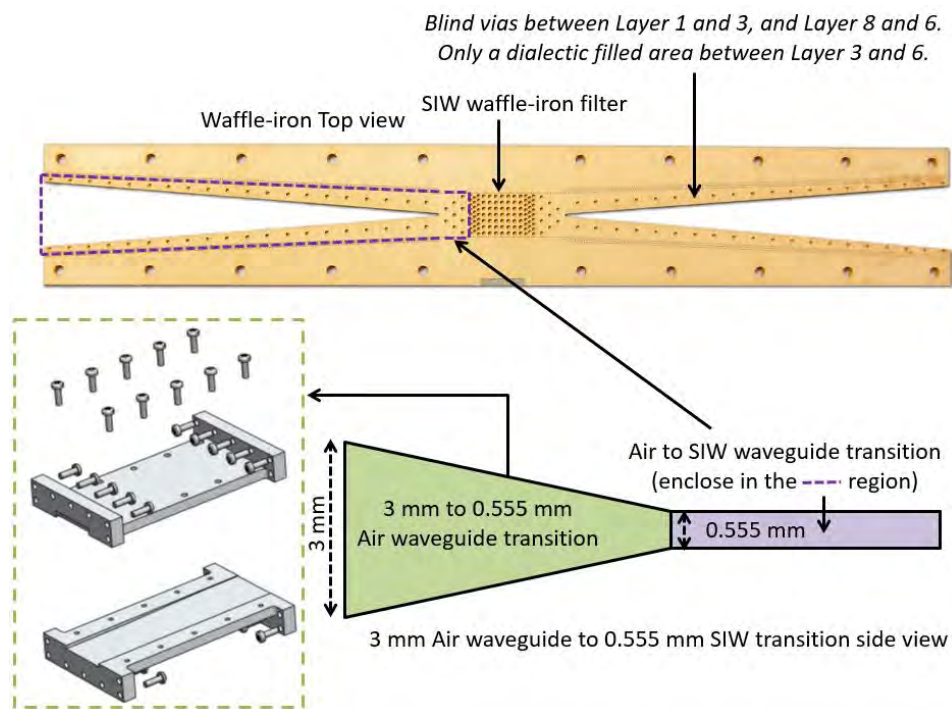


Figure 3.28: 3 mm Air waveguide to 0.555 mm SIW transition.

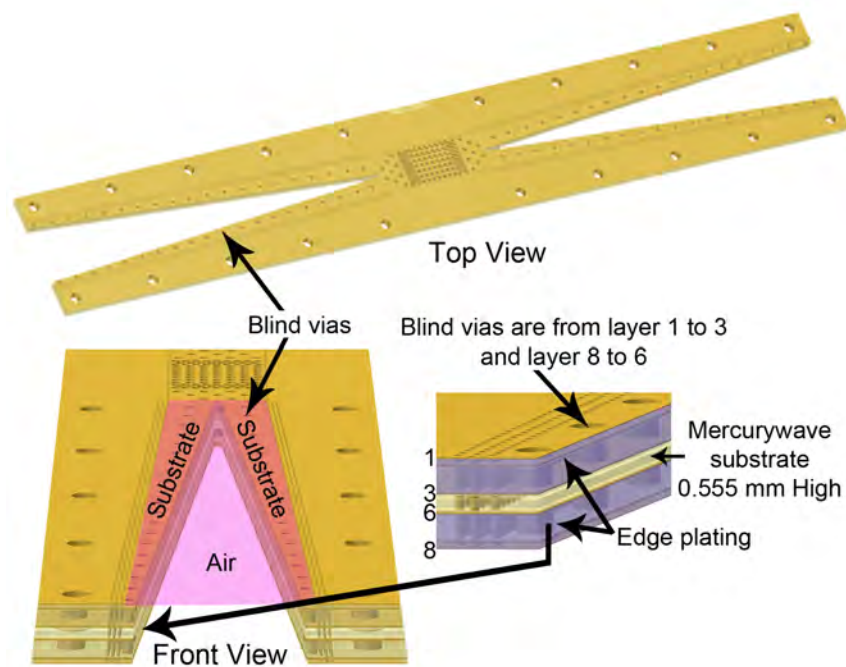


Figure 3.29: PCB with air waveguide to SIW transition.



As seen in Figure 3.30, the PCB slides into the metal waveguide structure, which has a dovetail step to ensure that a 0.555 mm waveguide opening is formed once the structure is fastened with 3.2 mm screws.

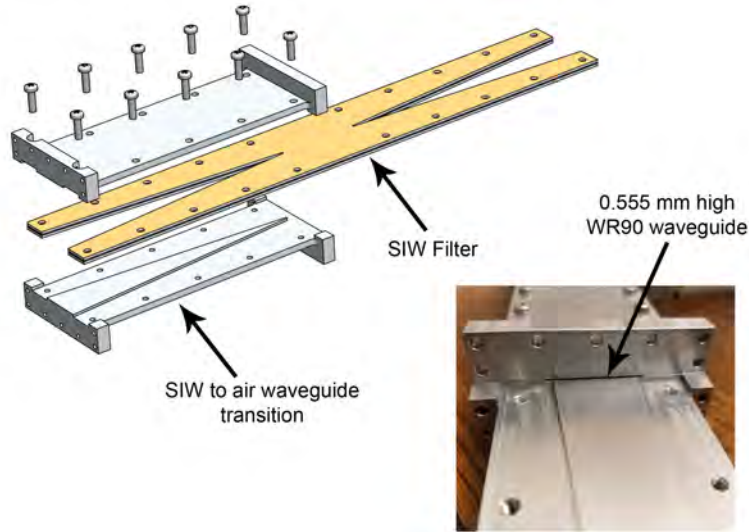


Figure 3.30: Air waveguide to SIW transition.

### 3.5 Manufacturing Issues

Two sets of PCB batches were manufactured. The first batch's final finish was done with Immersion-Gold. For the second batch, it was chosen not to have any final finish because the signal will only propagate between the inner-layer copper of the PCB.

A few observations will be made from the two batches, some observations will be looked at in this section, and some will be considered during the measurement evaluation in Chapter 4.

As previously mentioned, it is essential that the pegs are vertically aligned and the vertical gap ( $b'$ ) between the pegs must be kept constant. As seen in Figure 3.31, two round pads, on separate layers, were added to each peg. This was done to ensure that the vertical gap stays the same, and to control the depth tolerance of the blind via. For batch 1 it shows in Figure 3.31 (micro-section), and Figure 3.32 (CT-scan), that the top blind via is not aligned with the bottom blind via and has an offset of 0.15 mm. The top via was also not drilled deep enough, and the pads on each layer are also not 1.3 mm, but 1.14 mm. There are also some un-plated sections in the blind vias.

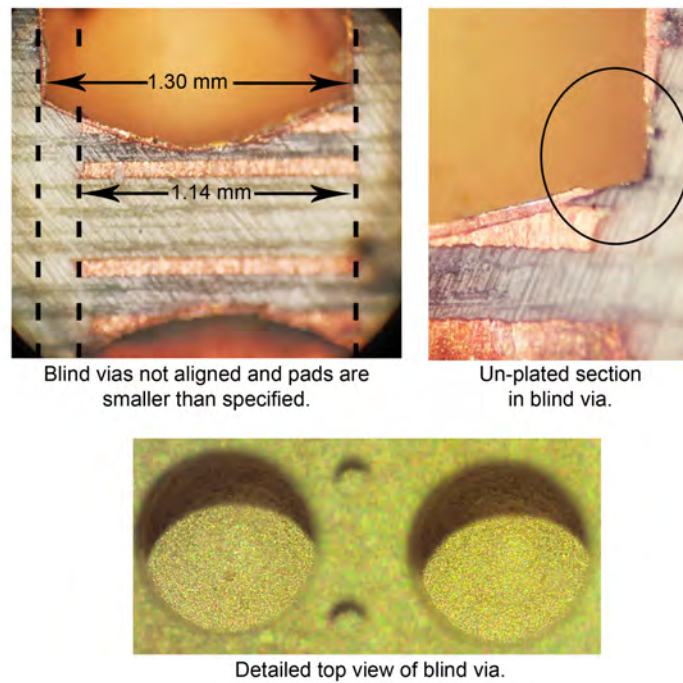


Figure 3.31: Batch 1 - Micro-section.

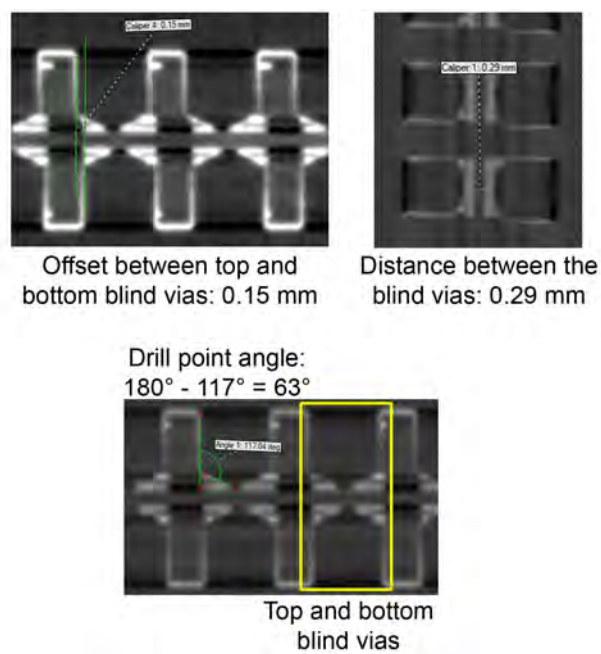


Figure 3.32: Batch 1 - CT-Scan.

For batch 2, the manufacturing process was improved. The panel was mounted on a 10 mm multi-layered FR4 PCB plate, with a tolerance of  $50\text{ }\mu\text{m}$ , as seen in Figure 3.33. What made this step challenging with the waffle-iron filter panel, is the fact that the copper thickness is only  $70\text{ }\mu\text{m}$ , so the depth controlled drilling process needs to be accurately controlled across the entire length of the panel, in this case, 360 mm. The fabricator, therefore, had to ensure planarity of the panel of less than  $50\text{ }\mu\text{m}$  over the entire 360 mm. This was accomplished by making a specialised 10 mm base plate out of FR4 material.



Figure 3.33: Depth controlled drilling.

Steel and aluminium plates were also considered, instead of the FR4 PCB plate, but the steel was too heavy for the drilling-bed and an aluminium sheet was not level enough for the required size.

In Figure 3.34, the micro-section, and Figure 3.35, the CT-scan, the alignment of the top and bottom pegs are much better with a  $0.04\text{ mm}$  difference. Each blind via is also touching both pads, and the pads also have a diameter of  $1.3\text{ mm}$ . The internal dimensions for the second batch are much better than the first batch but the external finish for batch 2 was not satisfactory. The external finish will be discussed in Chapter 4, together with the measured results.

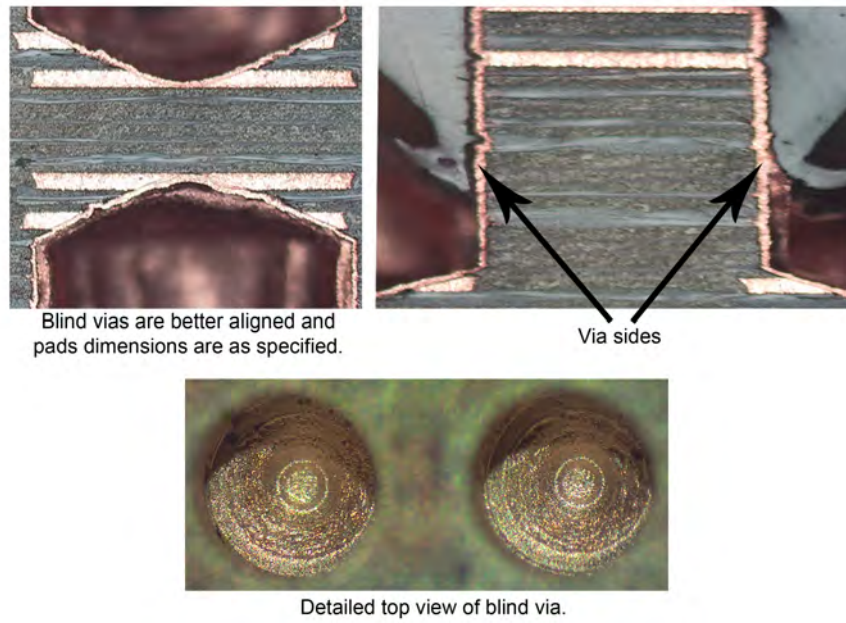


Figure 3.34: Batch 2 - Micro-section.

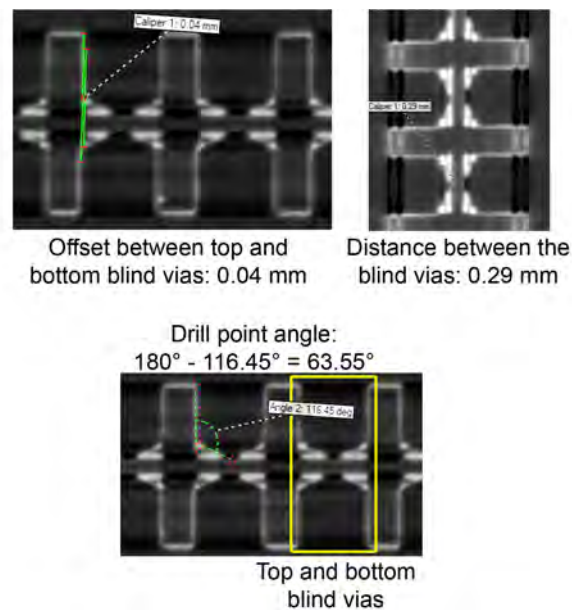


Figure 3.35: Batch 2 - CT-Scan.

The main disadvantage between a MSIW waffle-iron filter and a metal waffle-iron filter is the power handling capability. Metal waffle-iron filters are, for example, used in pulsed radar systems with peak power levels of 10 kilowatts (kW). The MSIW waffle-iron filter is designed to handle an average power of 10 Watts, but this is ideal for medium power systems.

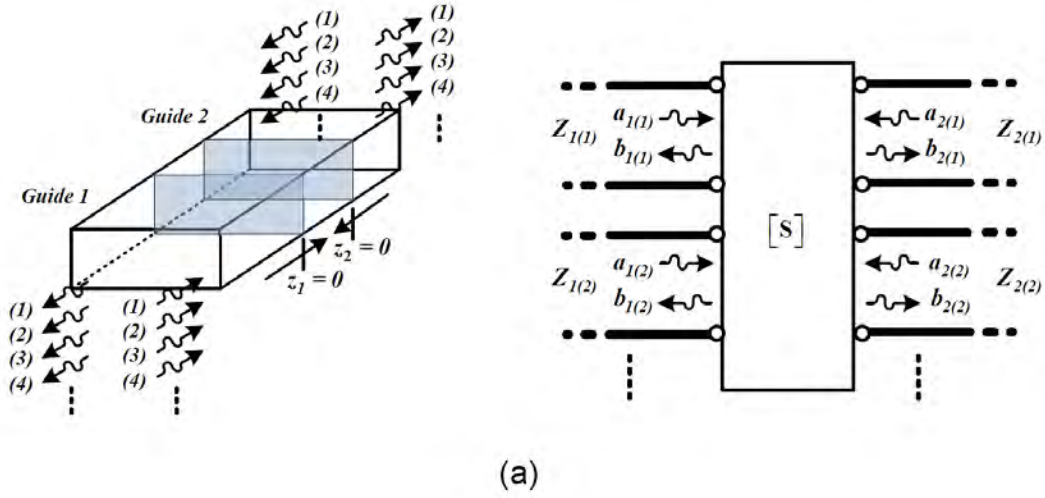
# Chapter 4

## Measurements

### 4.1 Measurement of devices supporting multiple propagating modes

Measurement of devices supporting multiple propagating modes at the ports, such as the one shown in Figure 4.1 (a), is normally difficult and time-consuming. The summation of the different modes needs to be separated into single-port measurements taken at one physical port. This is time-consuming because each mode is made up of a different electrical port, creating this complex multi-port device that can only be characterised by a generalised scattering matrix [73].

Pace et al. proposed the concept of a generalised scattering matrix for waveguide problems [74]. In their model, each physical port is made up of an infinite set of electrical ports, including both propagating and evanescent modes, and makes use of a multi-port S-parameter formula where the electrical ports are grouped in each physical port. This generalised scattering matrix creates a normalised basis by which the magnitude of the complex power carried by the wave is quantified. In Figure 4.1 (b), the matrix  $\mathbf{S}$  is called the generalized scattering matrix and is extensively used in solving waveguide problems.



$$\begin{bmatrix} b_{1(1)} \\ b_{1(2)} \\ \vdots \\ b_{2(1)} \\ b_{2(2)} \\ \vdots \end{bmatrix} = \begin{bmatrix} S_{1(1),1(1)} & S_{1(1),1(2)} & \cdots & S_{1(1),2(1)} & S_{1(1),2(2)} & \cdots \\ S_{1(2),1(1)} & S_{1(2),1(2)} & \cdots & S_{1(2),2(1)} & S_{1(2),2(2)} & \cdots \\ \vdots & \vdots & \cdots & \vdots & \vdots & \cdots \\ S_{2(1),1(1)} & S_{2(1),1(2)} & \cdots & S_{2(1),2(1)} & S_{2(1),2(2)} & \cdots \\ S_{2(2),1(1)} & S_{2(2),1(2)} & \cdots & S_{2(2),2(1)} & S_{2(2),2(2)} & \cdots \\ \vdots & \vdots & \cdots & \vdots & \vdots & \cdots \end{bmatrix} \begin{bmatrix} a_{1(1)} \\ a_{1(2)} \\ \vdots \\ a_{2(1)} \\ a_{2(2)} \\ \vdots \end{bmatrix}$$

or

$$\mathbf{b} = \mathbf{S}\mathbf{a}$$

Figure 4.1: Modes in a Waveguide (a) and its generalized S-Matrix representation (b). The vectors  $\mathbf{a}$  and  $\mathbf{b}$  contain the amplitudes of the incident and reflected modes at each port respectively [73].

In Section 1.1.3, a summary of possible solutions recorded in literature, is presented. The most accurate broadband measurement technique is presented by Sequinot et al. [44]. A multimode thru-reflection-line (TRL) algorithm used to derive the generalised scattering parameters of multimode two-port networks is proposed. They make use of multimode-to-N-line transitions in microstrip. In the theoretical development, they use notation similar to that used in the previous work of Eul and Schiek [75], which may be familiar to

engineers involved in microwave calibration techniques. This method requires the characterisation of a  $2N$  port device with the aid of a network analyser, but it is unfortunately time-consuming, which limits the practicality thereof.

To measure a multimode device, a controllable mode excitation is required at the input and output ports. In this chapter, it is proposed to replace Guide 1 and Guide 2 in Figure 4.1 with a lightly coupled single-mode co-axial probe, feeding into a multimode rectangular waveguide (as seen in Figure 4.2). This transition is described by the generalised scattering matrix in equation 4.1.1, where vector quantities are indicated by horizontal bars and matrix quantities with square brackets. This is a subset of the generalised scattering matrix of the transition, consisting of only the propagating modes which couple to the probe, and implies that the reference planes at the various ports are positioned in such a way that all non-propagating modes have died out. Note that all waveguide modes not excited by the probe, are excluded. In order to obtain a description containing all the propagating modes, various probe positions are required. Although equation 4.1.1 is only a subset of the full matrix, the characterisation of all the unknowns in this equation is still a formidable task, requiring a large number of calibration measurements.

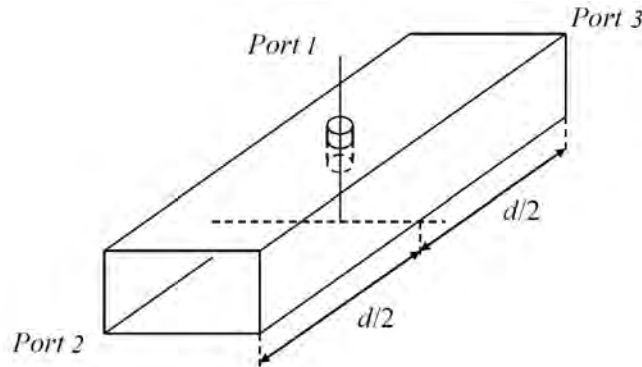


Figure 4.2: The three-physical-port probe section.

$$\begin{bmatrix} b_1 \\ \vec{b}_2 \\ \vec{b}_3 \end{bmatrix} = \begin{bmatrix} S_{11} & \vec{S}_{12} & \vec{S}_{13} \\ \vec{S}_{21} & [\vec{S}_{22}] & [\vec{S}_{23}] \\ \vec{S}_{31} & [\vec{S}_{32}] & [\vec{S}_{33}] \end{bmatrix} \begin{bmatrix} a_1 \\ \vec{a}_2 \\ \vec{a}_3 \end{bmatrix} \quad (4.1.1)$$

All the research until now focused on the characterisation of all the unknowns and calibrating devices that support multiple propagating modes. This



dissertation proposes two methods by which only the multimode waveguide filter is measured. Both methods, using the three-port device, will first use a Thru to measure the test set-up and show that each port exhibits multiple propagating modes. The Thru will then be replaced by a filter, and the same measurements will be taken again. The  $S_{21}$  results of the Thru, as well as the measurements of the filter, will then be plotted together. The main reason for this approach is that the interest of this measurement lies in the stopband of the filter. If enough combinations of modes can be excited, and all of these combinations show a significant attenuation, the results show that the stopband working of the filter can be validated up to 50 dB, without requiring a full calibration of the transition. Note that the fundamental mode will always be excited to a certain extent with this approach, resulting in a superposition with the propagating higher order modes. With the passband measurements, a normal coaxial to waveguide transition can be used, as only the  $TE_{10}$  mode propagates in that frequency band.

In the first method, a signal is lightly coupled through a 2.4 mm connector into an air-filled WR90 waveguide, with a height of 3 mm, that generates different mode combinations at the port. The modes propagate through an air-to-dielectric waveguide transition, into the MSIW waffle-iron filter. The unfiltered multimode signals are received at the output port of the filter. These modes travel through a dielectric-to-air waveguide transition and are finally coupled to the 2.4 mm connector at the furthest end. A condition, however, might occur where a mixture of modes is reflected by the output port. For this reason, the second method is proposed.

In the second method, the 2.4 mm connector set-up, at the output port, is replaced by a horn antenna, offering a very low reflection coefficient for all propagating modes at its feed plane. The 2.4 mm connector configuration on the input port of the filter stays the same. This method ensures that no mode is reflected at the output port and all the modes radiate out through the horn antenna.

If the results in both test methods yield similar results, then it is safe to assume that the filter works as expected.

#### 4.1.1 First measuring method: 2.4 mm connector set-up

This first method will be done by using a mechanical WR90 waveguide construction with two manual shifters attached to it. As seen in Figure 4.3, one shifter is attached at the back end of the waveguide ( $y$ -direction), to move the sliding back-short plate by turning the shifter's knob. The second shifter is on the side of the waveguide ( $x$ -direction), to move the 2.4 mm connector across



the width of the waveguide.

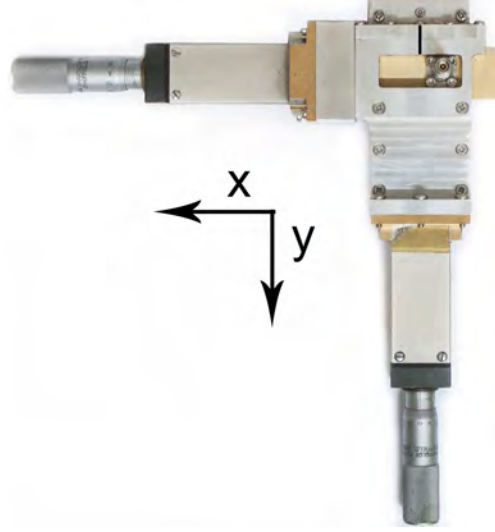


Figure 4.3: 3 mm High WR90 waveguide with a vertical and horizontal shifter.

The mechanical construction is attached to each side of the filter, to measure the propagating modes at each of the two ports.

As seen in Figure 4.4 (a), the 2.4 mm connector can move horizontally in width by turning the adjustment screw on the left-hand side. The 2.4 mm connector has a frequency range of DC to 50 GHz. The centre pin is very thin and acts like a monopole. A piece of shim-stock is soldered onto the centre pin of the 2.4 mm connector. This alters the coupling between the waveguide structure and the centre pin, resulting in an improved bandwidth response, as well as the insertion loss over the measured frequency band. This method differs from the previous proposed methods [38], [39], [40], [41], [42], [44], because the connector is adjusted slightly by turning the shifter, as seen in Figure 4.4 (b), and different modes can be generated. The adjustable sliding back short is created by inserting a machined sliding plug inside the guide (the green section in Figure 4.5). The other end is connected to the shifter. A great advantage of this method is the ease with which measurements can be made for the various choices of lengths, requiring only the manipulation of the sliding shorts by turning the shifter. Enough measurements must be made to determine all the elements of the scattering matrix relating to propagating modes.

Using a matrix network as seen in Figure 4.5, multiple modes are generated. The manual shifters have a tolerance of  $10\text{ }\mu\text{m}$ , which leads to accurate matrix positions. Also, the filter is passive and symmetrical, this means that

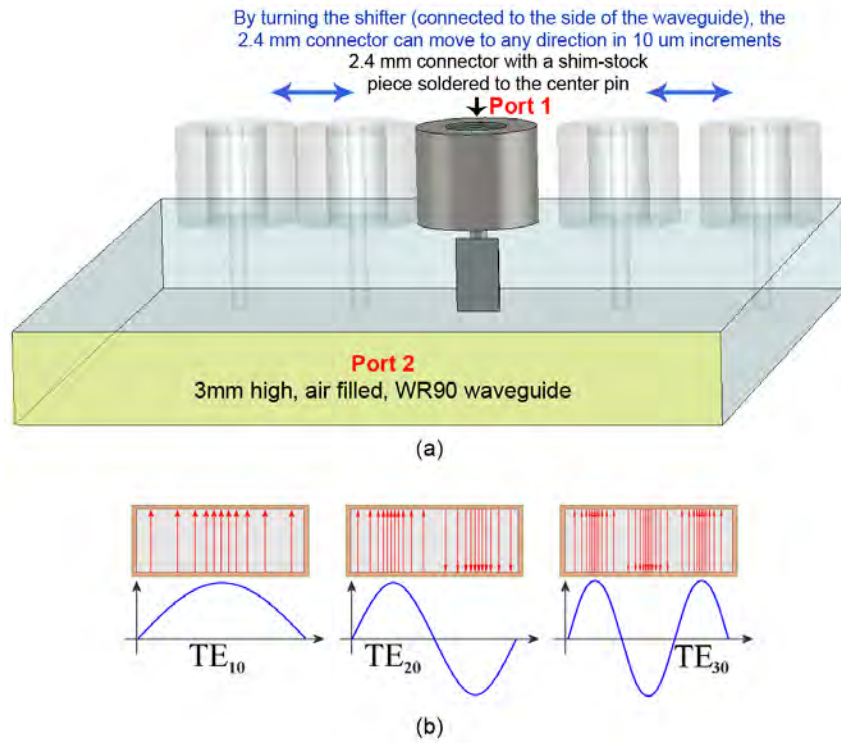


Figure 4.4: Adjusting the 2.4 mm connector.

$S_{21}$  and  $S_{12}$  will be the same. Figure 4.6 shows the frequencies where the different  $TE_{m0}$  modes start to propagate.

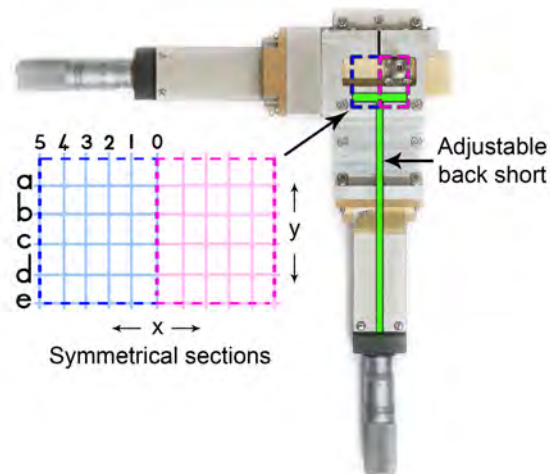


Figure 4.5: The 2.4 mm connector test set-up.

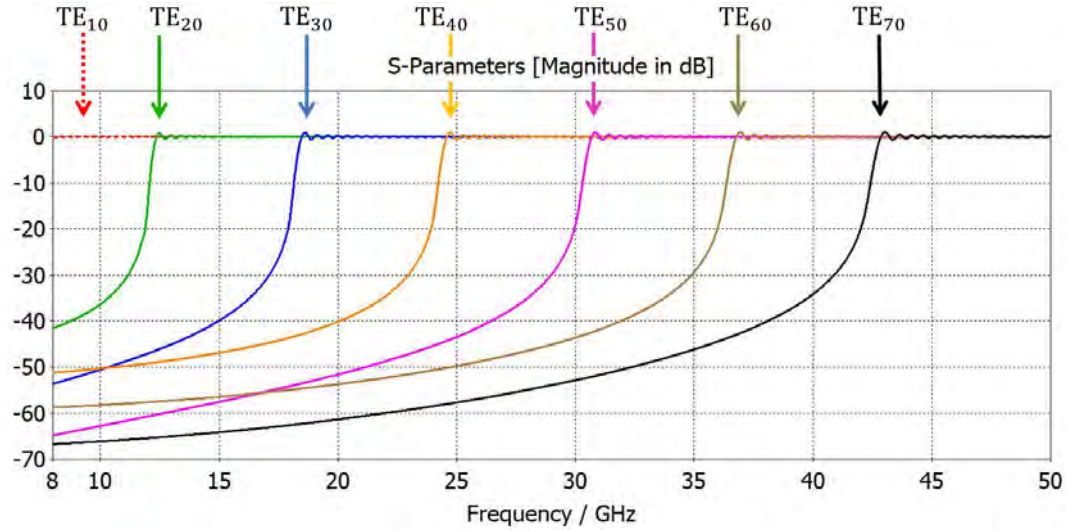


Figure 4.6: Simulated results for the  $TE_{m0}$  modes.

### Matrix set-up

Two matrices are proposed:

1. In Figure 4.5, the first matrix test set-up is as follow:
  - a) Move Port 2 to position  $a0$ .
  - b) Move Port 1 also to position  $a0$  and save the results as  $a0a0$ . The capture method of the results must stay consistent with the first part being Port 1 and the second part being Port 2 of the file name.
  - c) Keep Port 2 at position  $a0$  and move Port 1 to position  $a1$  and capture the results. Continue until Port 1 reach  $a5$ , then move Port 1 to  $b0$ . Continue until the last position  $e5$ .
  - d) Move Port 2 to  $a1$  and Port 1 to  $a1$ . Do not move Port 1 to  $a0$  and repeat step 2 and step 3. The reason to start Port 1 at  $a1$  is that the test set-up is not only symmetrical in  $x$ -direction (width of the waveguide) but the whole filter test set-up is symmetrical between Port 1 and Port 2 (in the  $y$ -direction). This means that  $S_{11}$  equals  $S_{22}$  and  $S_{21}$  equals  $S_{12}$ , for one set of measurements using the 2-port VNA. This reduces the number of measurements from 625 to 325, as seen in Table 4.1. This shows that  $b0b1$  (in red) does not need to be measured because  $b1b0$  (in blue) is already measured. The matrix does not have to be 5:5 and can be reduced to another relation, for example, a 4:4 and the number of measurements will reduce to 136. The 5:5 matrix was selected to prove the validity of the method.

- e) Each horizontal ( $x$ -direction) step is 2.236 mm. This ensures that the 2.0 mm wide shim-stock does not touch the waveguide wall. Each vertical ( $y$ -direction) step is 4 mm to cover a 20 mm length. During each vertical or horizontal shift, the VNA display is monitored to ensure that no modes go undetected.

Port 2

	a0	a1	a2	a3	a4	a5	b0	b1	b2	b3	b4	b5	c0	c1	c2	c3	c4	c5	d0	d1	d2	d3	d4	d5	e0	e1	e2	e3	e4	e5
a0	X																													
a1	X	X																												
a2	X	X	X																											
a3	X	X	X	X																										
a4	X	X	X	X	X																									
a5	X	X	X	X	X	X																								
b0	X	X	X	X	X	X	X	X																						
b1	X	X	X	X	X	X	X	X																						
b2	X	X	X	X	X	X	X	X	X	X																				
b3	X	X	X	X	X	X	X	X	X	X	X																			
b4	X	X	X	X	X	X	X	X	X	X	X	X																		
b5	X	X	X	X	X	X	X	X	X	X	X	X	X																	
c0	X	X	X	X	X	X	X	X	X	X	X	X	X	X																
c1	X	X	X	X	X	X	X	X	X	X	X	X	X	X	X															
c2	X	X	X	X	X	X	X	X	X	X	X	X	X	X	X	X														
c3	X	X	X	X	X	X	X	X	X	X	X	X	X	X	X	X	X													
c4	X	X	X	X	X	X	X	X	X	X	X	X	X	X	X	X	X	X												
c5	X	X	X	X	X	X	X	X	X	X	X	X	X	X	X	X	X	X	X											
d0	X	X	X	X	X	X	X	X	X	X	X	X	X	X	X	X	X	X	X	X	X									
d1	X	X	X	X	X	X	X	X	X	X	X	X	X	X	X	X	X	X	X	X	X	X	X							
d2	X	X	X	X	X	X	X	X	X	X	X	X	X	X	X	X	X	X	X	X	X	X	X	X						
d3	X	X	X	X	X	X	X	X	X	X	X	X	X	X	X	X	X	X	X	X	X	X	X	X	X					
d4	X	X	X	X	X	X	X	X	X	X	X	X	X	X	X	X	X	X	X	X	X	X	X	X	X	X				
d5	X	X	X	X	X	X	X	X	X	X	X	X	X	X	X	X	X	X	X	X	X	X	X	X	X	X	X			
e0	X	X	X	X	X	X	X	X	X	X	X	X	X	X	X	X	X	X	X	X	X	X	X	X	X	X	X	X		
e1	X	X	X	X	X	X	X	X	X	X	X	X	X	X	X	X	X	X	X	X	X	X	X	X	X	X	X	X		
e2	X	X	X	X	X	X	X	X	X	X	X	X	X	X	X	X	X	X	X	X	X	X	X	X	X	X	X	X	X	
e3	X	X	X	X	X	X	X	X	X	X	X	X	X	X	X	X	X	X	X	X	X	X	X	X	X	X	X	X	X	
e4	X	X	X	X	X	X	X	X	X	X	X	X	X	X	X	X	X	X	X	X	X	X	X	X	X	X	X	X	X	X
e5	X	X	X	X	X	X	X	X	X	X	X	X	X	X	X	X	X	X	X	X	X	X	X	X	X	X	X	X	X	X

Port 1

Table 4.1: Matrix for set-up 1.

- In the second matrix, specific frequencies (as seen in Table 4.2) were chosen to excite the  $TE_{10}$ ,  $TE_{20}$ ,  $TE_{30}$ ,  $TE_{40}$ ,  $TE_{50}$ ,  $TE_{60}$  and  $TE_{70}$  modes. From this, the distance from the centre of the waveguide ( $x$  direction), where the  $\vec{E}$ -field is the strongest for each selected mode, is calculated. Also,  $\lambda/4$  is calculated for every selected frequency. The measurements were reduced to 28, as seen in Table 4.2. The symmetry around the E-plane excludes the possibility of propagating even modes, but Quasi- $TM_{m0}$  modes, for even values of  $m$ , may also be excited due to misaligned pegs that appear asymmetrical with respect to the  $H$ -plane.

		Port 2									
Port 1		TE <sub>m0</sub>	GHz	$\lambda/4$ (mm)	X1	X2	X3	X4	X5	X6	X7
	X1	TE <sub>10</sub>	10	7.500	X						
	X2	TE <sub>20</sub>	20	3.750	X	X					
	X3	TE <sub>30</sub>	24	3.125	X	X	X				
	X4	TE <sub>40</sub>	30	2.500	X	X	X	X			
	X5	TE <sub>50</sub>	37	2.027	X	X	X	X	X		
	X6	TE <sub>60</sub>	45	$3 \times \lambda/4 = 5.000$	X	X	X	X	X	X	
	X7	TE <sub>70</sub>	48	$3 \times \lambda/4 = 4.688$	X	X	X	X	X	X	X

Table 4.2: Matrix for set-up 2.

### 4.1.2 Second measuring method: antenna set-up

As seen in Figure 4.7, the 2.4 mm connector's position can be adjusted to transmit different combinations of modes. Another horn antenna receives the radiation from the transmitted horn antenna, and the results are measured on the VNA from 26.5 GHz to 50 GHz. A distance of 45 cm between the two horn antennas are kept constant; and larger than  $4\lambda$  for the lowest frequency to ensure that the far-field is measured. In Figure 4.8 the receiving horn antenna is moved in a vertical (y) and horizontal (x) grid in 5 cm intervals, to ensure the entire far-field pattern is measured. The Thru calibration PCB is first measured to establish a baseline.

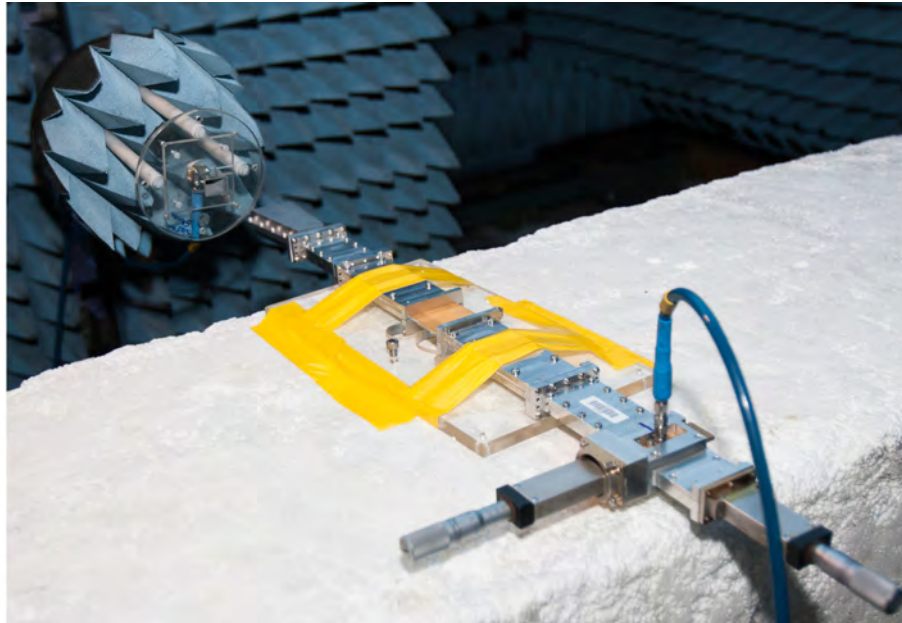


Figure 4.7: Antenna test set-up.



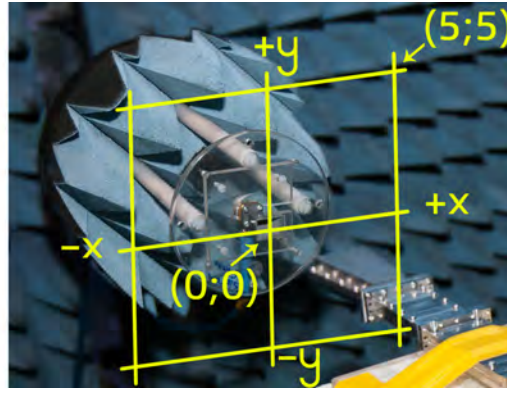


Figure 4.8: Antenna measurement grid

## 4.2 Implementation of measurement system

### 4.2.1 2.4 mm Connector set-up

The three-section mechanical structure for measuring multimode filters is shown in Figure 4.9.

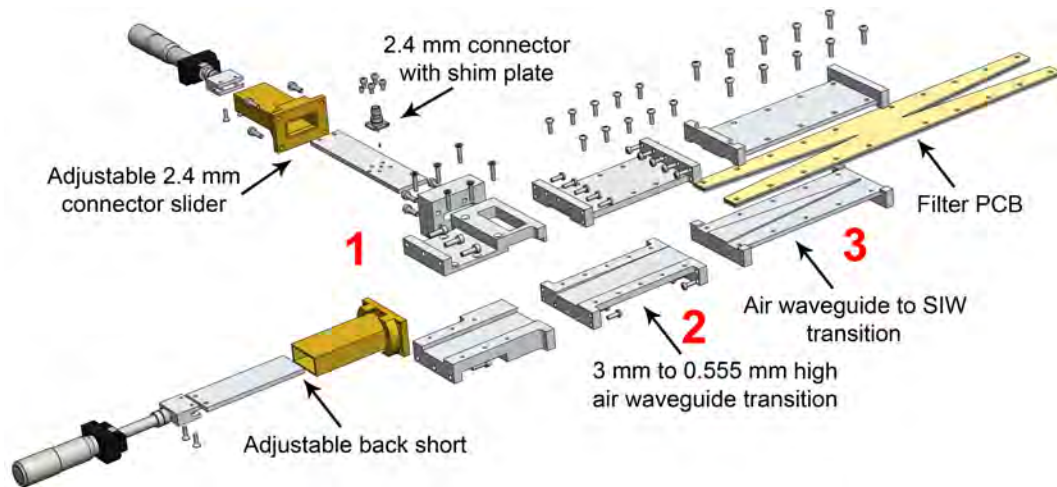


Figure 4.9: 2.4 mm Connector to SIW transition.

Section 1 consists of a WR90 waveguide with the two manual shifters. A sliding plate is connected to the horizontal shifter, with a 2.4 mm connector mounted on it as shown in Figure 4.10. A small piece of shim-stock (2.0 mm x 2.7 mm) is soldered on the 2.4 mm connector center pin, as seen in Figure 4.11, to reduce the insertion loss.

Section 2 consists of a 3 mm WR90 waveguide that is decreased to 0.555 mm, and in Section 3, a 0.555 mm WR90 waveguide is transitioned to SIW. These two sections are discussed in more detail in Chapter 3.

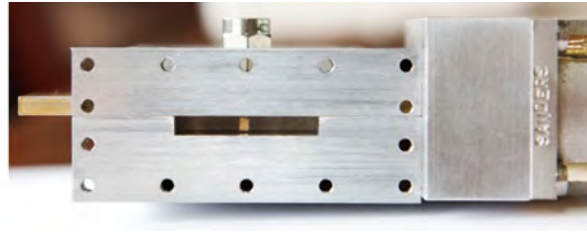


Figure 4.10: 2.4 mm Connector inserted in the waveguide.



Figure 4.11: 2.4 mm Connector with a small shim-stock piece soldered to the center pin.

The complete back-to-back 2.4 mm connector to SIW transition is shown in Figure 4.12, with the dimensions in mm.

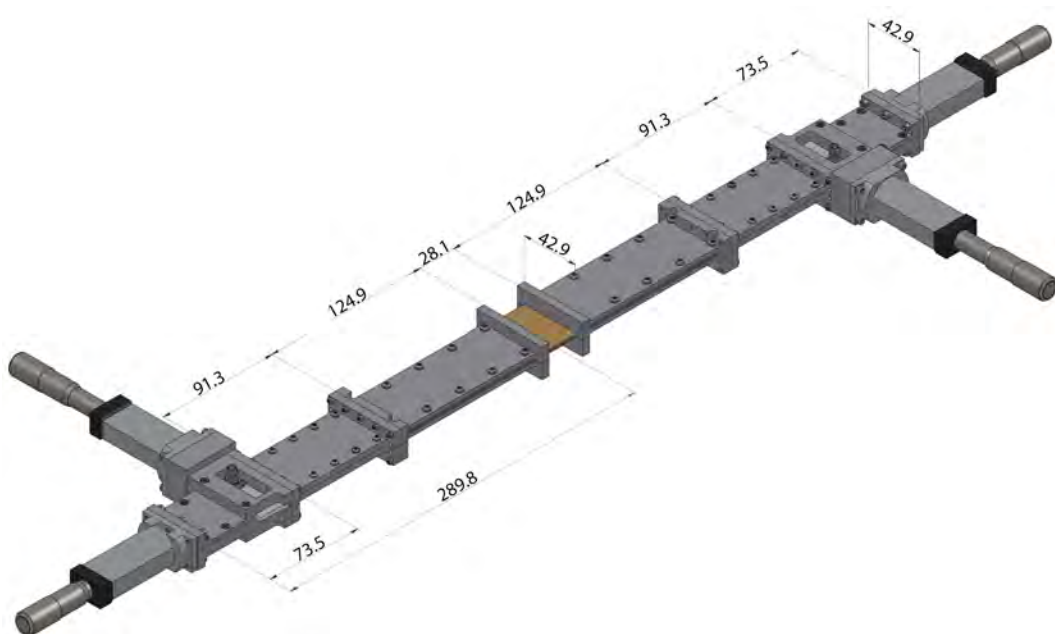


Figure 4.12: 2.4 mm Connector to SIW back-to-back transition.

### 4.2.2 Antenna set-up

Figure 4.13 shows the antenna section connected to the filter and Figure 4.14 shows the filter inside the complete horn antenna to 2.4 mm connector transition. In Figure 4.15, the antenna dimensions start from a WR90 waveguide of 3 mm opening and flaring out to a height of 20.50 mm, and a width of 40.36 mm. The total length is 100.47 mm.

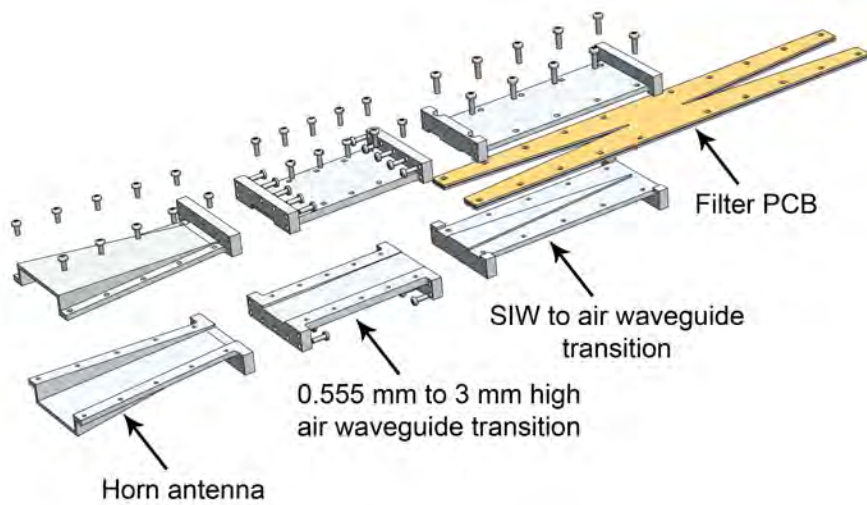


Figure 4.13: Horn antenna to SIW transition.



Figure 4.14: Completed horn antenna to 2.4 mm connector transition.



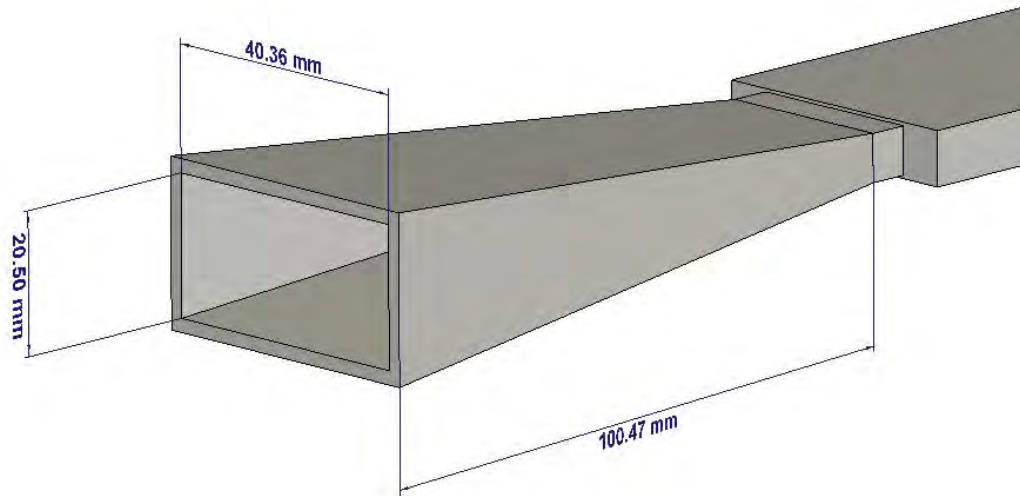


Figure 4.15: Dimensions of the horn antenna.

### 4.2.3 The Thru-standard

Before testing the filter, the test set-up must first be calibrated. Figure 4.16 shows the different calibration pieces used for the multimode test set-up. Starting from the left side, are the three pieces for the Thru set-up. To save cost a 0.555 mm double layer Thru PCB was manufactured and two aluminium plates are placed on the top and bottom of the Thru PCB to make up the total thickness of 2.857 mm. The Thru PCB consists of the same *Mercurywave<sup>TM</sup>* 9350 core material, as the waffle-iron filters, with a top and bottom copper layers. Three rows of vias on each side were to create the air-to-dielectric waveguide transition. On the left side of Figure 4.16 is Filter B (2.857 mm thick, 8 layer PCB).

Figure 4.17 (a) shows how the Thru plate is laying on the CAL bottom plate, which lays on the bottom air waveguide to SIW transition piece. Photo (b) shows how the top CAL plate lays on the Thru PCB. The last part that must be fitted and fasten with 3 mm screws is the top air waveguide to SIW aluminium transition piece.

## 4.3 Measurements of prototypes

In this section, the measured results for filter A and filter B will be shown. During the manufacturing phase, two panels are manufactured. The first panel's

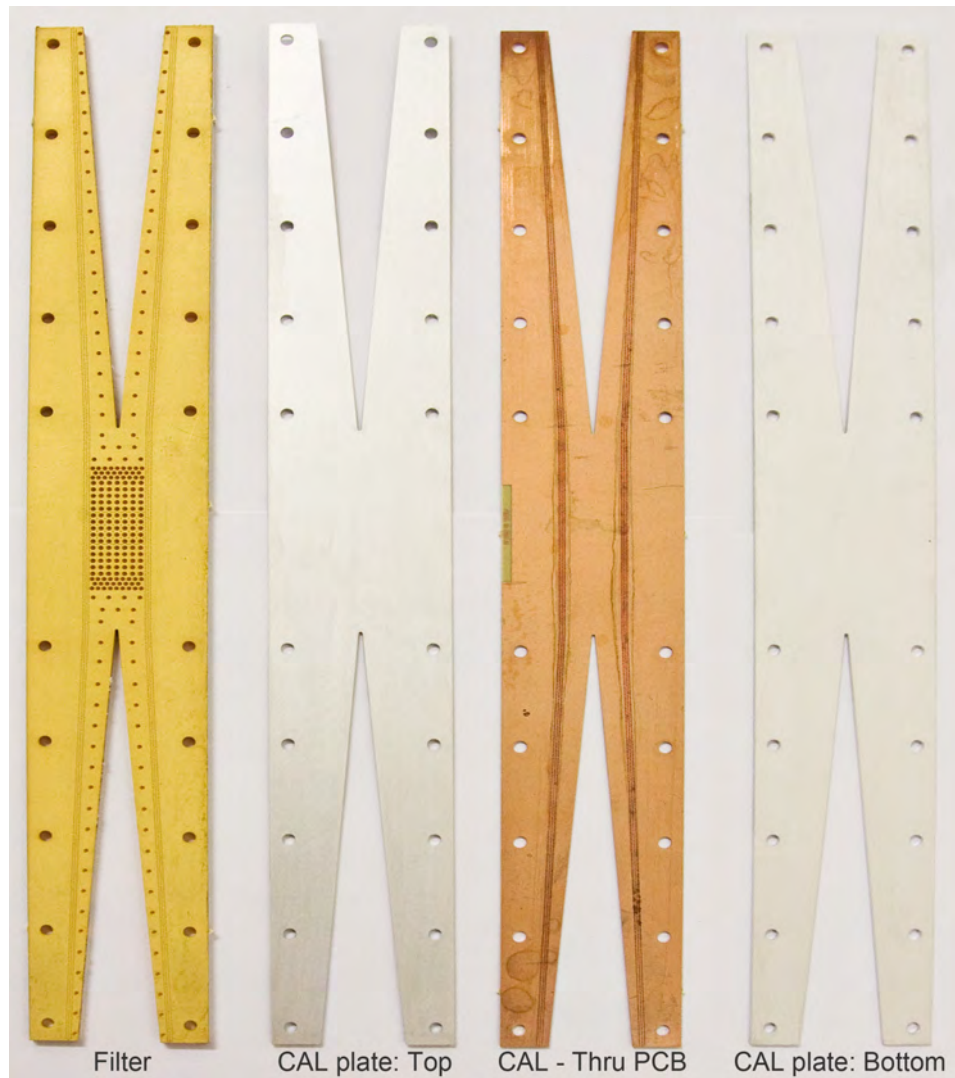


Figure 4.16: PCB test set-up.

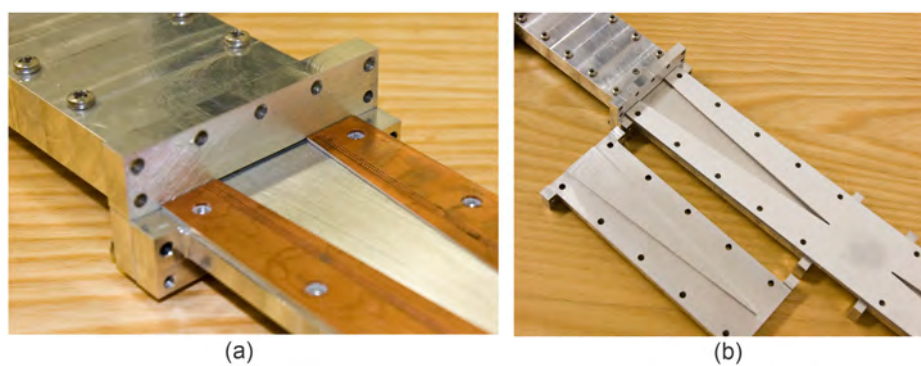


Figure 4.17: Calibration mechanical structure.

micro-section show that there is a misalignment between the bottom and top pegs. The manufacturing process is altered, and a second panel is manufactured but some inconsistencies occur during the drilling process. Each panel consists of different versions of filters A and B. The following tests were conducted:

1. Passband response measurement,
2. Multimode measurements in the stopband and
3. Power handling.

### 4.3.1 Measurement 1 - Passband response

SMA to SMA PCB filter versions were designed for both filter A and B to measure the passband response. Figure 4.18 shows the comparison between the simulated ideal lossless filter A (no SIW vias and with ideal waveguide ports); the simulated lossy MSIW filter A with SMA connectors; and the measured MSIW filter A with SMA connectors (batch 2). In Section 3.4.1, the measured insertion loss for the manufactured back-to-back SMA-to-SIW transition showed between 1.0 dB at 8 GHz and 1.5 dB at 12 GHz, this includes the SIW line loss. Also, a return loss of better than 15 dB is achieved across the band. Taking this into account, the measured passband response will have a maximum insertion loss of  $\sim 0.6$  dB over the band. The ideal filter simulation is between 4 and 5 times better than the measured filter, but this is due to no SMA connectors on each side of the filter.

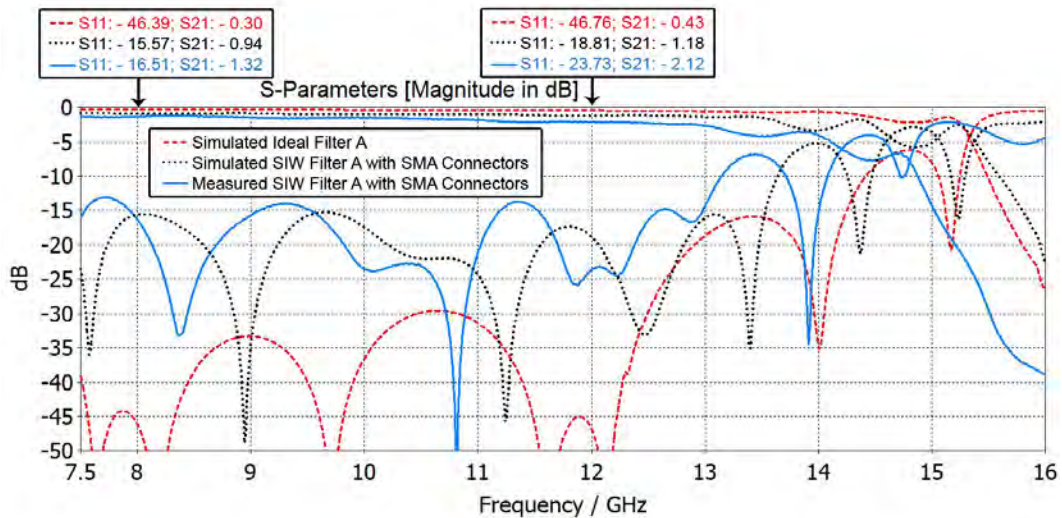


Figure 4.18: Comparison between simulated and measured results: filter A (batch 2).

Figure 4.19 shows the comparison between the simulated ideal lossless filter B (no SIW vias and waveguide ports); the measured MSIW Thru CAL PCB with SMA connectors; and the measured MSIW filter B with SMA connectors (batch 2). The insertion loss is more in filter B, but it is understandable due to the extra peg (waffle) sections in the filter.

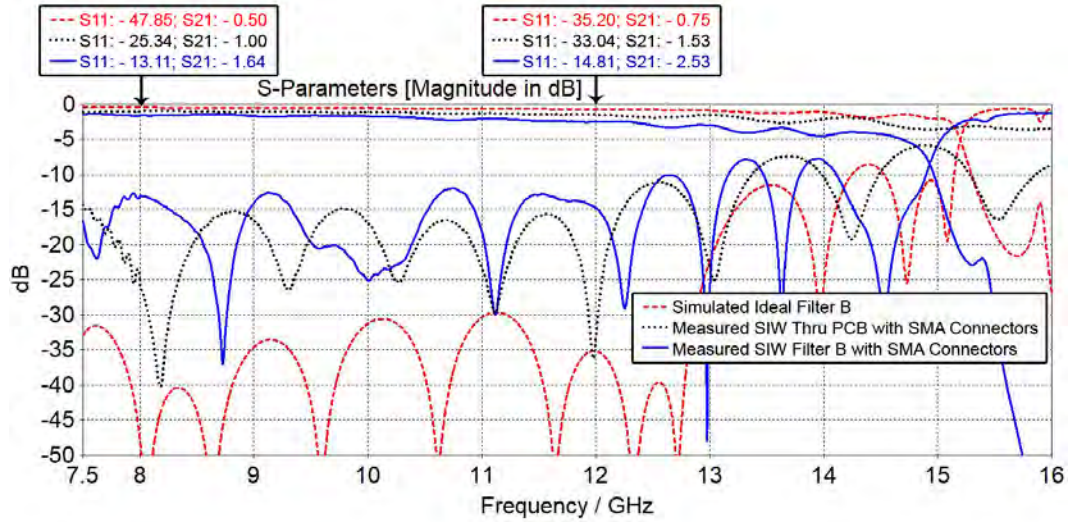


Figure 4.19: Comparison between simulated and measured results: filter B (batch 2).

The first batch has a surface finish of Immersion-Gold as seen in Figures 4.20 and 4.21. Edge mount SMA connectors are connected to each port.

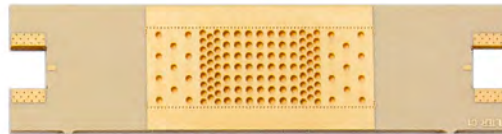


Figure 4.20: Filter A: SMA-EMS-SIW-EMS-SMA classical MSIW Waffle-iron filter.



Figure 4.21: Filter B: SMA-EMS-SIW-EMS-SMA extended MSIW Waffle-iron filter.



For the second batch, it was chosen not to have any surface finish. Figure 4.22 below shows the edge mount SMA connectors connected to the ports.

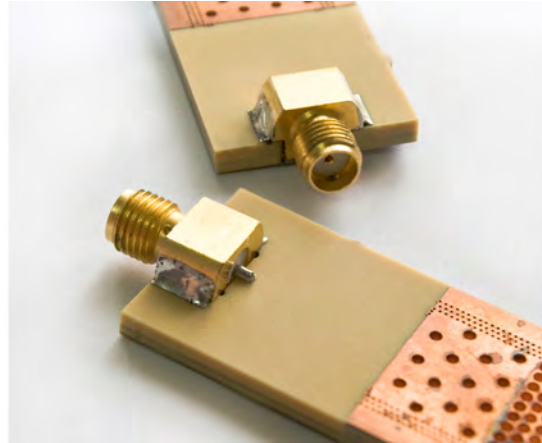


Figure 4.22: SMA connectors soldered on batch 2.

Figure 4.23 shows the response between batch 1 and batch 2 for filter A. The manufacturing process for batch 2 was much better and precise and this can be seen from the reflection coefficient that has improved from -10 dB to -14 dB. Additionally, the insertion loss improved by at least 0.5 dB and range between 1.8 dB to 2.1 dB. Lastly, the insertion loss of the Thru back-to-back SMA-to-SIW transition must be taken into account.

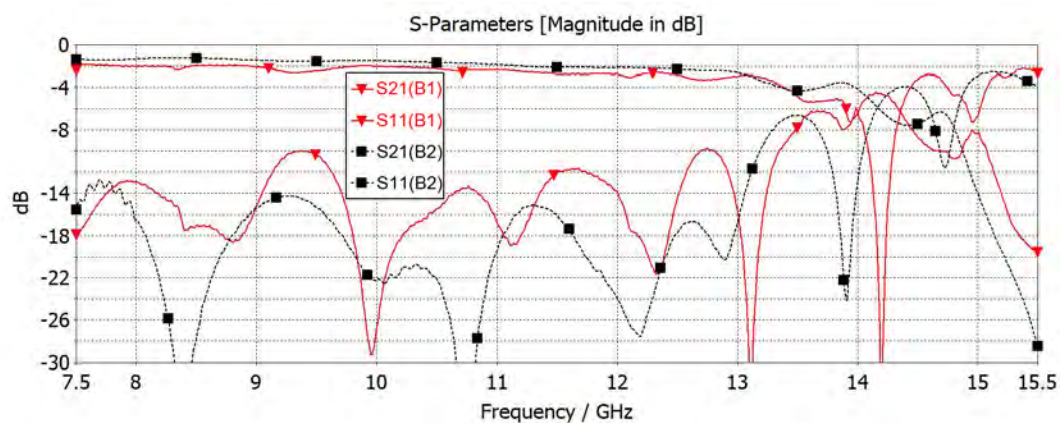


Figure 4.23: Filter A: Compare batch 1 and 2.

Figure 4.24 shows the response between batch 1 and batch 2 for filter B. Batch 2 has a higher insertion loss of 1.91 dB at 8 GHz and 3.04 dB at 12 GHz.

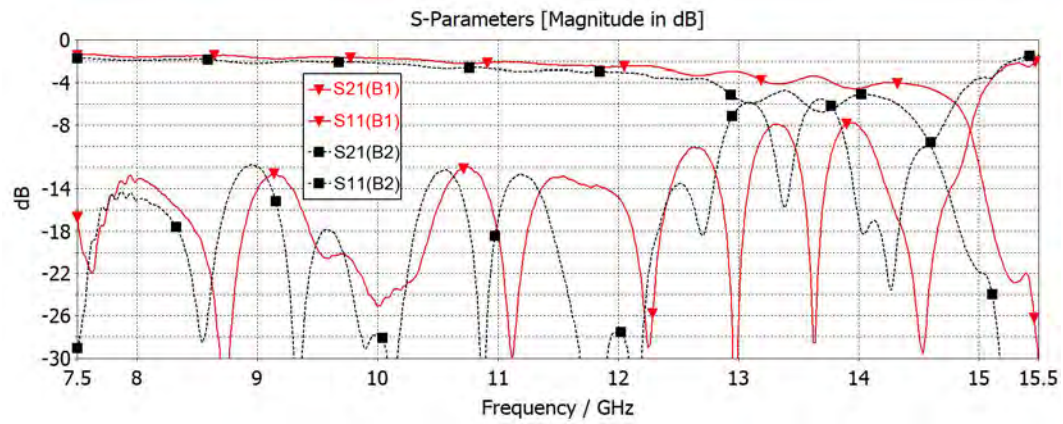


Figure 4.24: Filter B: Compare batch 1 and 2.

In Figure 4.25 two enclosures are fitted because the SMA to embedded microstrip transition acts like an antenna in the stopband for higher frequency modes. As seen in Figure 4.26, the stopband performance has improved from 42 dB return loss to 68 dB.

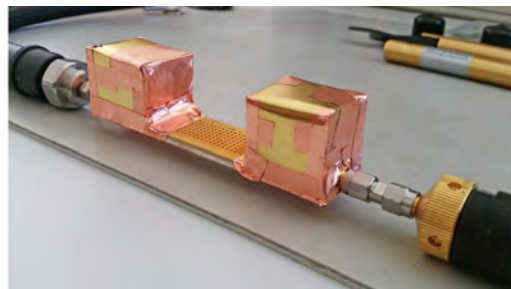


Figure 4.25: SMA transition enclosures.

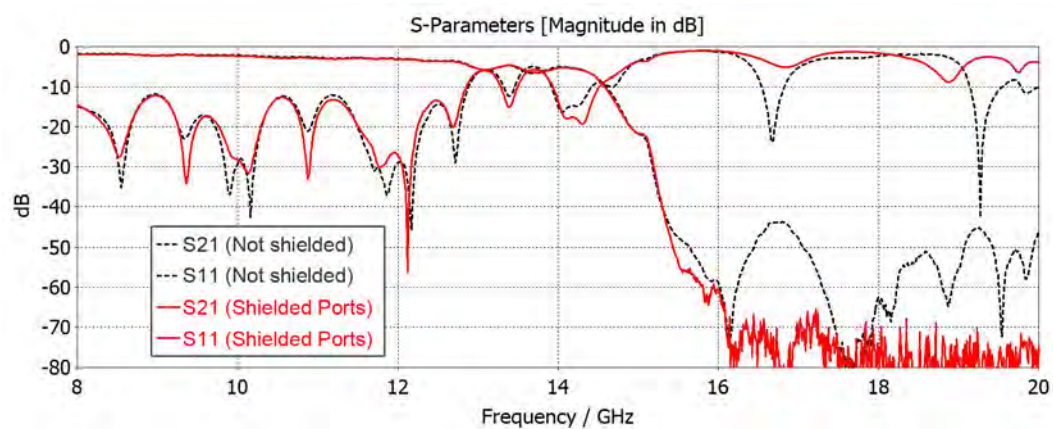


Figure 4.26: Results with or without SMA enclosures.

Figure 4.27 shows the comparison for filter B between SMA and SMPM transitions. Their response is very similar.

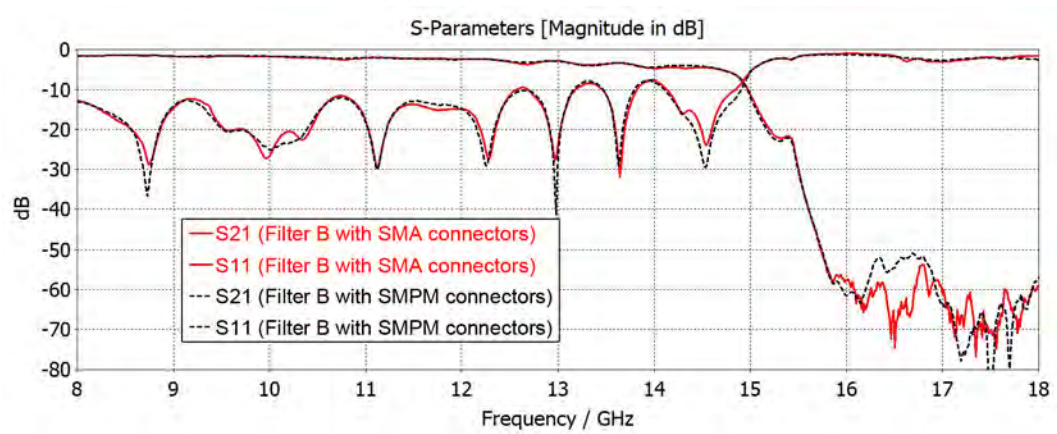


Figure 4.27: Comparison between SMPM and SMA transitions.

### 4.3.2 Measurement 2 - Multimode measurements in the stopband

For the multimode measurements an air waveguide-to-SIW transition, as seen in Figures 4.28 and 4.29, is used to measure the stopband response.

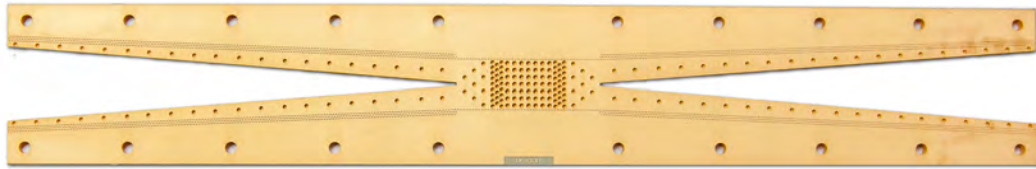


Figure 4.28: Filter A: WG-SIW-WG Classical Waffle iron filter.



Figure 4.29: Filter B: WG-SIW-WG Longer Waffle iron filter.

Two methods are used to measure the multimode in the stopband.

### First measuring method: 2.4 mm connector set-up

The test was conducted using a VNA and connecting each port to a 2.4 mm connector on the test structure as seen in Figure 4.30 below.

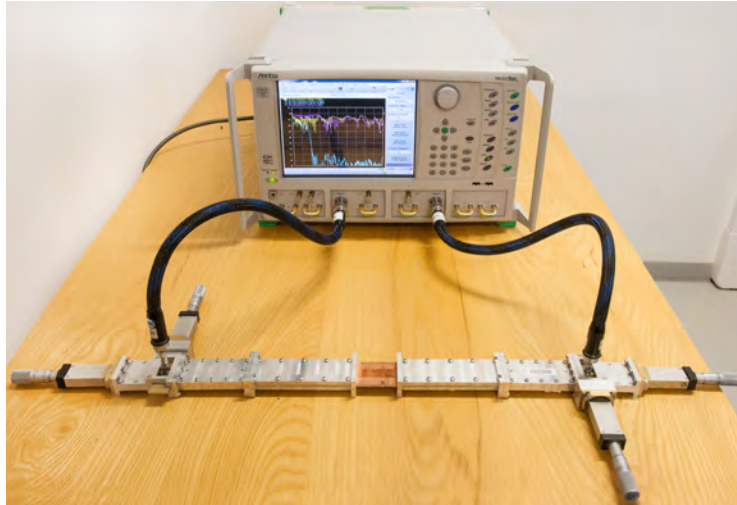


Figure 4.30: VNA test set-up.

### Batch 1 measurement results:

Figures 4.31 and 4.32 shows the different mode measurement results between the calibration PCB and filter A (short filter) and B (long filter). Comparing with the CAL PCB, both filter A and filter B have at least a 40 dB greater insertion loss in the stopband.

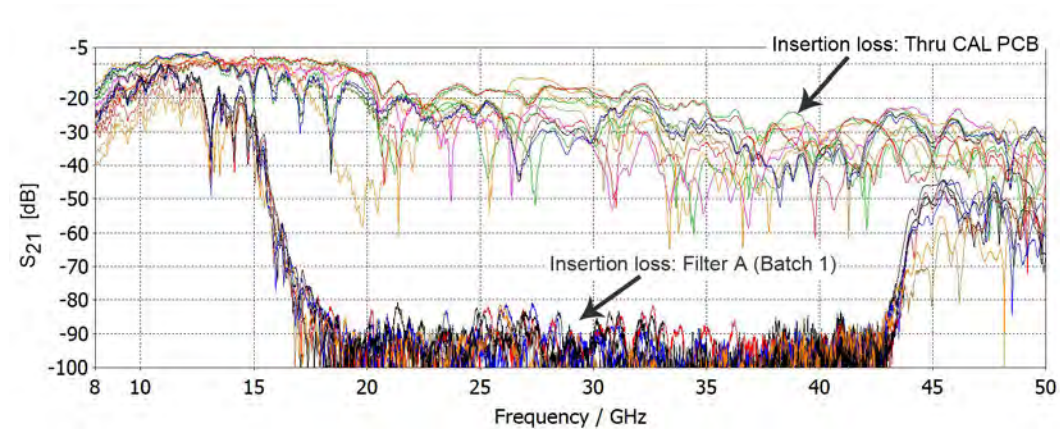


Figure 4.31: Comparison between the calibration PCB and filter A.



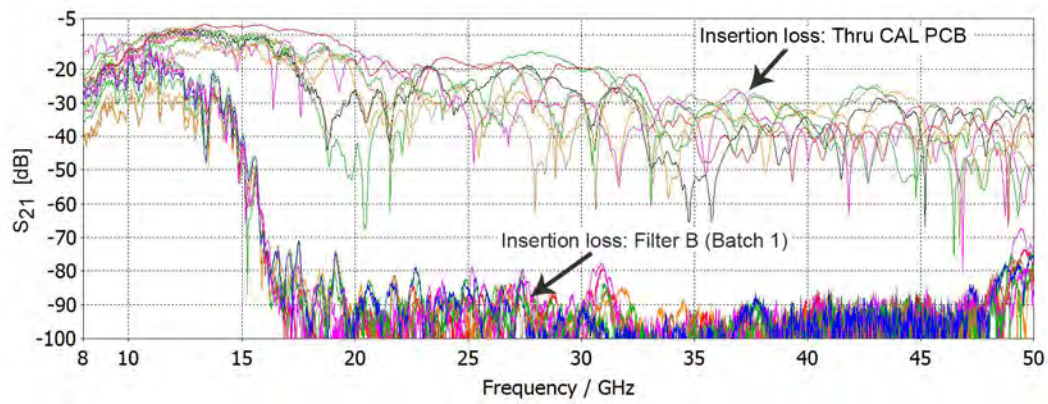


Figure 4.32: Comparison between the calibration PCB and filter B.

Looking only at filter A in Figure 4.33, it can be demonstrated that it attenuates the frequency band between 15 GHz and 43 GHz.

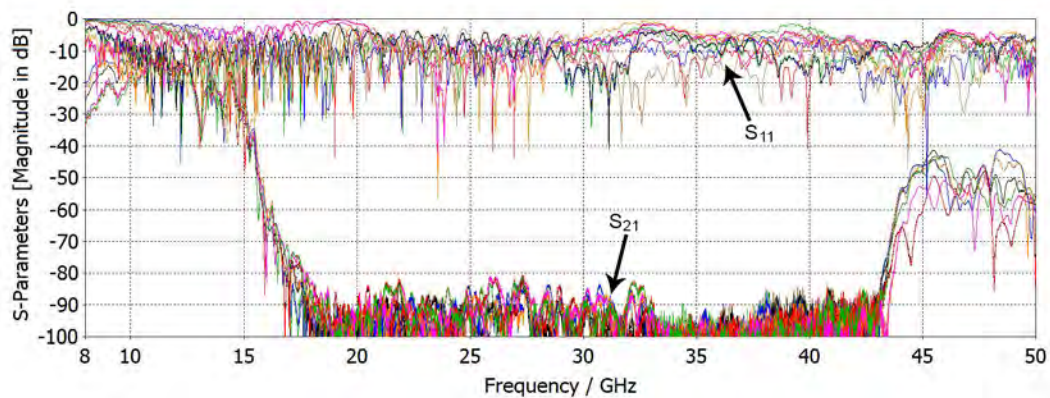


Figure 4.33: Filter A, batch 1 - stopband results.

Filter A has at least 10 dB more insertion loss in the stopband than filter B (Figure 4.34), but filter B attenuates higher than 48 GHz and not 43 GHz as seen in filter A.

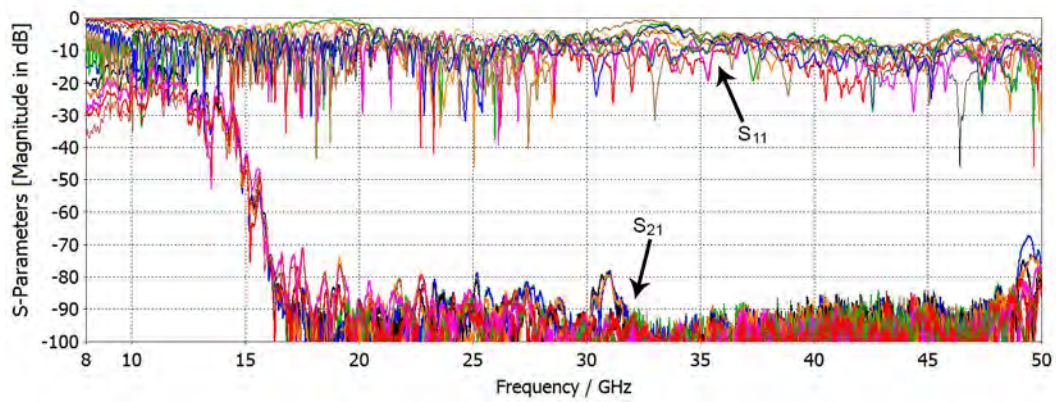


Figure 4.34: Filter B, batch 1 - stopband results.

#### Batch 2 measurement results:

Although the manufacturing process was improved during batch 2, the stopband results got worse. In Figures 4.35 and 4.36, the stopband results for filter A and B are shown.

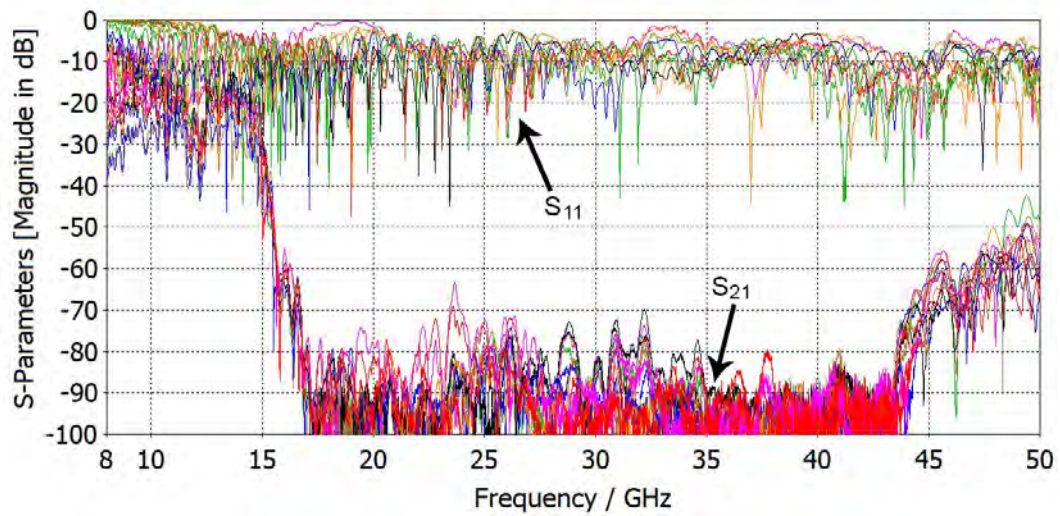


Figure 4.35: Filter A, batch 2 - stopband results.

Figure 4.36 shows the results of different mode measurements for filter B, batch 2.

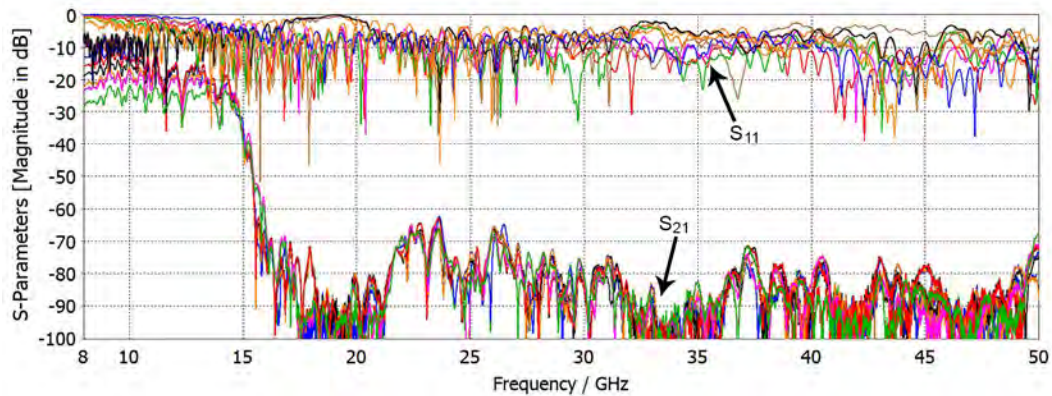


Figure 4.36: Filter B, batch 2 - stopband results.

Comparing filter A from batch 2 to batch 1 in Figure 4.37, the insertion loss is at least 30 dB less in the frequency range around 23 GHz. The same can be seen for filter B in Figure 4.38.

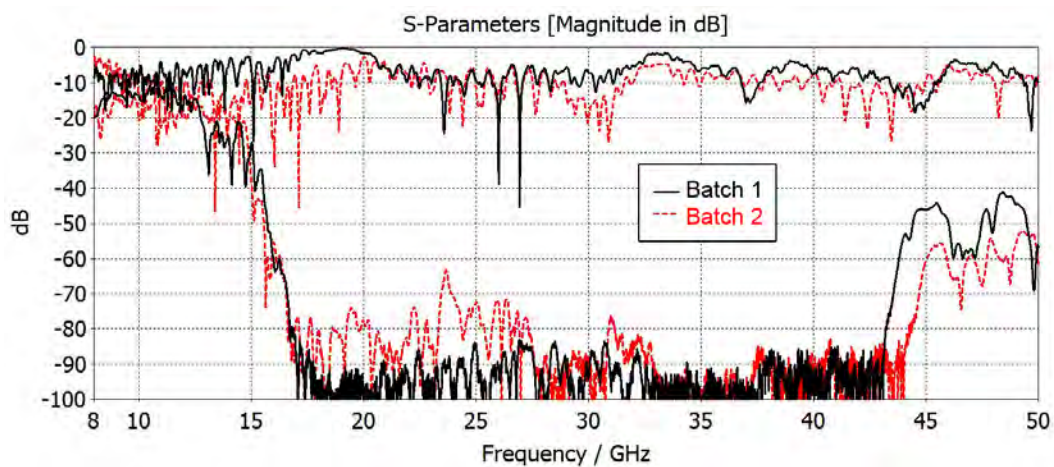


Figure 4.37: Filter A - Compare batch 1 and 2.

Both batches were mechanically inspected, and the results were compared. In Figure 4.39, it is shown that the 0.8 mm drill bit broke during the routing phase and a 6.5 mm slot on both sides of the dovetail can be seen. Also seen in Figure 4.40, the edge plating did not adhere so well to the PCB edge to form a grounding wall. Taking these two factors into account, it is proposed that the



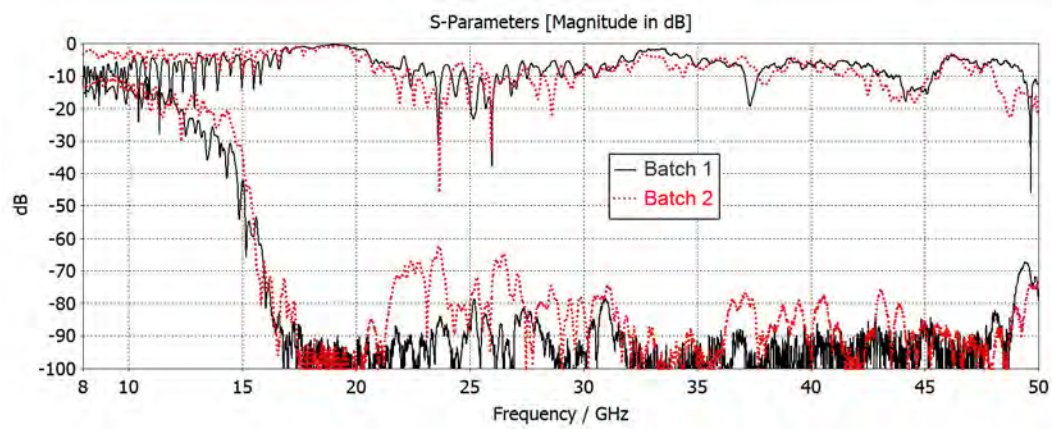


Figure 4.38: Filter B - Compare batch 1 and 2.

6.5 mm slots are  $\lambda/2$  for 23 GHz and acts as an antenna. Also, because the insertion loss measure around 80 dB in the stopband, it is essential to make sure no power leakage occurs and the edge plating in batch 2 did not prevent leakage.

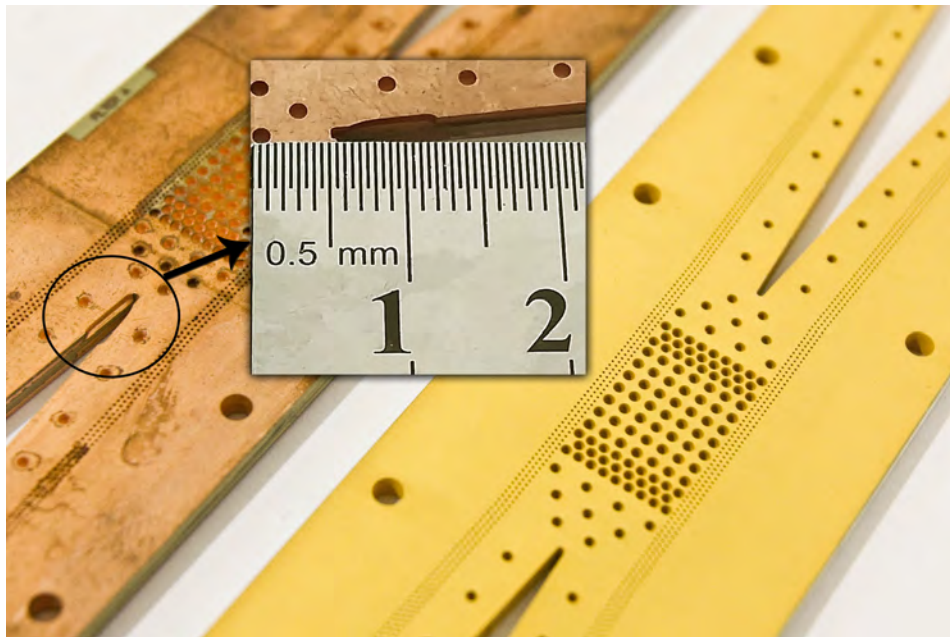


Figure 4.39: External inspection of the filter batches.

To verify the grounding hypothesis, a test is conducted where filter A from batch 2 is measured with additional clamps and copper tape used to seal the filter (Figure 4.41). It can be seen in Figure 4.42 that the insertion loss is at least 10 dB lower around 23 GHz.

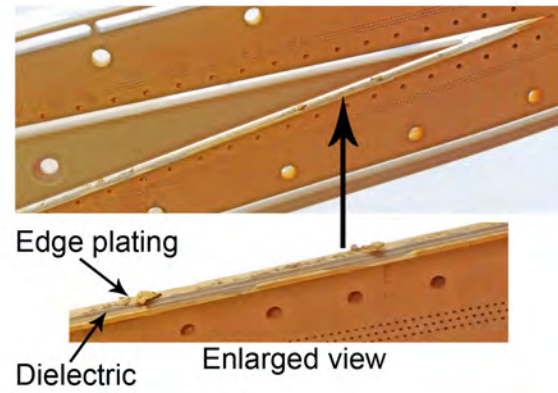


Figure 4.40: PCB batch 2 - Edge plating.



Figure 4.41: Sealing and clamping of the test set-up.

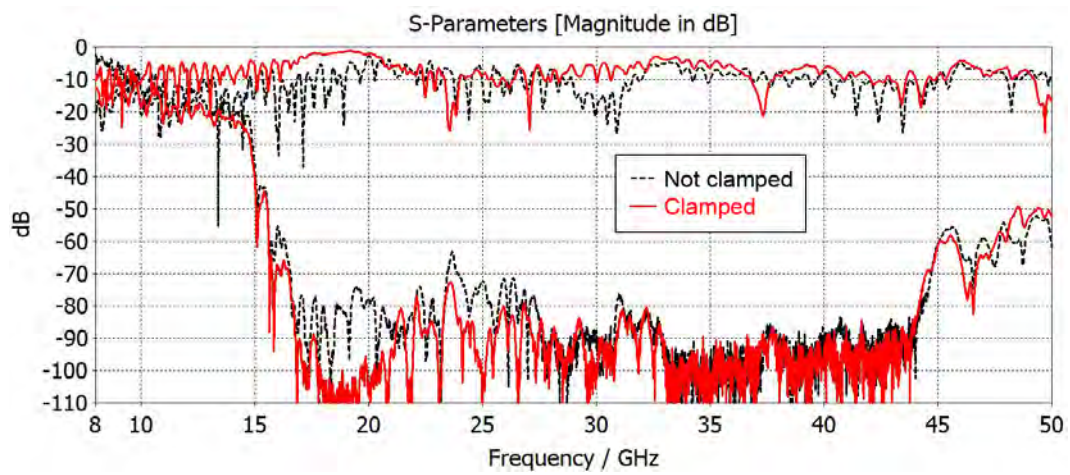


Figure 4.42: Filter A batch 2 - Compare results between filter structure clamped and not clamped.

### Second measuring method: antenna set-up

During each antenna measurement, the results showed similar responses and a combination of these results are shown in Figures 4.43 and 4.44, where the insertion loss in the stopband is compared between the Thru CAL PCB and filter A for batch 1 and 2 respectively.

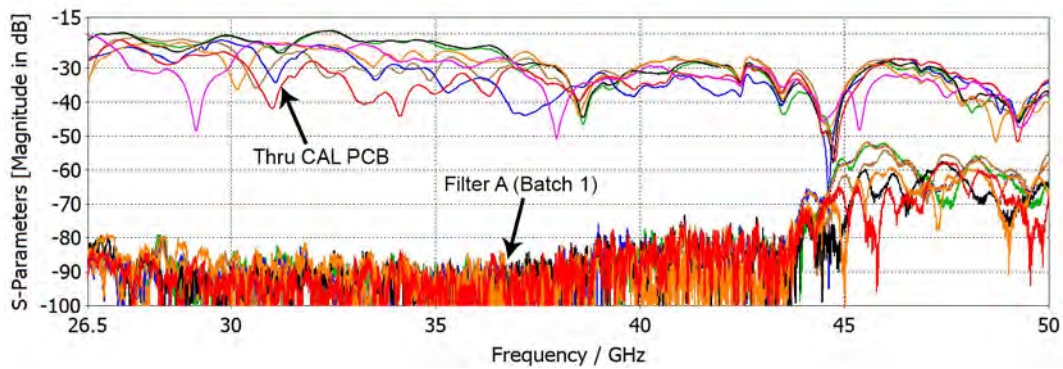


Figure 4.43: Antenna measurements for filter A from batch 1.

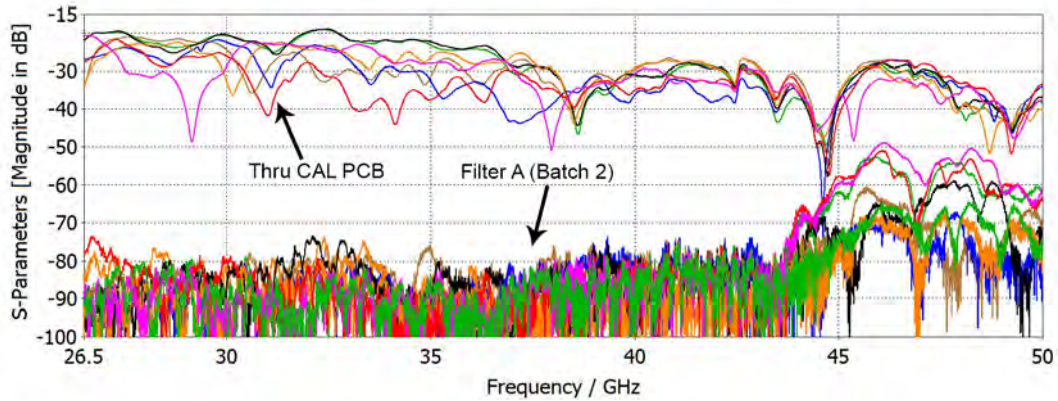


Figure 4.44: Antenna measurements for filter A from batch 2.

The results show that the insertion loss is less in batch 2 and this is due to the drilling and edging-plating problem that was stated in the previous subsection.

Figures 4.45 and 4.46 shows the insertion loss comparison between the Thru CAL PCB and filter B for batch 1 and 2 respectively. Again, the results show that the insertion loss in the stopband is less in batch 2.



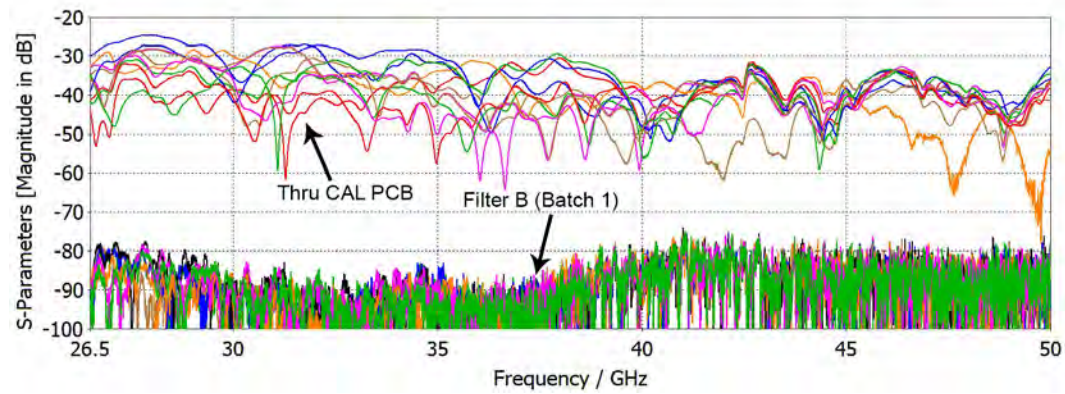


Figure 4.45: Antenna measurements for filter B from batch 1.

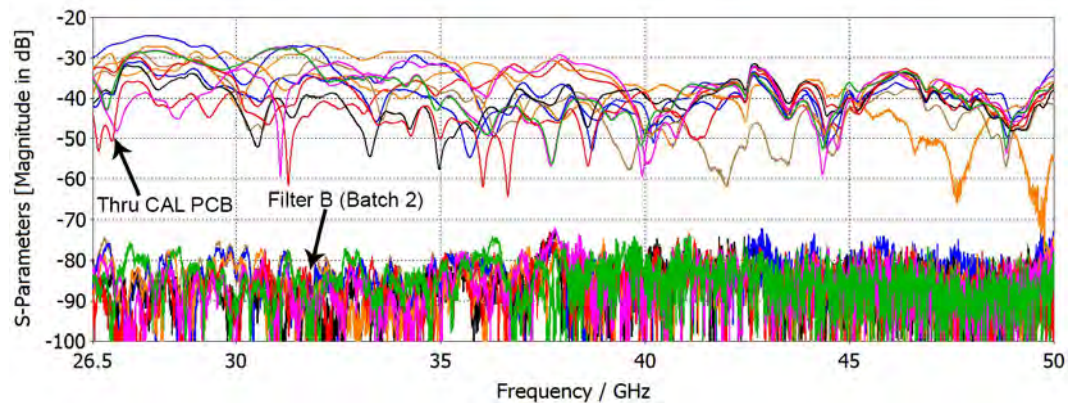


Figure 4.46: Antenna measurements for filter B from batch 2.

It is also evident that filter A has a smaller stopband response than filter B and this due to the extra peg (waffle) sections in filter B.

### 4.3.3 Measurement 3 - Power handling

The waffle-iron filter is designed for a pulsed communication system, with a average power level of 10 Watt. Only a 25 Watt (CW) power amplifier (PA) was able for the power measurements and for this reason it was decided to keep the test intervals to 1 minute. Both batches, using the SMA type filters, were tested at a frequency setting of 10 GHz.

For the calibration set-up, the 44.61 dBm (25 Watt) PA is connected to a 40 dB attenuator and measured as seen in Figure 4.47.

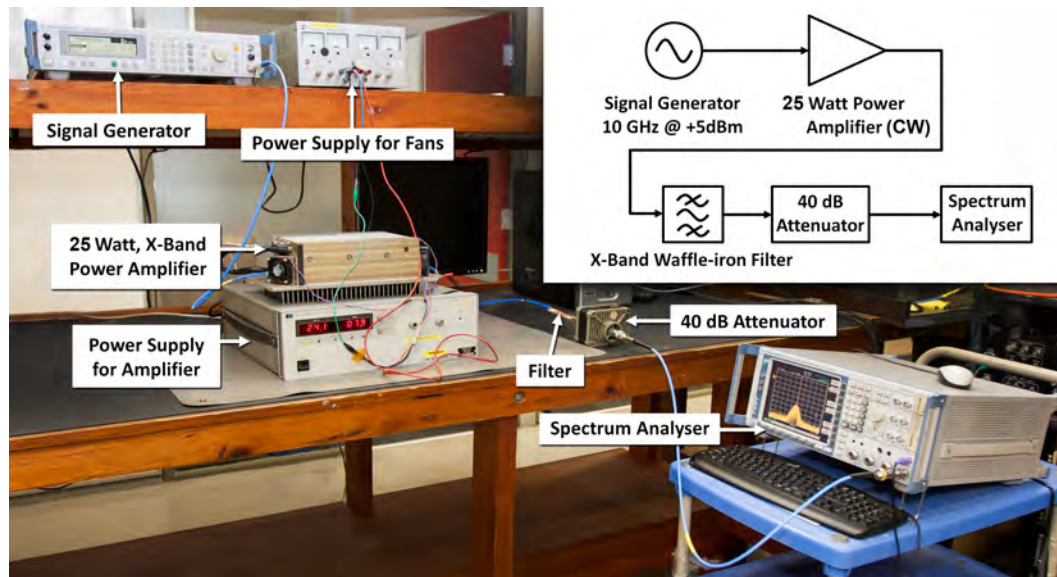


Figure 4.47: Power test set-up.

The combined cable and attenuator loss is 41.65 dB, and the 10 GHz signal strength, measured at the input of the spectrum analyser, is +2.96 dBm. For the power test, the filters are placed, one at a time, between the PA and the attenuator. The filters reached a maximum temperature of 64.6°C during test intervals of 1 minute each. All the filters from both batches showed excellent results. The calibration test set-up results is shown in Figure 4.48, where the PA's second harmonic is measured at 20 GHz, with a signal strength of -55.52 dBm. In Figure 4.49, filter B (batch 1) measured a 1.11 dBm (excluding the combined cable and attenuator loss of 41.65 dB) signal strength at 10 GHz and -83.96 dBm at 20 GHz.

The insertion loss over the bandpass section, for all the filters, were measured after the power tests and compared to the results before the power test. Figure 4.50 shows the response for the short filter design and Figure 4.51 shows the response for the long filter design. In both cases, the solid red line shows the response before the power tests and the black dashed line shows the results of the response after the test. The response in both filters is very similar. When considering how much voltage can be tolerated in a substrate, one needs to consider not just the dielectric breakdown voltage, but also the amount of resin present and possible resin starvation that can lead to air pockets, which in turn can degrade the voltage isolation performance of the final PCB. Care



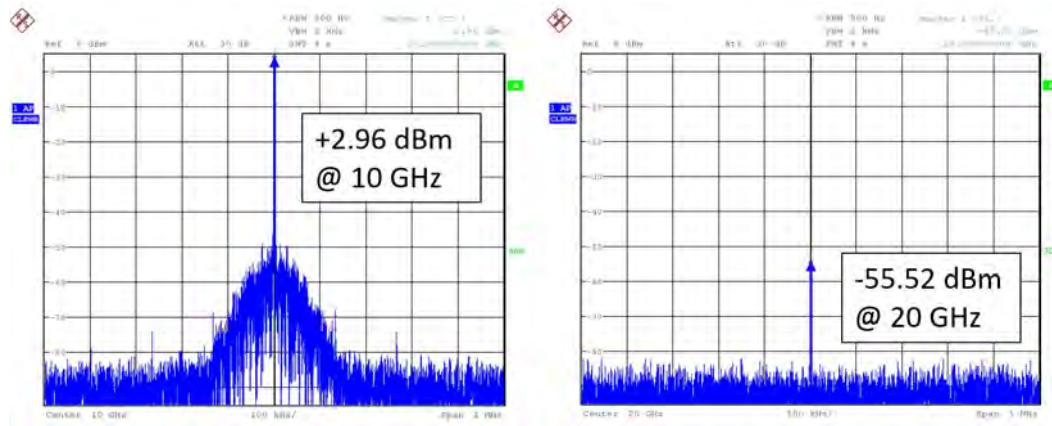


Figure 4.48: Calibration results for the power test set-up.

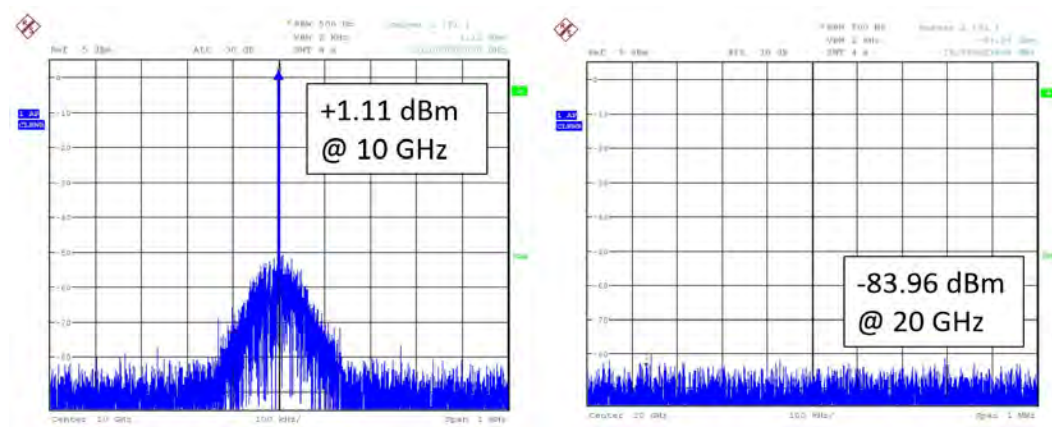


Figure 4.49: Power measurement results of filter B (batch 1).

should be taken to insure good resin content to uphold the voltage isolation property of the substrate. In the case of the test board, the electric field strength of the *Mercurywave*<sup>TM</sup> 9350 substrate is 590 kV/mm, which refers to the safe operating point of the substrate. The actual breakdown voltage is in excess of 50 kV.

#### 4.3.4 Summary and concluding remarks

Two types of MSIW waffle-iron filters were tested. Filter A is a classic MSIW waffle-iron filter, whereas filter B is an extended version with an extra step in the middle of the filter. Two PCB panels, containing both types of filters, were manufactured. The filter pegs in panel 1 (batch 1) do not align vertically, but the filters still performed well. The filter pegs in panel 2 (batch 2) are aligned, but the edge plating did not adhere well to the hole's wall, thus reducing the effectiveness in forming a RF wall. A drill bit also broke during the routing phase and damaged the filter. This led to substandard results in the stopband.

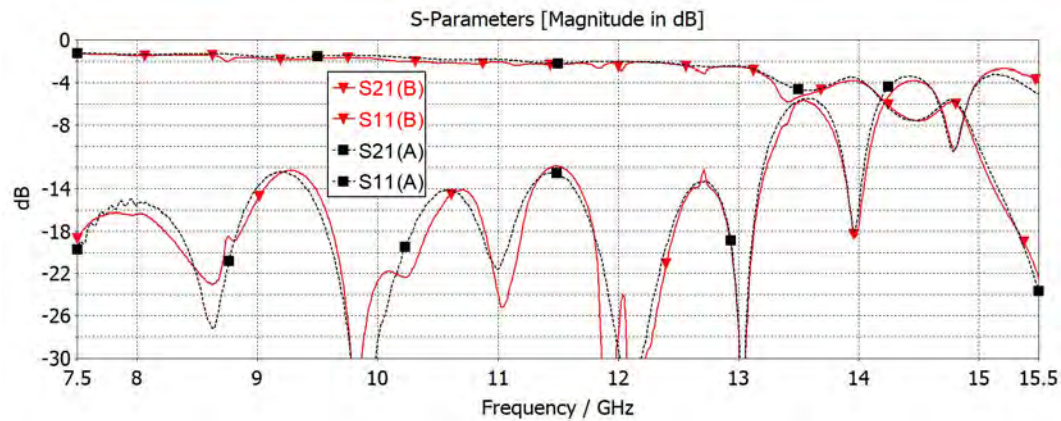


Figure 4.50: Short Filter: Measurements before and after the power test.

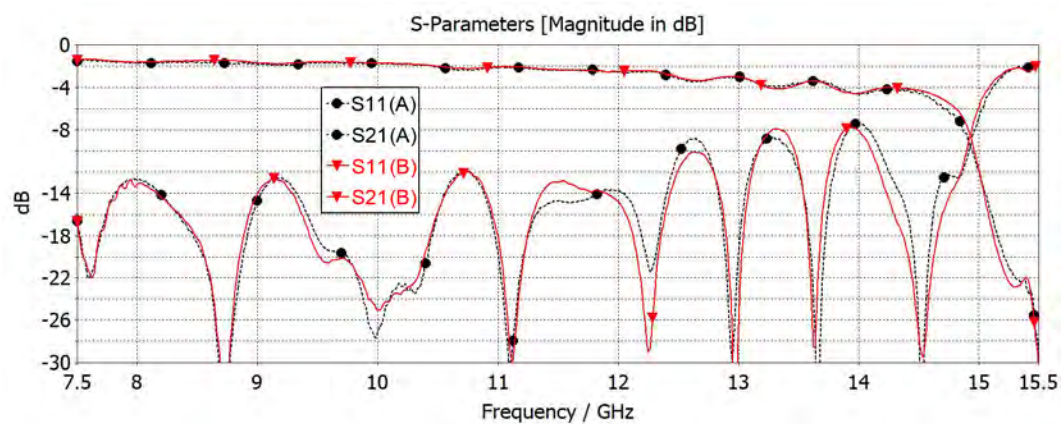


Figure 4.51: Long Filter: Measurements before and after the power test.

Both panels were tested for its passband response, multimode response in the stopband as well as power handling. The multimode measurements are conducted using two methods and both yielded consistent similar results, proving that the higher order modes are being attenuated. The filters displayed less than -12 dB passband reflection over 8.5 to 10.5 GHz, with stopband attenuation in excess of 70 dB over the harmonic bands 15 to 43 GHz for filter A and 15 to 49 GHz for filter B. The prototypes were designed to handle 10 Watt average power in a pulsed transmitter circuit, but were successfully tested using a 25 Watt (CW) power amplifier. A good correlation is obtained between synthesised and measured responses in these two designs.

## Chapter 5

# Conclusion

The main objective of this thesis was the design and manufacturing of a Multilayered Substrate Integrated Waveguide (MSIW) Waffle-iron Filter. Two filter versions were designed namely, filters A and B. Filter A is the classical SIW Waffle iron filter and Filter B is an extended version of Filter A with an extra step in the middle of the filter, to extend the stopband width.

In Chapter 1 the background into Waffle-iron and SIW filters were described. It also highlighted the different methods, until now, for measuring the scattering parameters of multimode waveguide filters.

An in-depth SIW design methodology and PCB manufacturing process was shown in Chapter 2.

The design and manufacturing of Filter A and B, two iterations of each, were discussed in Chapter 3.

Chapter 4 presented two methods to measure a multimode waveguide filter. All the different measurement methods were examined. It was concluded that the alignment of the MSIW Waffle-iron filter pegs are not as important as in normal metallic Waffle-iron filters. The grounding between the air waveguide and the dielectric transitions, on the other hand, plays a very important roll in the stopband response of the filter. The prototypes presented, displayed less than -12 dB passband reflection over 8.5 to 10.5 GHz, with stopband attenuation in excess of 70 dB over the harmonic bands 15 to 43 GHz for filter A and 15 to 48 GHz for filter B. The prototypes were designed to handle 10 Watt average power in the transmitted band. A good correlation is obtained between synthesised and measured responses in these two designs.

# Appendices

# Appendix A

## MercuryWave 9350

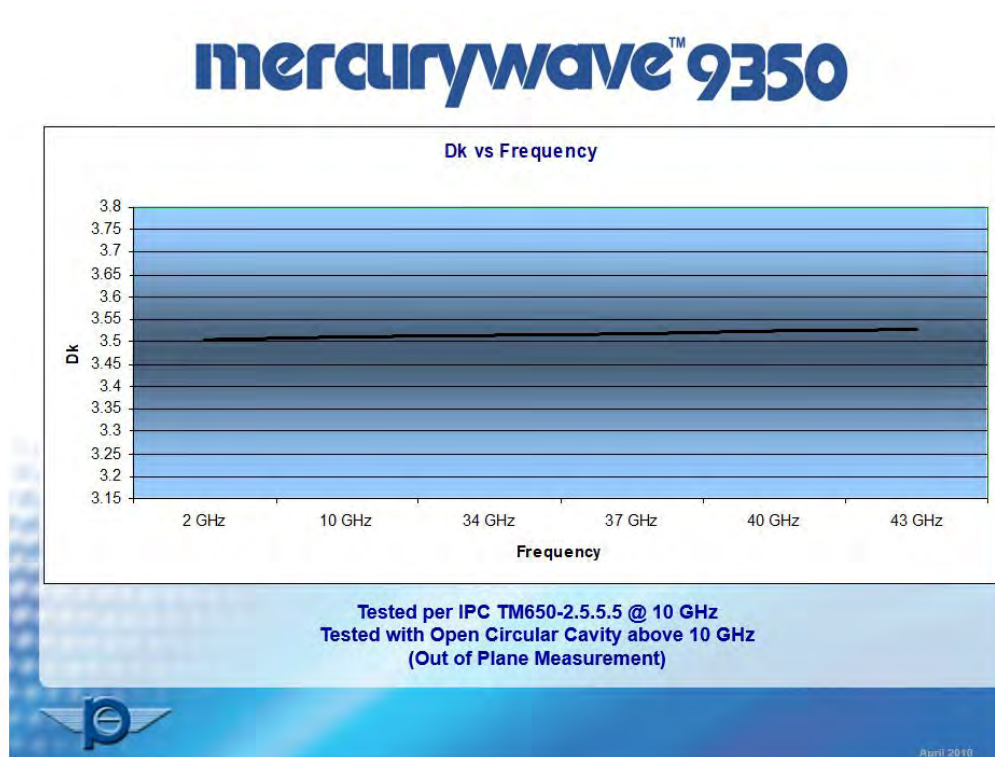


Figure A.1: Dielectric constant changing with frequency.

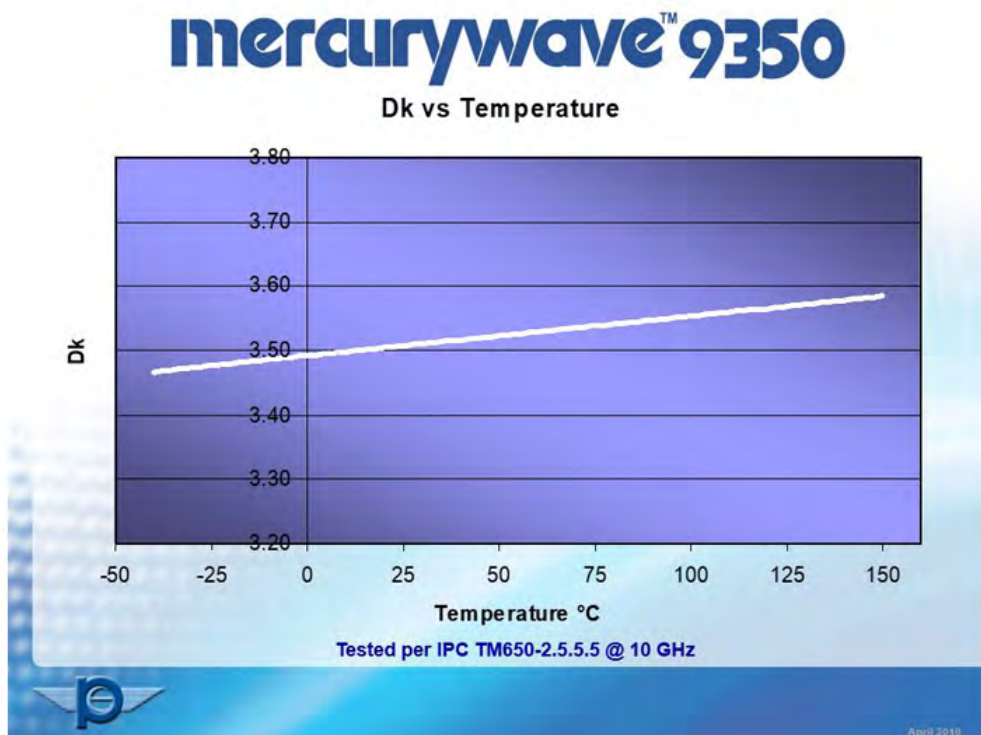



Figure A.2: Dielectric constant changing with temperature.

## Mercurywave™ 9350 Comparison to 4103/11

A new slash sheet designation has been submitted for Mercurywave™ 9350



	4103/11	Mercurywave 9350	Units
Peel Strength 1.oz Foil			
Low Profile Foil (sub 1 micron)	N/A	5	Lbs/in
Standard Foil			
After Thermal Stress	3	7	Lbs/in
At 150C	3	7	Lbs/in
After Process Solutions	3	8	Lbs/in
Volume Resistivity			
96/35/90	10 <sup>4</sup> 5	10 <sup>4</sup> 7	MΩ-cm
24/125	10 <sup>4</sup> 4	10 <sup>4</sup> 6	MΩ-cm
Surface Resistivity			
96/35/90	10 <sup>4</sup> 3	10 <sup>4</sup> 5	MΩ
24/125	10 <sup>4</sup> 2	10 <sup>4</sup> 6	MΩ
Moisture Absorption	0.25	0.15	%
Dielectric Breakdown	30	>50	kV
Permittivity 10 GHz	3.48 - 3.60	3.5	
Loss Tangent 10 GHz	0.006	0.004	
Flexural Strength			
Length Direction	310	606	N/mm <sup>2</sup>
Cross Direction	228	428	N/mm <sup>2</sup>
Thermal Stress 10 s @ 288 C	Pass	Pass	s
Electric Strength	N/A	1500	V/mil
Flammability			
Average Burn Time	50	94-V0	s
Individual Burn Time	10	94-V0	s
CTE			
X/Y Axes	N/A	10-14	ppm/C
Z Axis	N/A		
61		48	ppm/C
62		245	ppm/C

Figure A.3: Mercurywave™ 9350 specifications.



**mercurywave™ 9350 Thermal Properties**

Property	Mercurywave™ 9350	N4350-13RF	N4000-29
T <sub>g</sub> (DSC)	≥200°C*	210°C	185°C
T <sub>d</sub> (TGA)	360°C	350°C	350°C
T <sub>260</sub>	200 min.	> 30 min.	> 60 min.
T <sub>288</sub>	40 min.	>10 min.	15 min.
T <sub>300</sub>	18 min.	0 min.	3-5 min.
Solder Float (4"x4" Cu Clad 288°C time to failure)	>600 sec.	>470 sec.	>600 sec.
Pressure Cooker (1 hr.)			
Moisture Gain	0.15%	0.10%	0.15%
Solder Dip (288°C)	>600 sec.	>600 sec.	>600 sec.

**\* T<sub>g</sub> by DMA**

April 2019

Figure A.4: Mercurywave™ 9350 thermal properties.



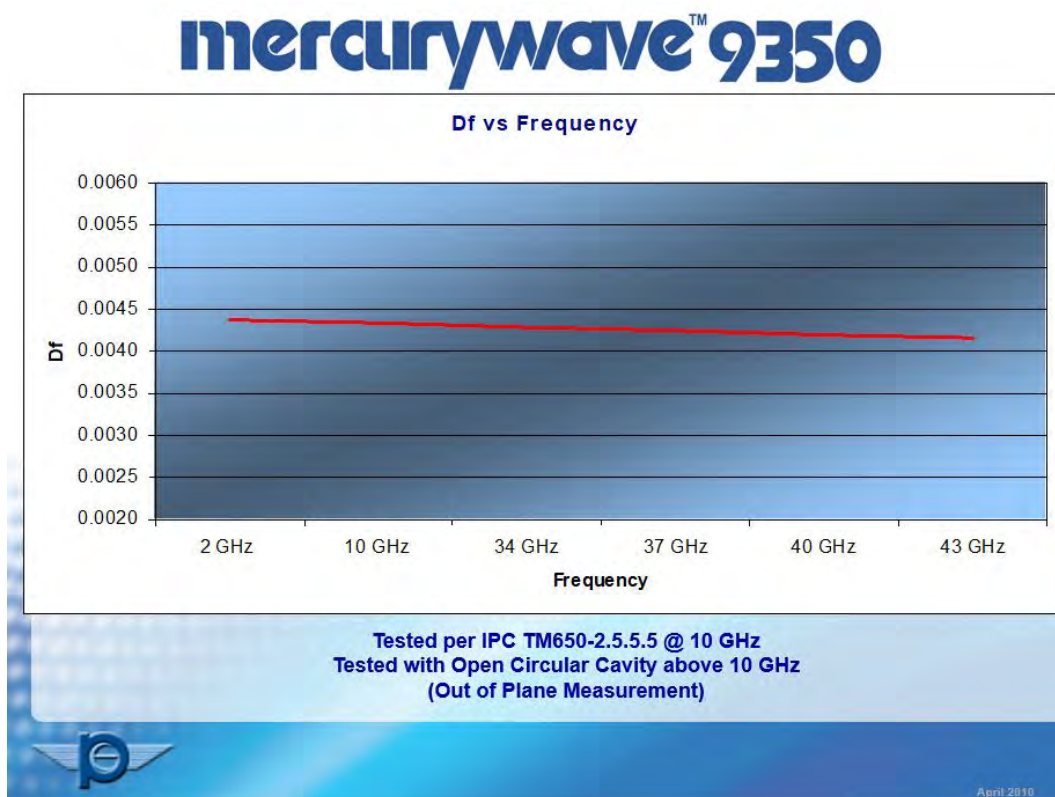


Figure A.5: *Mercurywave*<sup>TM</sup> 9350 loss tangent changing with frequency.

# Bibliography

- [1] L. Huang and N. Yuan, "A Compact Wideband SIW Bandpass Filter with Wide Stopband and High Selectivity," *MDPI Electronics*, pp. 1–12, April 2019.
- [2] G. Matthaei, L. Young, and E. Jones, *Microwave Filters, Impedance-Matching Networks and Coupling Structures*. McGraw-Hill Book Co, 1964.
- [3] X. P. Chen and K. Wu, "Substrate Integrated Waveguide Filter, Basic Design Rules and Fundamental Structure Features," *IEEE Microwave Magazine*, vol. 15, no. 5, pp. 108–116, July 2014.
- [4] L. G. Maloratsky, *RF and Microwave Integrated Circuits, Passive Components and Control Devices*. Elsevier Inc., 2004.
- [5] D. Deslandes and K. Wu, "Accurate modeling, wave mechanisms, and design considerations of a substrate integrated waveguide," *IEEE Transactions on Microwave Theory and Techniques*, vol. 54, no. 6, pp. 2516–2526, June 2006.
- [6] Y. Cassivi, L. Perregrini, K. Wu, and G. Conciauro, "Low-cost and High-Q millimeter-wave resonator using substrate integrated waveguide technique," *Proc. European Microwave Conf., Milan, Italy*, pp. 1–4, September 2002.
- [7] M. Salehi, E. Mehrshahi, and R. Rezaiesarlak, "Stopband improvement of substrate integrated waveguide filters using slotted ground structures," *Proc. Asia-Pacific Microw. Conf., Yokohama, Japan*, pp. 1717–1719, December 2010.
- [8] M. Salehi and E. Mehrshahi, "Spurious-response suppression of substrate integrated waveguide filters using multishape resonators and slotted plane structures," *Int. J. RF Microwave Computer Aided Eng.*, vol. 21, no. 6, pp. 650–657, November 2011.
- [9] I. W. Lee, H. Nam, T. S. Yun, and J. C. Lee, "Spurious suppressed substrate integrated waveguide bandpass filter using stepped impedance res-

- onator,” *J. Korean Inst. Electromagn. Eng. Sci.*, vol. 10, no. 1, pp. 1–5, March 2010.
- [10] W. M. Fathelbab and M. J. Almalkawi, “A stepped-impedance substrate integrated waveguide bandpass filter,” *Proc. IEEE Radio Wireless Symp., New Orleans, LA*, pp. 332–334, January 2010.
  - [11] L. S. Wu, J. Mao, W. Y. Yin, and X. L. Zhou, “Broadband filter based on stub-loaded ridge substrate integrated waveguide in low temperature cofired ceramic,” *Proc. IEEE Electrical Design of Advanced Packaging and Systems Symp.*, pp. 1–4, December 2011.
  - [12] F. Zhu, W. Hong, J. X. Chen, and K. Wu, “Wide stopband substrate integrated waveguide filter using corner cavities,” *Electronics Letters*, vol. 49, no. 1, pp. 50–52, January 2013.
  - [13] D. Jia, Q. Feng, Q. Xiang, and K. Wu, “Multilayer Substrate Integrated Waveguide (SIW) Filters With Higher-Order Mode Suppression,” *IEEE Microwave and Wireless Components Letters*, vol. 26, no. 9, pp. 678–680, September 2016.
  - [14] M. Dong, D. Shen, X. Zhang, W. Ren, Z. Ma, R. Qian, and H. Yuan, “Substrate Integrated Gap Waveguide Bandpass Filters with High Selectivity and Wide Stopband,” *2018 IEEE/MTT-S International Microwave Symposium (IMS)*, June 2018.
  - [15] R. Moro, S. Moscato, M. Bozzi, and L. Perregrini, “Substrate Integrated Folded Waveguide Filter with Out of Band Rejection Controlled by Resonant Mode Suppression,” *IEEE Microwave and Wireless Components Letters*, vol. 25, no. 4, pp. 214–216, April 2015.
  - [16] C. Fan, W. Choi, W. Yang, W. Che, and K. Tam, “A Low Cross-Polarization Reflect array Antenna Based on SIW Slot Antenna,” *IEEE Antennas and Wireless Propagation Letters*, vol. 16, pp. 333–336, June 2017.
  - [17] Z. Zhang, X. Cao, J. Gao, S. Li, and J. Han, “Broadband SIW Cavity-Backed Slot Antenna for End-fire Applications,” *IEEE Antennas and Wireless Propagation Letters*, vol. 17, no. 7, pp. 1271–1275, July 2018.
  - [18] H. Jamshidi-Zarmehri and M. H. Neshati, “Design and Development of High-Gain SIW H-Plane Horn Antenna Loaded with Waveguide, Dipole Array, and Reflector Nails Using Thin Substrate,” *IEEE Transactions on Antennas and Propagation*, vol. 67, no. 4, pp. 369–384, February 2019.
  - [19] T. Cheng, W. Jiang, S. Gong, and Y. Yu, “Broadband SIW Cavity-Backed Modified Dumbbell-Shaped Slot Antenna,” *IEEE Antennas and Wireless Propagation Letters*, vol. 18, no. 5, pp. 936–940, May 2019.

- [20] W. Q. Che, E. K. N. Yung, K. Wu, and X. D. Nie, "Design investigation on millimeter-wave ferrite phase shifter in substrate integrated waveguide," *Progress in Electromagnetics Research*, vol. 45, pp. 263–275, 2004.
- [21] T. Yang, M. Ettorre, and R. Sauleau, "Novel Phase Shifter Design Based on Substrate-Integrated-Waveguide Technology," *IEEE Microwave and Wireless Components Letters*, vol. 22, no. 10, pp. 518–520, September 2012.
- [22] B. Veadesh, S. Aswin, and K. Shambavi, "Design and analysis of C-band SIW directional coupler," *2017 International conference on Microelectronic Devices, Circuits and Systems (ICMDCS)*, Aug 2017.
- [23] X. Shi and X. Zhu, "Design of Cruciform Directional Coupler with Capacitive Slots Based on SIW," *2018 International Conference on Microwave and Millimeter Wave Technology (ICMMT)*, May 2018.
- [24] M. Pasian, L. Silvestri, C. Rave, M. Bozzi, L. Perregrini, A. F. Jacob, and K. K. Samanta, "Substrate-Integrated-Waveguide E-Plane 3-dB Power-Divider/Combiner Based on Resistive Layers," *IEEE Transactions on Microwave Theory and Techniques*, vol. 65, no. 5, pp. 1498–1510, January 2017.
- [25] J. Chen, W. Hong, H. Tang, X. Yin, and K. Wu, "A compact millimeter-wave mixer module," *2005 Asia-Pacific Microwave Conference Proceedings*, December 2005.
- [26] Z. Zhang, Y. R. Wei, and K. Wu, "Broadband Millimeter-Wave Single Balanced Mixer and Its Applications to Substrate Integrated Wireless Systems," *IEEE Transactions on Microwave Theory and Techniques*, vol. 60, no. 3, pp. 660–669, March 2012.
- [27] A. Collado, F. Mira, and A. Georgiadis, "Mechanically Tunable Substrate Integrated Waveguide (SIW) Cavity Based Oscillator," *IEEE Microwave and Wireless Components Letters*, vol. 23, no. 9, pp. 489–491, September 2013.
- [28] Z. Cai, X. Tang, T. Zhang, and Y. Yang, "An X-band Low Phase Noise Oscillator with High Harmonic Suppression Using SIW Quarter-Wavelength Resonator," *2018 IEEE/MTT-S International Microwave Symposium (IMS)*, June 2018.
- [29] R. Zhang, J. Zhou, Z. Yu, and B. Yang, "A Low Phase Noise Feedback Oscillator Based on SIW Bandpass Response Power Divider," *IEEE Microwave and Wireless Components Letters*, vol. 28, no. 2, pp. 153–155, January 2018.

- [30] A. Ayaran, J. B. K., and S. Golmohammadi, "Substrate Integrated Waveguide Band-Pass Filter with CPWG fed for RADAR application in X-Band," *International Journal of Electronics; Mechanical and Mechatronics Engineering*, vol. 3, no. 2, pp. 553–556, 2014.
- [31] C. Zhao, C. Fumeaux, and C. Lim, "Folded Substrate-Integrated Waveguide Band-Pass Post Filter," *IEEE Microwave and Wireless Components Letters*, vol. 27, no. 1, pp. 22–24, January 2017.
- [32] T. R. Jones and M. Daneshmand, "Miniaturized Slotted Bandpass Filter Design Using a Ridged Half-Mode Substrate Integrated Waveguide," *IEEE Microwave and Wireless Components Letters*, vol. 26, no. 5, pp. 334–336, May 2016.
- [33] S. Saeedi and H. H. Sigmarsson, "Miniaturized evanescent-mode cavity SIW bandpass filter with spurious suppression," *2018 IEEE Radio and Wireless Symposium (RWS)*, March 2018.
- [34] A. Parameswaran and S. Raghavan, "Novel SIW dual mode band pass filter with high skirt selectivity," *2017 2nd International Conference for Convergence in Technology (I2CT)*, April 2017.
- [35] X. Wu, Q. Chu, X. Tian, and X. Ouyang, "Quintuple-Mode UWB Bandpass Filter With Sharp Roll-Off and Super-Wide Upper Stopband," *IEEE Microwave and Wireless Components Letters*, vol. 21, no. 12, pp. 661–663, October 2011.
- [36] M. Khalil, M. Kamarei, J. Jomaah, and H. Ayad, "Compact multilayer Band-Pass filter in Substrate Integrated Waveguide (SIW) technology," *2016 IEEE Middle East Conference on Antennas and Propagation (MECAP)*, September 2016.
- [37] A. C. Beck, "Measurement Technique for Multimode Waveguides," *IRE Trans. Microwave Theory Tech.*, pp. 35–41, April 1955.
- [38] L. Felsen, W. Khan, and L. Levey, "Measurement of Two-Mode Discontinuities in a Multimode Waveguide by a Resonance Technique," *IRE Trans. Microwave Theory Tech.*, pp. 102–110, January 1959.
- [39] V. Price, "Measurement of Harmonic Power Generated by Microwave Transmitters," *IRE Trans. Microwave Theory Tech.*, pp. 116–120, January 1959.
- [40] E. D. Sharp and E. M. T. Jones, "A Sampling Technique for the Measurement of Multimode Harmonic Waveguide Power," *IRE Trans. Microwave Theory Tech.*, pp. 73–82, January 1961.

- [41] D. S. Levinson and I. Rubinstein, "A Technique for Measuring Individual Modes Propagating in Overmoded Waveguide," *IEEE Trans. Microwave Theory Tech.*, vol. 14, pp. 310–322, July 1966.
- [42] J. J. Taub and J. Goldberg, "A New Technique for Multimode Power Measurement," *IRE Trans. Microwave Theory Tech.*, pp. 64–69, 1962.
- [43] Y. Carmel, K. R. Chu, M. E. Read, V. L. Granatstein, G. Faillon, P. Boulanger, E. Kammerer, and G. Mourier, "A Technique to Identify Electromagnetic Modes in Oversize Waveguides," *IEEE Trans. Microwave Theory Tech.*, vol. MTT-32, pp. 1493–1495, 1984.
- [44] C. Seguinot, P. Kennis, J. Legier, F. Huret, E. Paleczny, and L. Hayden, "Multimode TRL, A New Concept in Microwave Measurements, Theory and Experimental Verification," *IEEE Trans. Microwave Theory Tech.*, vol. 46, pp. 536–542, May 1998.
- [45] X. P. Chen and K. Wu, "Substrate Integrated Waveguide Filter, Design Techniques and Structure Innovations," *IEEE Microwave Magazine*, vol. 15, no. 6, pp. 121–133, September 2014.
- [46] X. P. Chen and K. Wu, "Substrate Integrated Waveguide Filter, Practical Aspects and Design Considerations," *IEEE Microwave Magazine*, vol. 15, no. 7, pp. 75–83, November 2014.
- [47] K. Wu, "Integration and interconnect techniques of planar and nonplanar structures for microwave and millimeter-wave circuits-current status and future trend," *Asia-Pacific Microwave Conference*, pp. 411–416, December 2001.
- [48] F. Xu and K. Wu, "Guided-wave and leakage characteristics of substrate integrated waveguide," *IEEE Trans. Microwave Theory Tech.*, vol. 53, no. 1, pp. 66–73, January 2005.
- [49] L. Simonovich, "Practical Method for Modeling Conductor Surface Roughness Using the Cannonball Stack Principle, Issue 2.0," *LAMSIM Enterprises Inc.*, April 2015.
- [50] S. B. Cohn, E. M. T. Jones, O. Heinz, J. K. Shimizu, B. M. Schiffman, and F. S. Coale, "Research on design criteria for microwave filter," *Stanford Research Institute, Final Report SRI Project 1331*, June 1957.
- [51] S. B. Cohn, C. Flammer, E. M. T. Jones, and B. M. Schiffman, "Design criteria for microwave filters and coupling structures," *Stanford Research Institute, Technical Report 2 SRI Project 2326*, June 1958.
- [52] S. B. Cohn, "Broad-band waveguide filter," *U.S. Patent 3 046 503*, July 1962.

- [53] L. Young, "Postscript to two papers on waffle-iron filters (correspondence)," *IEEE Transactions on Microwave Theory and Techniques*, vol. 11, no. 6, pp. 555–557, November 1963.
- [54] J. Caputo and F. Bell, "Waffle-iron harmonic suppression filter," *IEEE Transactions on Microwave Theory and Techniques*, vol. 13, no. 5, pp. 701–703, September 1965.
- [55] S. B. Cohn, "Design relations for the wide-band waveguide filter," *Proceedings of the IRE*, vol. 38, no. 7, pp. 799–803, July 1950.
- [56] N. Marcuvitz, *Waveguide Handbook*. McGraw-Hill Book Co, 1951.
- [57] L. Young and B. M. Schiffman, "New and improved types of waffle-iron filters," *Proceedings of the IEE*, vol. 110, pp. 1191–1198, July 1963.
- [58] T. Stander and P. Meyer, "High-power broadband absorptive waveguide filters," PhD, University of Stellenbosch, 2009.
- [59] F. Arndt and J. Brandt, "Direct EM based optimization of advanced waffle-iron and rectangular combline filters," in *IEEE MTT-S International Microwave Symposium Digest*, June 2002.
- [60] F. Arndt, R. Beyer, W. Hauth, D. Schmitt, and H. Zeh, "Cascaded wide stop band waffle-iron filter designed with a MM/FE CAD method," in *29th European Microwave Conference*, 1999.
- [61] M. B. Manuilov and K. V. Kobrin, "Field theory CAD of waffle-iron filters," in *35th European Microwave Conference*, October 2005.
- [62] E. D. Sharp, "A high-power wide-band waffle-iron filter," *IEEE Transactions on Microwave Theory and Techniques*, vol. MTT-11, no. 2, pp. 111–116, March 1963.
- [63] D. M. Pozar, *Microwave Engineering*, 4th ed. John Wiley and Sons, Inc., 2012.
- [64] F. Sabath, E. L. Mokole, and S. N. Samaddar, "Definition and Classification of Ultra-Wideband Signals and Devices," *The Radio Science Bulletin*, no. 313, June 2005.
- [65] S. Lee, S. Jung, and H. Lee, "Ultra-Wideband CPW-to-Substrate Integrated Waveguide Transition Using an Elevated-CPW Section," *IEEE Microw. Wireless Compon. Lett.*, vol. 18, no. 11, pp. 746–747, November 2008.



- [66] F. Taringou, T. Weiland, and J. Bornemann, "Broadband design of substrate integrated waveguide to stripline interconnect," *International Conference on Numerical Electromagnetic Modeling and Optimization for RF, Microwave, and Terahertz Applications (NEMO)*, no. 6, pp. 1–4, 2014.
- [67] S. Lin, S. Yang, A. E. Fathy, and A. Elsherbini, "Development of a novel UWB Vivaldi antenna array using SIW technology," *Progress In Electromagnetics Research*, vol. 90, pp. 369–384, June 2009.
- [68] X. P. Chen and K. Wu, "Low-loss ultra-wideband transition between conductor-backed coplanar waveguide and substrate integrated waveguide," *IEEE MTT-S International Microwave Symposium Digest*, pp. 349–352, June 2010.
- [69] F. Taringou, D. Dousset, J. Bornemann, and K. Wu, "Substrate-integrated waveguide transitions to planar transmission-line technologies," *IEEE/MTT-S International Microwave Symposium Digest*, pp. 1–3, 2012.
- [70] Z. Kordiboroujeni and J. Bornemann, "New Wideband Transition from Microstrip Line to Substrate Integrated Waveguide," *IEEE Transactions on Microwave Theory and Techniques*, vol. 62, no. 12, pp. 2983–2989, December 2014.
- [71] "Design Guide for High Speed Controlled Impedance Circuit Boards," *A standard developed by the Institute for Interconnecting and Packaging Electronic Circuits*, March 2004.
- [72] H. Mansor and R. Abdul-Radman, "Optimal transition in Air-filled Substrate Integrated Waveguide," *IEEE Student Conference on Research and Development (SCORED)*, pp. 172–176, 2015.
- [73] P. Meyer, "RN01-Scattering Parameters," Ph.D. dissertation, University of Stellenbosch, 2017.
- [74] J. R. Pace and R. Mittra, "Generalized Scattering Matrix Analysis of Waveguide Discontinuity Problems," *Quasi-Optics XIV, New York. Polytechnic Institute of Brooklyn Press*, pp. 172–194, 1964.
- [75] H. J. Eul and B. Schiek, "A generalized theory and new calibration procedures for network analyser self-calibration," *IEEE Transactions on Microwave Theory and Techniques*, vol. 39, pp. 724–731, April 1993.